Novel Materials Chemistry for Structural, Photovoltaic, and Environmental Applications

By

TRAVIS M. REED

Bachelor of Science Chemistry
Wayne State College
Wayne, Nebraska
2010

Submitted to the Faculty of the
Graduate College of the
Oklahoma State University
in partial fulfillment of
the requirements for
the Degree of
DOCTOR OF PHILOSOPHY
May, 2018

NOVEL MATERIALS CHEMISTRY FOR

STRUCTURAL, PHOTOVOLTAIC, AND

ENVIRONMENTAL APPLICATIONS

Dissertation Approved:

Dr. Allen Apblett

Dissertation Adviser

Dr. Nicholas Materer

Dr. Charles Weinert

Dr. Frank Blum

Dr. Tyler Ley

ACKNOWLEDGEMENTS

Giving thought to all of the people who have helped and inspired me through this journey that is finally culminating with a doctoral degree is overwhelming. I know that my success was achieved solely based on the friendships and help of the people that affected my life along the way. I want to extend my thanks to those people in which there are too many to name. I would like to take this time to acknowledge the few who inspired me significantly.

Firstly, I would like express my deepest gratitude to my advisor, Dr. Allen Apblett. His guidance and advice that was directed toward me during my time here at Oklahoma State University was significant and will have lasting impressions on both my personal and profession life. His drive for new knowledge and his willingness to teach are quality traits that I hope to echo as I venture into the world. I would also like to thank my advisor committee members: Drs. Blum, Materer, Weinert, and Ley for serving on my committee and dedicating their time through this entire process.

Secondly, I would like to acknowledge the Apblett research group. The friendships made with the many people who have graced the research group has made my time here a more joyful experience. I especially would like to thank Zach Brown and Drs. Cory Perkins, Evangeline Rukundo, Ahmed Moneeb, Asma Alothman, and Ahmedul Kabir for encouragement, laughs, and good times. I will hold dear all the conversations

and experiences where cultures and life experiences were shared. An extra special thanks to Dr. Cory Perkins and Zach Brown for the endless amount of help whether that be with the large amount of proof reading or the willingness to listen to the countless hours of practicing for talks. Your friendships mean a great deal to me and will extend far past my time here at Oklahoma State University.

Finally, I would like to thank my family for all the love, support, and faith in me. Their belief in me was unwavering and helped me through the patches when I even doubted myself. To my parents, Mike and Lana, I cannot express how grateful I am for the sacrifices you two have made in helping me achieve my dreams. The willingness to lend a sympathetic ear or to provide advice has been a cornerstone in my success. To Kensie, who is my best friend and partner in crime, her strength and understanding during this entire process has meant everything to me. Your compassion and passion in everything you do is something I strive to emulate within my own life. I consider myself lucky to have you in my life. Thank you.

Name: Travis M. Reed

Date of Degree: MAY, 2018

Title of Study: NOVEL MATERIALS CHEMISTRY FOR STRUCTURAL, PHOTOVOLTAIC, AND ENVIRONMENTAL APPLICATIONS

Major Field: CHEMISTRY

Alkali-silica reaction (ASR) causes the untimely degradation of concrete structures such as bridges, dams, and roadways. This reaction occurs due to the alkalis present in the cement and the reactive forms of silica found in the aggregates used in concrete production. Neutralization of these reactive aggregates was done by a pretreatments using LiOH or Ca(OH)2 to the aggregates. The pretreated aggregates showed a significant reduction in expansion during the ASTM C 1260 standardized test leading to the elimination of ASR.

Additionally, the synthesis of bimetallic metal oxides were investigated for the use in arsenic remediation from aqueous media, as well as, for materials for potential photovoltaic applications. The synthesis of bimetallic pyruvic acid oxime precursors provides a low temperature decomposing single source precursors for the corresponding metal oxides. Controlling the stoichiometry of the metal salts in the precursor synthesis allows for retention of the desired stoichiometry in the final bimetallic metal oxide. Several Iron/zinc metal oxides of various stoichiometry were synthesized, characterized, and then used to treat arsenate ($H_2AsO_4^-$ and $HAsO_4^{2-}$) and arsenite (H_3AsO_3) aqueous solutions. Maximum capacities were determined by using both Langmuir and Freundlich adsorption isotherm models. Real world samples were investigated to examine samples with a more diverse matrix. These samples covered industrial wastewaters, ground water, and apple juice. In all treatments, the arsenic concentration was reduced to below the detection limit of the microwave plasma atomic emission spectroscopy. The other bimetallic metal oxide system investigated was cobalt-doped zinc oxide for potential use in photovoltaic applications. ZnO is a wideband gap semiconductor that absorbs light in the near ultraviolet region, but when doped with cobalt, the material is red shifted and absorbs light in the red wavelength range. The control of the stoichiometry allowed for the doping of ZnO with 5% and 10% cobalt through the decomposition of the pyruvic acid oxime precursors. Cobalt-doped ZnO was also synthesized in various doping percentages by a chemical bath method, which allows for growth of a film onto a glass slide. Films initially produced layered hydroxy salts that are easily converted to doped ZnO around 200 °C.

TABLE OF CONTENTS

Chapter Page

LIST OF TABLES

Table Page

Chapter II

Chapter III

Chapter IV

LIST OF SCHEMES

Scheme Page

LIST OF EQUATIONS

Equation Page

Chapter II

Chapter III

Chapter IV

LIST OF FIGURES

Figure Page

Figure Page

Chapter IV

CHAPTER I

Introduction

The focus on this dissertation is the manipulation of the surface properties of multi-metallic oxides either to prevent unwanted reactions or to promote desired reactions. The alkali silica reaction was the one targeted for inhibition. This reaction leads to crumbling of concrete infrastructures as siliceous aggregates are attacked by alkali in the cement paste. As described in Chapter 1, the use of LiOH and $Ca(OH)_2$ treatments of an alkali silica reaction prone aggregate (Jobe sand) were tested as methods for prevention of this devastating reaction that leads to the premature failure of concrete structures.

The desirable interfacial reaction explored in this research was the adsorption of arsenic from water and apple juice. As described in Chapter II, bimetallic iron/zinc oxides with varying ratios of the metals were investigated for the sorption of several arsenic species from water and apple juice.

The single source precursor method was used to produce cobalt-doped zinc oxides as described in Chapter III. These materials also have potential applications in arsenic remediation and catalysis, but the targeted application in this research was for use in photovoltaic devices.

Complementing this effort was an investigation of a solution growth or chemical bath method for preparation of cobalt-doped zinc oxide.

Alkali-Silica Reaction

Concrete is the most extensively used construction material in the world. It is a mixture of cement, coarse and fine aggregate, sand, and water mixed in specific ratios.[1] Some of the earliest uses of concrete-like technology dates back to around 3,000 B.C. with the Egyptians using gypsum and lime mortars for the building of the pyramids.[2] The major advance in concrete science was with the development of Portland cement by Joseph Aspdin in 1824 that drastically changed the approach for construction of infrastructure.[3] As the needs of society evolved, the features and properties of concrete and cement needed to change. The performance of the material was improved and changed through a variety of chemical and mineral admixtures. These admixtures can improve air entraining, reduce the amount of water required, slow or speed up setting, improve permeability, and increase strength of the concrete.[4] Improvement of the durability and performance of concrete is extremely important due to the cost and scale of use of concrete. Roads, bridges or dams need to have long lifespans to make these structures cost effective and practical. The cost of these projects are tied to the types of starting materials used in making of the cement and the concrete. The use of low cost aggregates are desirable, but could come with drastic issues such as early degradation or failure due to alkali-silica reaction.

Alkali-silica reaction takes place in concrete and is a chemical reaction between hydroxyl ions found within the cement and the siliceous aggregate used to make the concrete.[5] This reaction causes the formation of a gel that expands to cause cracking and

damage to the concrete. This cracking allows further reactions to take place and this process can propagate until failure of the structure (Figure 1). Slowing or prevention of alkali-silica reaction can be accomplished by the addition of admixtures such as fly ash, slag, or lithium salts or the use cement with low alkali metal content.[6]

Figure 1: Concrete damage caused be alkali-silica reaction.[7]

Bimetallic Oxide Materials

Metal oxide materials are used for an extensive list of applications. Major areas where metal oxides are used include sensing,[8] catalysis,[9] energy production and storage,[10] and environmental applications.[11,12] The desire to use metal oxides in these approaches comes from a variety of features that include their wide range of surface chemistry, interesting electronic properties, and their amenability for production on the nanoscale. The latter property allows for an alteration of properties to provide ones that are not found in the bulk material. Synthesis of metal oxides can be achieved by several conventional methods. Use of the ceramic method, sol-gel method, hydrothermal or solvothermal methods, and precursor method are some of the commonly used approaches to achieve various metal oxides. This

study will focus on the precursor method and chemical bath deposition technique for the synthesis of the bimetallic metal oxides.

The Precursor Method

The precursor method allows for the synthesis of a metal containing precursor that then can be subsequently converted to the corresponding metal oxide. A typical synthetic route using this method consists of the reaction of a soluble metal salt with an organic ligand to produce a precursor complex.[13] This approach allows metal cations to be mixed on the atomic level with a controlled stoichiometry in the metal-organic complex.[14] The metals present within the precursor complex have short diffusion distances to combine with each other, thus allowing the formation of complex bimetallic oxides to form at relatively low temperatures.[14] These precursor complexes can then be heated to remove organics resulting in deposition of the metal oxides. The organic ligands that are chosen are often used to provide sources of oxygen, but can also be used to influence the final materials particle size, shape, and surface properties.[15] Issues with this method that need to be addressed includes the difficulty in controlling stoichiometry in mixed metal syntheses when the precipitation rates for the selected metals vary. Another issue that arises is in the choice of organic ligand. Choosing an organic ligand that will easily decompose leaving behind pure material is key.

Pyruvic acid oxime is the organic ligand used for this research. Apblett and coworkers published the initial work on this synthetic approach in an investigation into the capture of radioactive nuclides by complexation with sodium pyruvic acid oxime. This precipitation then allowed the formation of metal oxides through decomposition at low temperatures (< 300 °C).[16] Pyruvic acid oxime metal complexes decompose at low

temperatures into the metal oxide and volatile fragments: water, carbon dioxide and acetonitrile.[17] In this investigation, this synthetic method was used to develop iron/zinc mixed metal oxides for the use in arsenic remediation in aqueous systems and to develop cobalt-doped zinc oxide to be used in photovoltaic applications.

Chemical Bath Deposition Technique

Chemical bath deposition is often used for the growth of semiconductor films onto substrates. This simple and easily reproducible process can be performed at low temperatures using cheap starting materials such as urea and hexamethylenetetramine.[18] This synthesis undergoes two specific stages, nucleation and particle growth. [19] The film growth with this process is quite robust, being able to coat almost any type of substrate and any overall shape.[19] Variable reaction parameters such as pH, temperature, total reaction time, and concentration can lead to variations in the final films. These parameters can effect crystal size, crystal shape, and film thickness.[19,20]

The chemical bath deposition used for this project involved the use of hexamethylenetetramine as the hydroxyl ion source. These hydroxyl ion react with the metal ions in solution and precipitate the metal hydroxide out of solution.[21] This process was used to create films of cobalt-doped zinc oxide on glass slides.

Removal of Arsenic from Contaminated Waters

Elemental arsenic is a metallic grey metalloid, but is usually found as a component of naturally occurring minerals.[22] Arsenic is the 20th most abundant element in the Earth's crust and is commonly found naturally in arsenates, metal arsenides, and sulfide minerals, with arsenopyrite (FeAsS) being the most abundant.[23] Arsenic adopts a wide range of oxidation

states (-3, 0, +3, +5) in various organic and inorganic forms. Inorganic oxyanions of +3 and +5 arsenic exist mainly in water. Arsenite (AsO_3^{3-}) and arsenate (AsO_4^{3-}) are found as contaminants in water, that when ingested can cause serious illnesses and death (Figure 2).

Figure 2: Black foot disease caused by long-term arsenic exposure.[24]

Both oxyanion species can be present within a water source due to the slow nature of the redox chemistry (Figure 3).[23] The presence of both species in water provides difficulty for the development of a cheap and easy to use technique to target both species (Figures 4 & 5). This difficulty arises primarily from a variance in overall charge of the species in waters.

At pH 7, arsenite is found as a neutral species (H_3AsO_3) while arsenate is found negatively charged ($H_2AsO_4^-$ or $HAsO_4^{2-}$).

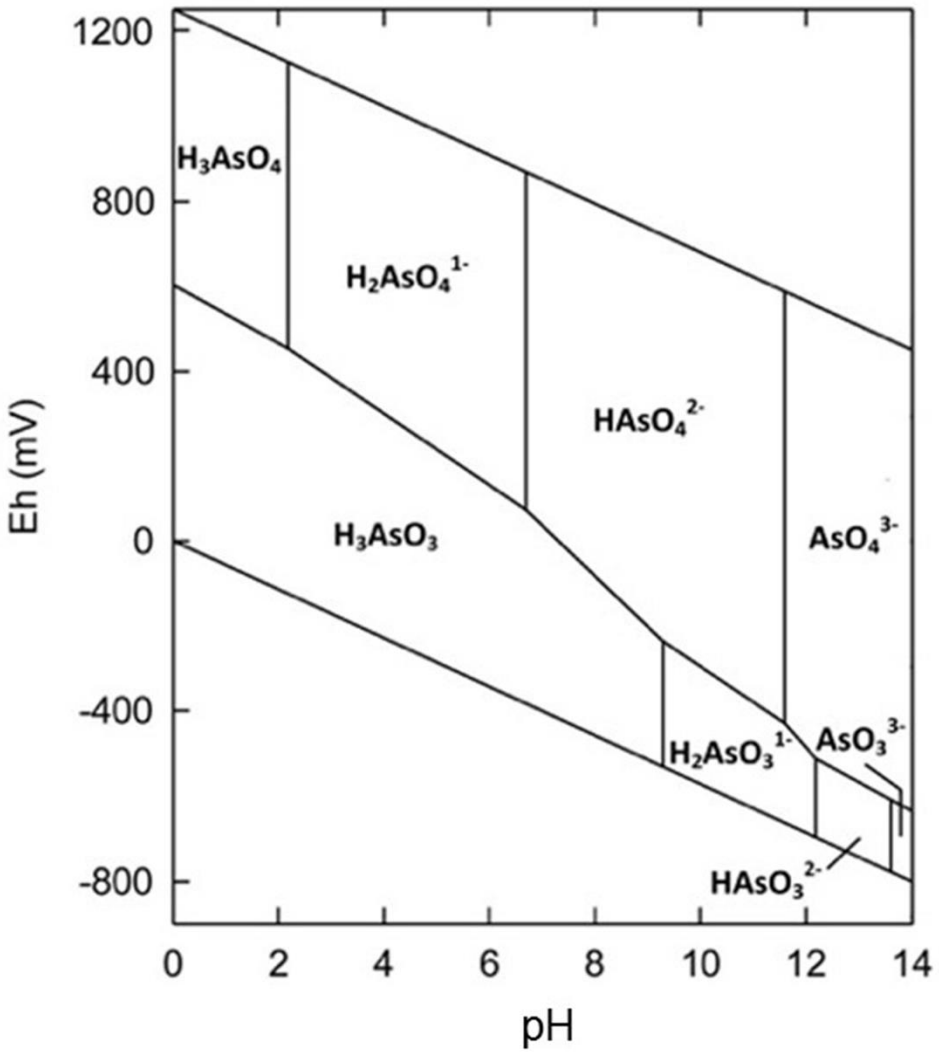

Figure 3: Pourbaix diagram for aqueous arsenic species.[25]

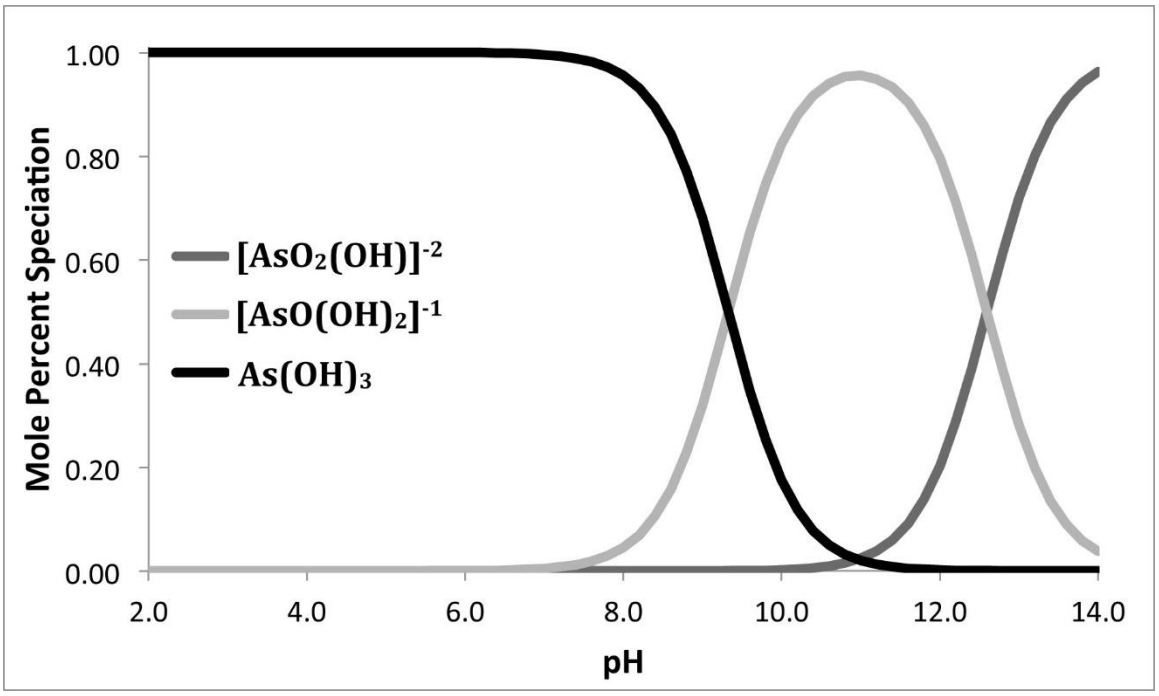

Figure 4: Aqueous arsenic (III) species distribution as a function of pH.[25]

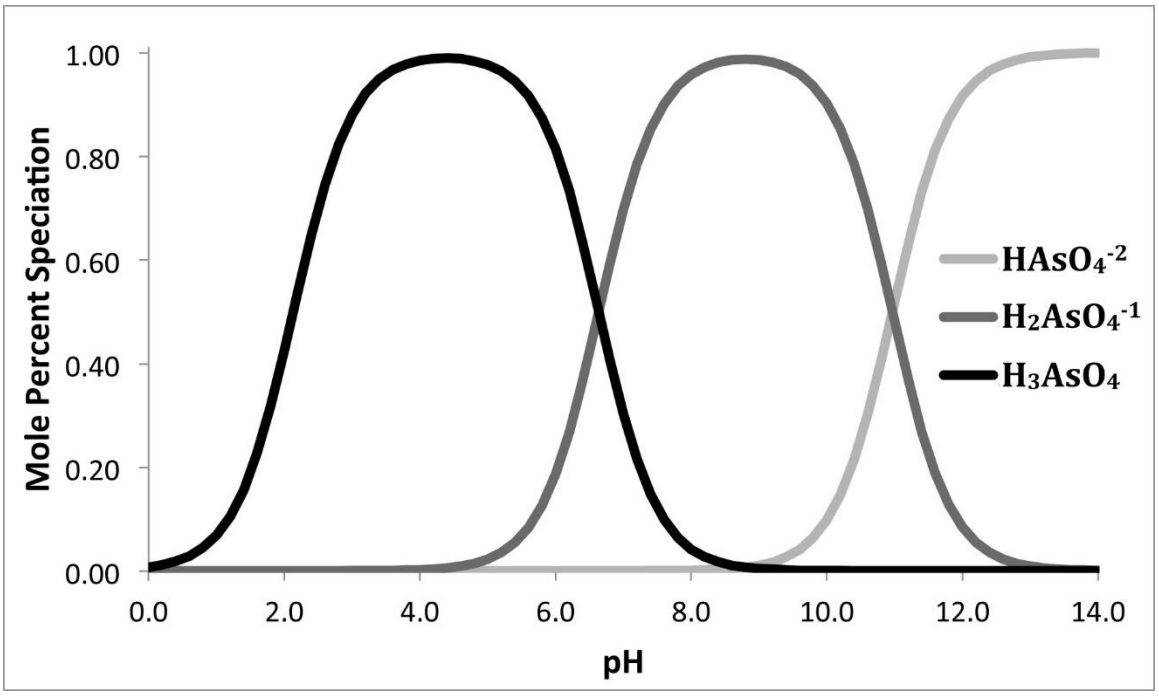

Figure 5: Aqueous arsenic (V) species distribution as a function of pH.[25]

Current technologies that are utilized to combat arsenic contamination in aqueous waters includes oxidation/precipitation, coagulation, ion exchange, reverse osmosis, and adsorption.[26] These technologies have a variety of shortcomings and often only target the arsenate species.[26] Using the adsorption technique, materials, such as metal oxide nanomaterials, can be designed to have improved surface area and unique surface features that enable the efficient adsorption of both the arsenate and the arsenite species.

Materials for Photovoltaic Applications

Photovoltaic materials absorb light and in return produce electricity. This effect is referred to as the photoelectric effect. This technology was initially developed for the space program, but eventually found terrestrial use during the 1970s oil embargo.[27] The pioneering system that was explored for these devices was silicon wafers.[27] These materials had high efficiency, but were very expensive to use. Next, the devices shifted to thin film processes that reduced the price of the devices, but lowered the overall efficiency. The third generation of photovoltaic devices uses thin film materials with varying bandgaps that when added together make several junctions. These multiple junctions improve efficiency by allowing for a wide range of the solar spectrum to be absorbed. In developing these multi-junction devices, there is a need for finding materials where the bandgap can be controlled or tailored to maximize the amount of light being absorbed.[28] The interest in wide band gap semiconductors for use in photovoltaic applications stems from a broad choice of synthetic routes, an ability to achieve nanostructure morphologies, and a capability to tailor the bandgap.[29]

This study will discuss the use of zinc oxide that has a bandgap of 3.37 eV and absorbs in the near ultraviolet region of the electromagnetic spectrum.[30] Zinc oxide can undergo doping with various transition metals to alter the bandgap and allow the material to absorb into the visible spectrum.[31] This control of the material's bandgap allows for absorption of a wider range of light.

Scope of the Study

The topics being covered in this study includes the investigation into the neutralization of reactive aggregates of cement to prevent alkali-silica reaction and the development of bimetallic oxides for the use in the remediation of arsenic from aqueous samples and in photovoltaic devices.

In Chapter II, this study covers the investigation into the neutralization of reactive aggregates used in cement to prevent alkali-silica reaction. The hypothesis was that treatments with lithium and calcium hydroxide, would pre-react active sites on the surfaces of the siliceous mineral to form non-expansive lithium or calcium silicates. This was predicted to prevent the formation of sodium or potassium silicates and the attendant damage they cause. The ability to prevent or reduce the expansion by alkali-silica reaction would allow for the use of inexpensive and much more readily available alkali-silica reaction prone aggregates for concrete. This can correlate to being able to use cheaper building materials that do not suffer from the premature degradation that is seen in concrete undergoing alkali-silica reaction.

The second part of this study involves the development of several bimetallic oxides through two different routes for environmental and photovoltaic applications. In Chapter III, iron-zinc

oxides were synthesized with varying iron and zinc molar ratios and these were used to treat various arsenic containing aqueous solutions. These bimetallic oxides were made through the decomposition of a pyruvic acid oxime precursor. Controlling the stoichiometry in the starting solutions allowed for control of the metal molar ratios in the final metal oxide. The investigation of mixed zinc-iron oxide was performed to improve the arsenate and arsenite adsorption capacities from what was possible using pure iron oxide. This improvement in the adsorption is expected to come from addition of zinc, which is a softer Lewis acid. In Chapter IV, the synthesis of cobalt-doped zinc oxide for the use in photovoltaic applications is discussed. The percentage of cobalt doping was varied to allow several different materials to be investigated for their photovoltaic properties. Syntheses of these materials were done by two methods. Initially, pyruvic acid oxime precursors were used to synthesize the final cobalt doped zinc oxide, but the desire for film growth led to the use of the chemical bath deposition method. This technique allowed for film growth onto glass slides at 90 °C. These films can be easily developed for use in photovoltaic devices.

References

1. Hasan, S. T. All About Cement. civiltoday.com/civil-engineering-materials/cement/81-cement-definition-and-full-details.

2. Shepard, N. G. K. The History of Concrete. www.nachi.org/history-of-concrete.

3. Biernacki, J. J.; Bullard, J. W.; Sant, G.; Brown, K.; Glasser, Fredrik P.; Jones, S.; Ley, T.; Livingston, R.; Nicoleau, L.; Olek, J.; Sanchez, F.; Shahsavari, R.; Stutzman, P. E.; Sobolev, K.; Prater, T., Cements in the 21st century: Challenges, perspectives, and opportunities. Journal of the American Ceramic Society 2017, 100 (7), 2746-2773.

4. Chemical Admixtures. http://www.cement.org/cement-concrete-applications/concrete-materials/chemical-admixtures.

5. Thomas, M. D. A., Fournier, B., Folliard, K.J. Alkali-Aggregate Reactivity (AAR) Facts Book; The Transtec Group, Inc.: 2013.

6. Bauer, S.; Cornell, B.; Figurski, D.; Ley, T.; Miralles, J.; Folliard, K. Alkali-silica reaction and delayed ettringite formation in concrete: A literature review; 2006.

7. Technology, F. H. A. R. a. Alkali-Silica Reaction. fhwa.dot.gov/publications/research/infrastructure/pavements/pccp/03047/02.cfm.

8. Fine, G. F.; Cavanagh, L. M.; Afonja, A.; Binions, R., Metal Oxide Semi-Conductor Gas Sensors in Environmental Monitoring. Sensors 2010, 10 (6), 5469.

9. Khan, M. M.; Adil, S. F.; Al-Mayouf, A., Metal oxides as photocatalysts. Journal of Saudi Chemical Society 2015, 19 (5), 462-464.

10. Jose, R.; Thavasi, V.; Ramakrishna, S., Metal Oxides for Dye-Sensitized Solar Cells. Journal of the American Ceramic Society 2009, 92 (2), 289-301.

11. Xu, P.; Zeng, G. M.; Huang, D. L.; Feng, C. L.; Hu, S.; Zhao, M. H.; Lai, C.; Wei, Z.; Huang, C.; Xie, G. X.; Liu, Z. F., Use of iron oxide nanomaterials in wastewater treatment: A review. Science of The Total Environment 2012, 424 (Supplement C), 1-10.

12. Perkins, C. K.; Reed, T. M.; Brown, Z. A.; Apblett, A. W., Exceptional sorption behaviour of porous tungsten oxide for aqueous lead. Environmental Science: Water Research & Technology 2017, 3 (3), 429-432.

13. Apblett, A. W.; Georgieva, G. D.; Mague, J. T., Synthesis and Spectroscopic and Thermal Decomposition Studies of Alkali Metal Salts of 2-Oximidopropionate. Inorganic Chemistry 1997, 36 (12), 2656-2661.

14. Vidyasagar, K.; Gopalakrishnan, J.; Rao, C. N. R., A convenient route for the synthesis of complex metal oxides employing solid-solution precursors. Inorganic Chemistry 1984, 23 (9), 1206-1210.

15. Georgieva, G. D. Metal carboxylate precursors for ceramic materials and waste forms for radionuclides. Ph.D. Dissertation, Tulane University, New Orleans, LA, USA, 1995.

16. Apblett, A. W.; Georgieva, G. D.; Mague, J. T., Incorporation of Radionuclides into Mineral Phases via a Thermally Unstable Complexant Ligand. MRS Proceedings 1992, 294.

17. Bagabas, A. A. Low temperature precursors for metal oxide catalysts. Ph.D. Dissertation, Oklahoma State University, Stillwater, OK, USA, 2005.

18. Nair, P. K.; Nair, M. T. S.; García, V. M.; Arenas, O. L.; Peña, A. C. Y.; Ayala, I. T.; Gomezdaza, O.; Sánchez, A.; Campos, J.; Hu, H.; Suárez, R.; Rincón, M. E., Semiconductor thin films by chemical bath deposition for solar energy related applications. Solar Energy Materials and Solar Cells 1998, 52 (3), 313-344.

19. Hodes, G., Semiconductor and ceramic nanoparticle films deposited by chemical bath deposition. Physical Chemistry Chemical Physics 2007, 9 (18), 2181-2196.

20. Niesen, T. P.; De Guire, M. R., Review: deposition of ceramic thin films at low temperatures from aqueous solutions. Solid State Ionics 2002, 151 (1), 61-68.

21. Hari, P.; Baumer, M.; Tennyson, W. D.; Bumm, L. A., ZnO nanorod growth by chemical bath method. Journal of Non-Crystalline Solids 2008, 354 (19), 2843-2848.

22. Greenwood, N. N., Chemistry of the elements. 2nd ed.; Oxford Boston : Butterworth-Heinemann: Oxford Boston, 1997.

23. Mandal, B. K.; Suzuki, K. T., Arsenic round the world: a review. Talanta 2002, 58 (1), 201-235.

24. Chronic Arsenic Poisoning: Pictures of Sufferers. users.physics.harvard.edu/~wilson/arsenic/pictures/arsenic_project_pictures2.html.

25. Bulut, G.; Yenial, Ü.; Emiroğlu, E.; Sirkeci, A. A., Arsenic removal from aqueous solution using pyrite. Journal of Cleaner Production 2014, 84 (Supplement C), 526-532.

26. Mohan, D.; Pittman, C. U., Arsenic removal from water/wastewater using adsorbents—A critical review. Journal of Hazardous Materials 2007, 142 (1), 1-53.

27. Green, M. A., Recent developments in photovoltaics. Solar Energy 2004, 76 (1), 3-8.

28. Matt Boreland., D. B. Current and Future Photovoltaics; Office of Science and Innovation: United Kingdom, 2006.

29. Djurišić, A. B.; Liu, X.; Leung, Y. H., Zinc oxide films and nanomaterials for photovoltaic applications. physica status solidi (RRL) – Rapid Research Letters 2014, 8 (2), 123-132.

30. Özgür, Ü.; Alivov, Y. I.; Liu, C.; Teke, A.; Reshchikov, M. A.; Doğan, S.; Avrutin, V.; Cho, S.-J.; Morkoç, H., A comprehensive review of ZnO materials and devices. Journal of Applied Physics 2005, 98 (4), 041301.

31. Yang, S.; Wang, Y.; Bai, L.; Liu, B.; Fan, J.; Yang, X.; Zhao, H.; Wei, C.; Huang, Q.; Chen, X.; Wang, G.; Zhao, Y.; Zhang, X., Transparent double-period electrode with effective light management for thin film solar cells. RSC Advances 2013, 3 (1), 208-214.

CHAPTER II

Development of Aggregate Coatings for Prevention of Alkali-Silica Reaction

Introduction

Concrete structures play a vital role within the world's infrastructure. Concrete is used as a building material in our roads, bridges, dams and buildings. Failures within concrete can lead to significant property damage that can be expensive and put lives at risk. Concrete is made when cement and water is mixed with an aggregate, such as sand, gravel, or crushed rock.[1] Cement is often manufactured through a dry method.[1-2] This process involves the quarrying of the limestone, clay, shale, or other starting materials. The starting materials are then pulverized that reduce the rocks to under 3 inches.[2] The material is then heated in a kiln at high temperatures (around 1500 °C).[2] There are several ways that concrete can fail including corrosion of the steel rebar support, deterioration by water going through freeze-thaw cycles within the concrete, physical and chemical sulfate attack, and alkali-silica attack. Alkali-silica reaction (ASR) is a reaction that occurs within concrete between the reactive silica found within the aggregate and cement containing elevated levels of alkali metal ions. The high pH of the cement paste causes the silica to dissolve and a alkali metal silicate gel to form around the aggregate.

This gel, in the presence of moisture, expands and can lead to increased internal pressure that causes cracking as can be seen in Figures 1 and 2. This internal pressure and associated cracking can ultimately lead failure of the concrete.

Figure 1: ASR cracking on a bridge parapet in Illinois.[3]

Figure 2: Extensive ASR cracking found in bridge columns (left). ASR damage in pavement slabs (right).[4]

The start of the cracking of concrete allows for water ingress which causes further formation and swelling of gel throughout the material leading to reduced strength and increased permeability that ultimately leads to a catastrophic failure of the concrete.[5] The increase of permeability can also lead to further damage such as corrosion of rebar and freeze/thaw damage. Hydroelectric dams, bridges, highways and runways all can suffer from degradation caused by alkali-silica reaction. Typically, visible signs of ASR take 10 to 15 years to appear but there have been documented cases of ASR damage appearing within six months. The onset of ASR depends strongly on the susceptibility of the aggregate and the alkali metal content of the cement.

Since the identification of ASR in 1940, there has been a large amount of research investigating the causes and methods for prevention of ASR. Thaulow and coworkers previously determined that ASR gel contains calcium, silicon, potassium, sodium, and water.[6] The ratio of the components of the ASR gel can be found in broad variation. The variation of the individual elements can determine how the ASR gel behaves within the concrete and determines the outcome of the ability to damage the concrete. The mechanism for ASR gel formation is complex and not completely fully understood. The initial step of this reaction takes place with the highly alkaline cement dissolving the silica that is present within the aggregate. This step is accelerated by the presence of poorly crystalline hydrous silica that enables deeper penetration of hydroxyl and sodium or potassium ions into the silica causing increased cleavage of the silicon-oxygen bonds.[7] Aggregates with amorphous types of silica, such as opal, are especially prone to ASR.[8] The dissolved silica forms alkali metal silicates, also referred to as alkali silica gel.

Traditionally, five common methods that are used to control ASR gel formation within the concrete. The most obvious of these is to use aggregates that do not undergo ASR, but there is a high demand and a low availability of these aggregates. Further, aggregates that do not undergo ASR might have to be shipped a great distance causing an economic obstacle for the budgets of the target projects. The second method for combating ASR is to limit the amount of alkali in the cement. Manufacturers can produce low-alkali cement with a Na_2O equivalent less than 0.6%. The low Na_2O equivalent ensures low alkali content, thus limiting ASR and decreasing the damage, but these cements are expensive. The Na_2O equivalent can be calculated from Equation 1, which correlates sodium and potassium as their respective oxides. Both Na_2O and K_2O can be assumed to have identical behavior under the conditions that are present in concrete that can undergo ASR.[9]

$$Na_2O_{equivalent}[wt\%] = Na_2O[wt\%] + 0.658K_2O[wt\%]$$

Equation 1: Equation to determine alkali content found within cement.

The third approach is to reduce the amount of moisture in the concrete limiting the formation of the ASR gel. There are two approaches for limiting the moisture. The first is to apply a protective coating after the concrete has hardened, providing a barrier to protect the concrete from water permeation. The other approach to limit moisture is by using extensive curing or the addition of various admixtures. The use of admixtures and extensive curing produces a concrete with low permeability. This low permeability provides a barrier to prevent the migration of water into the concrete. Lastly, ASR can be minimized by the addition of pozzolanic materials. Pozzolanic materials are siliceous and

or aluminous materials that when hydrated can react with calcium hydroxide ($Ca(OH)_2$), the alkalis in the pore solution, and reactive silica from the material to form secondary products.[10] This approach introduces secondary cementitious materials (SCMs), such as fly ash and slag, into the cement to mitigate ASR. The SCMs can reduce the swelling capacity, lower the viscosity of the ASR gel, lower the ion diffusion coefficient, and reduce the long term permeability.[11,12] On top of these possible property changes, the use of fly ash and slag are economically beneficial, as they are from waste streams from steel production and the combustion of coal.[11] Another additive that can be used to stop ASR from propagating is lithium nitrate ($LiNO_3$). Though the specific mechanism is not well understood, addition of large amounts of $LiNO_3$ before or after the concrete has been cast, can stop ASR.[13] This process is quite costly due to the large amount $LiNO_3$ needed and the price. The amount of $LiNO_3$ needed is the amount required to achieve a lithium to alkali molar ratio ([Li]/[Na + K]) of 0.74.[14]

The first part of the alkali-silica reaction involves the cleavage of the siloxane networks by the hydroxide (OH^-) ions to form alkali silicate and silicic acid (Scheme 1). Silicic acid can further react with the hydroxide ions to be further converted into alkali silicate.

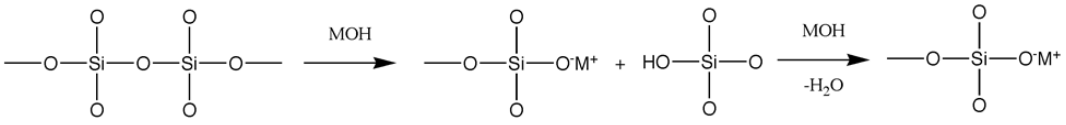

Scheme 1: The alkali-silica reaction (M = Na^+ or K^+)

The composition of the ASR gel plays a key role in whether swelling takes place. The hypothesis tested in this work is that pre-treatment of an ASR reactive aggregate with a

metal hydroxide (either LiOH or an alkaline metal hydroxide) can neutralize reactive sites before they are exposed to sodium or potassium hydroxide in the cement matrix. Support for this hypothesis is provided by the work done by Cannon and coworkers, in which pre-treatment of Jobe sand with a concentrated barium hydroxide ($Ba(OH)_2$) solution led to a reduction of expansion in the mortar bar at 14 days by 23% for a single treatment.[15] These positive results led them to treat the Jobe sand twice with concentrated $Ba(OH)_2$ solutions reducing expansion by 45% at the end of the 14 day ASTM C1260 test.[15]

In this study, we investigated the effectiveness of treating Jobe sand, with LiOH and $Ca(OH)_2$ solutions. Jobe sand was selected as the aggregate of choice due to its known ability to undergo ASR.[16] Jobe sand is a product from the Jobe-Newman Quarry in El Paso, Texas and is readily available. It is considered to be a highly ASR reactive due to its specific composition of microcrystalline SiO_2 (chert) and aluminosilicate (feldspar).[17] LiOH and $Ca(OH)_2$ were chosen due to the possibility of converting the reactive silica found within the aggregate to a more stable calcium or lithium silicate. In pre-treating the aggregate prior to the use in concrete our hypothesis is that it will be unnecessary to use additives, such as $LiNO_3$, to stop or prevent ASR. Instead with no reactive silicates, the aggregate can be used like crystalline aggregates that do not exhibit any ASR.

Experimental

The first approach to reactively neutralize the aggregate that was investigated utilized treatment with saturated $Ca(OH)_2$ solution. 150 g of Jobe sand was treated with

200 mL of saturated $Ca(OH)_2$ solution at 80 °C for 24 h. After the reaction, the sand was washed thoroughly with deionized water. Washing with deionized water was done until a constant reading was achieved with a conductivity meter. The sand was then dried at 60 °C. The treatment cycle was repeated a total of 25 times to allow for more $Ca(OH)_2$ to react with the aggregate. A large number of reactions were necessary to allow for a sufficient amount of the silica to be reacted due to the low solubility of $Ca(OH)_2$. The treated sand was then analyzed by X-ray fluorescence (XRF) to identify any increase in calcium present within the sand. The sand was then used in testing for ASR reactivity by using the ASTM C 1260 test.[18] ASTM C 1260 is an accelerated mortar bar test that measures the performance of the aggregate within concrete. This test is widely accepted and provides test results within 14 days. It involves the production of mortar bars that are immersed in 1 M sodium hydroxide (NaOH) at 80 °C. This environment provides conditions that lead to an accelerated rate of ASR. The bars are removed at specific times and their lengths are measured. As ASR starts to develop, the length of the mortar bar will increase. To pass the test the mortar bar must have an average expansion of less than 0.10% over 14 days. If after the 14 days the sample has an average expansion of less than 0.20% but greater than 0.10%, the sample needs further investigation to determine if the expansion that is present is due to ASR. If the sample shows an expansion of greater than 0.20%, the aggregate is considered ASR prone.

The second approach to reactively neutralize the aggregate involved treatment with LiOH. Twelve plastic bottles were used as reaction vessels. Each plastic bottle held 100 g of Jobe sand and was filled with 115 mL of 2 M LiOH. The bottles were placed in a hybridization oven and rotated for 4 days at 80 °C. After 4 days, the sand was then

washed thoroughly with tap water and then washed with deionized water until the conductivity remained constant. The sand was then dried overnight at 60 °C. The same procedure was completed for a second time, but this time the reaction was performed at room temperature. The sand was washed using the same procedure and then dried overnight at 60 °C. This allowed for the determination of the influence on an elevated reaction temperature and its results on the testing. Sand was also produced by using both the elevated temperature method and room temperature method twice. The sand was treated twice in order to provide a more completely neutralized aggregate. All sand samples were tested by the ASTM C 1260 test and the difference in ASR expansion when compared to uncoated Jobe sand is shown later in Table 2.

Results and Discussion

Treatment with $Ca(OH)_2$ solution was chosen as the means to replace the more reactive silicate with less reactive calcium silicate since it is known that gels produced by ASR high in calcium undergo a very low amount of swelling.[19] Due to the low solubility of the $Ca(OH)_2$, the reactions were repeated 25 times in order to neutralize a substantial amount of reactive aggregate. The 25 reactions led to an uptake of 8.6 g of $Ca(OH)_2$, which if assumed the sand is pure silica (SiO_2), we estimate a total reaction of 4.6% of the sand. The $Ca(OH)_2$ treated sand was analyzed by XRF, a technique that allows for comparisons of amounts of individual elements by measuring counts of secondary X-rays produced by the excited material when bombarded with primary X-rays. XRF was used to follow the change in intensity of calcium from the untreated Jobe sand to the final treated material. The spectrum of the untreated Jobe sand shows a low intensity (<100,000 counts) for calcium (Figure 3) and a drastic increase of the calcium intensity

for the final treated material (Figure 4). This is mirrored in the solutions, of all 25 treatments, with the intensity of $Ca(OH)_2$ decreasing from the starting solution to the final solution after treatment (Figure 5). Comparing the Ca/Fe and K/Fe intensity ratios from the untreated and treated XRF spectra, there is a percent increase of 1068% for Ca/Fe intensity and a percent decrease of 11.9% for K/Fe upon the $Ca(OH)_2$ treatment. Since iron is not lost into the alkaline solution, the XRF signal for iron is used as an internal standard to help quantify the changes in calcium and potassium content.

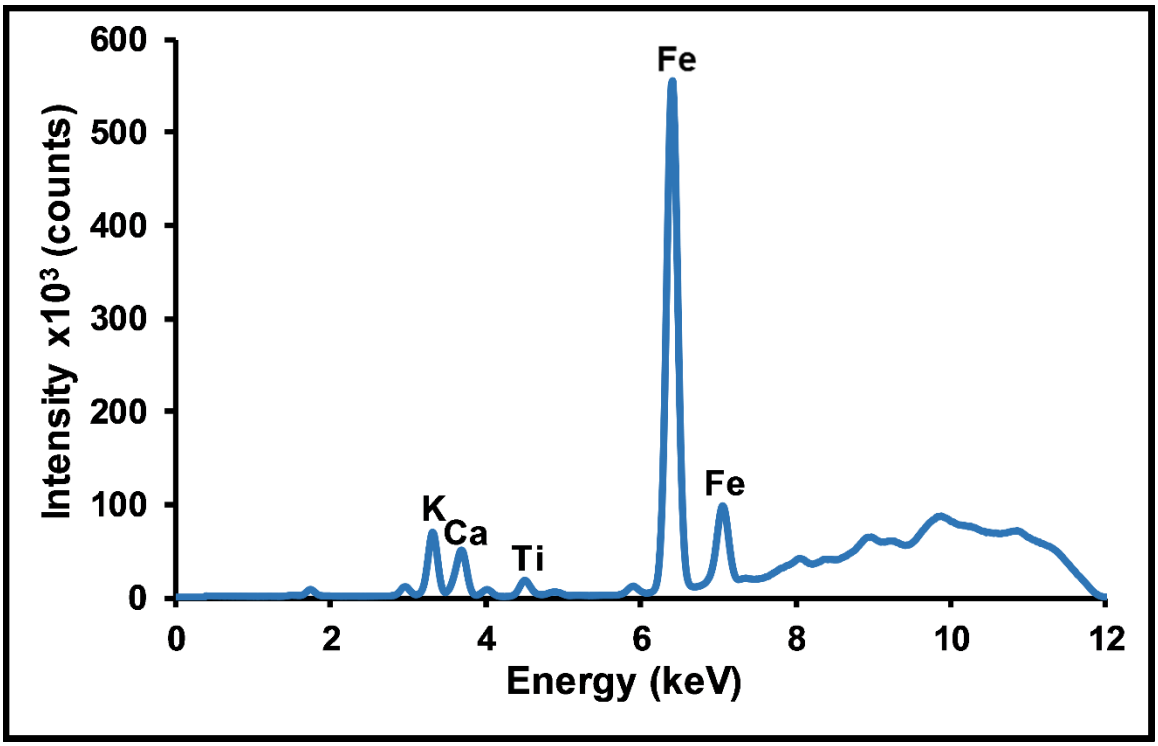

Figure 3: XRF spectrum of the untreated Jobe sand.

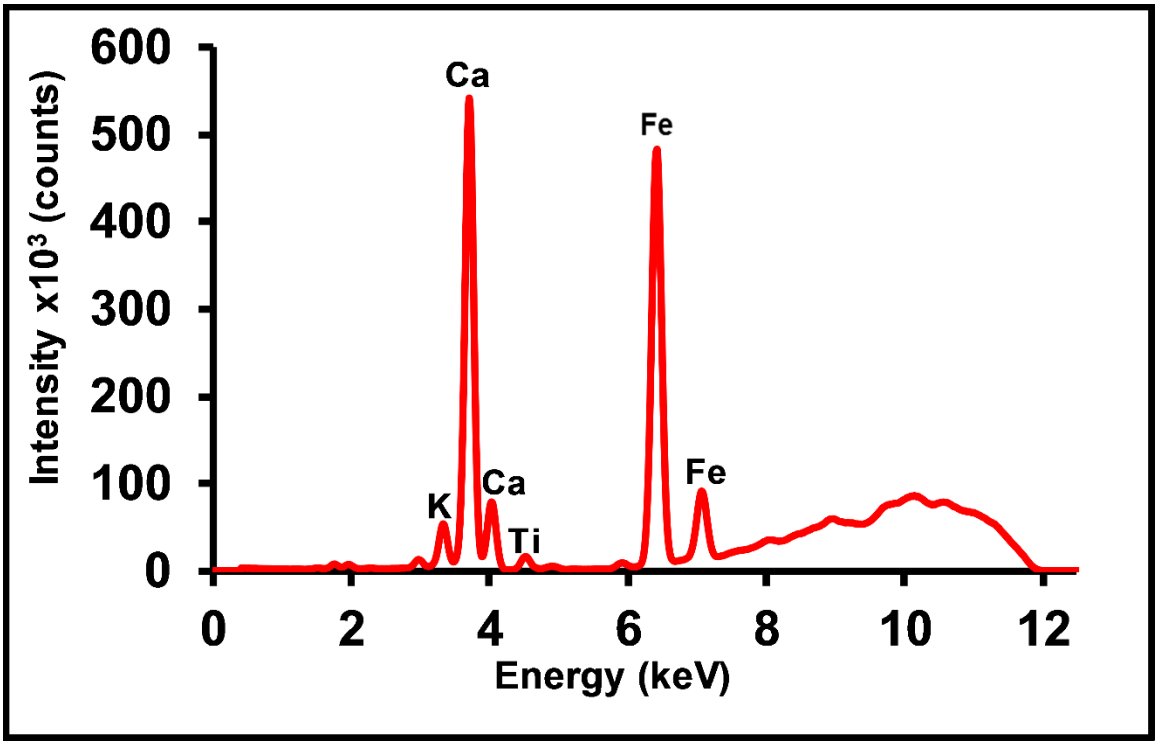

Figure 4: XRF spectrum of the $Ca(OH)_2$ treated Jobe sand.

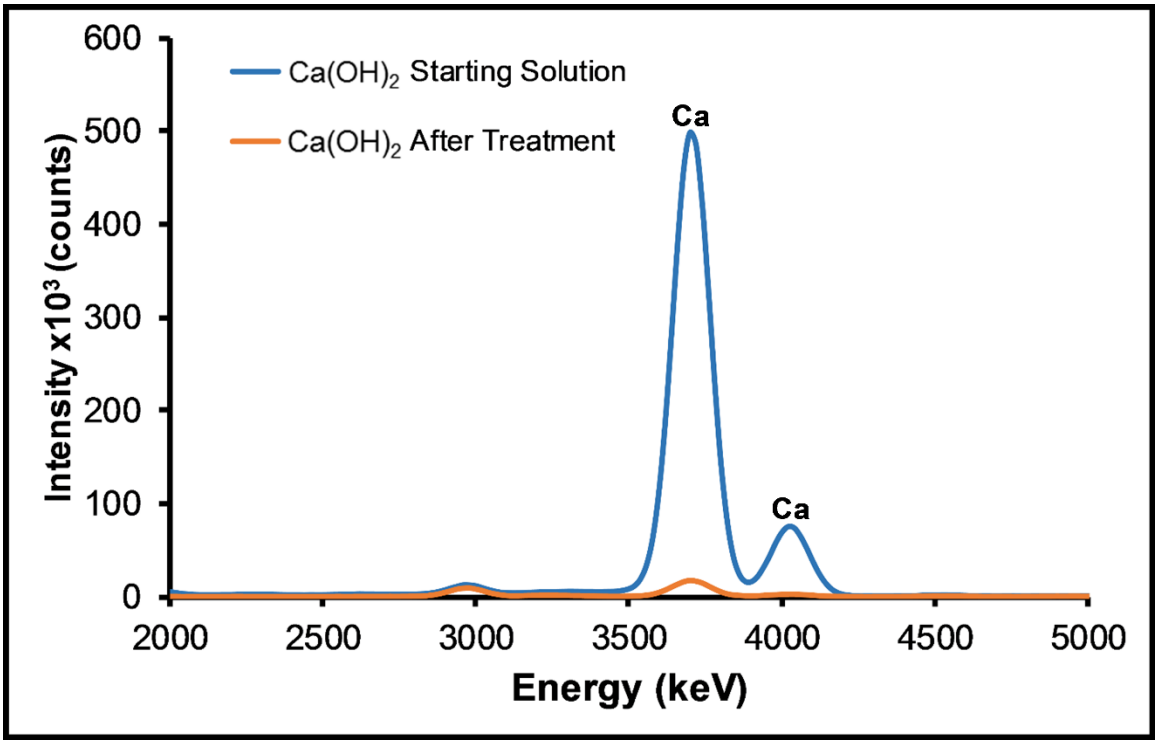

Figure 5: XRF spectrum of the change of intensities of the starting $Ca(OH)_2$ solution to the final $Ca(OH)_2$ solution.

Treatment of Jobe sand provided positive results in reducing ASR (Figure 6). The percent expansion versus time curves generally show a steep increase in expansion in the first 10 days. This increase is followed by a slower almost linear trend for both the control mortar bar and the bar made using the $Ca(OH)_2$ treated sand. After 3 days, the mortar bar containing $Ca(OH)_2$ treated sand begin to expand at a slower rate than the control. After the first 14 days, the $Ca(OH)_2$ treated sand had an expansion of 0.46% (Figure 6). This expansion is an improvement from the untreated sand, but the sample is still showing symptoms of ASR, as it is over the 0.10% limit. At the end of the test, the $Ca(OH)_2$ treated sample expanded only 0.82%, less than the control which expanded 0.95%. In total, the treatment of the sand with $Ca(OH)_2$ led to 14% reduction in expansion over the 80 day testing period (Figure 7).

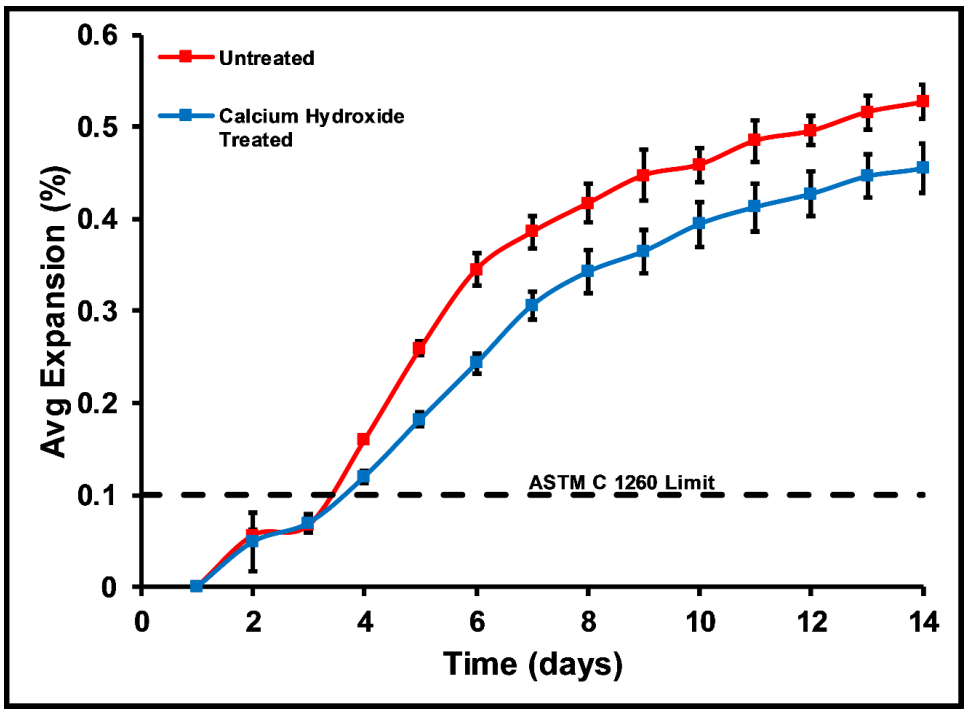

Figure 6: ASR test results for mortar bars using $Ca(OH)_2$ treated sand after 14 days.

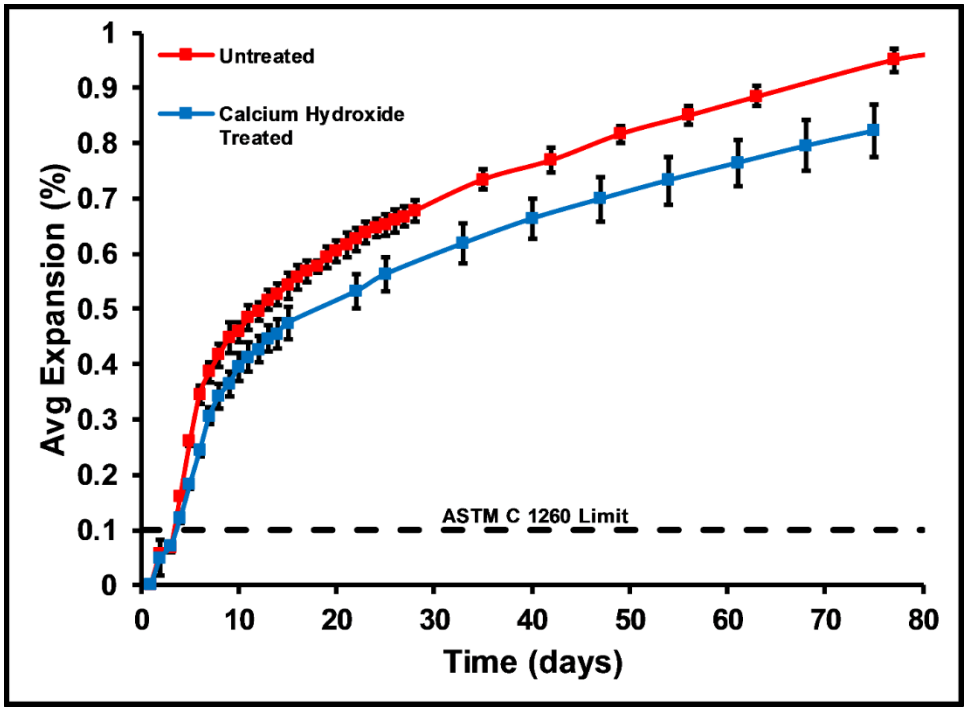

Figure 7: ASR test results for mortar bars using $Ca(OH)_2$ treated sand after 80 days.

The treatment with LiOH was performed on the hypothesis that the neutralized aggregate would display similar properties to that of the addition of $LiNO_3$. Incorporation of large amounts of $LiNO_3$ into concrete must be performed in order to prevent ASR from taking place. Aggregate was reacted with 2 M LiOH at both room temperature and at an elevated temperature (80 °C) for 4 days. After the desired reaction times, the treatment solutions were diluted (1:100) with deionized water and analyzed. The lithium concentrations were determined by the use of flame photometry, a method that allows for concentration determination of alkali and alkali earth metals by use of a photodetector to capture emitted light from the excited metals. Lithium produces a red light that is emitted at a wavelength of 670 nm.[20] Calibration of the instrument was done with the use of Li standards diluted from a 1000 ppm stock solution made from $LiOH \cdot H_2O$ (Figure 8). The

total available lithium available for reaction in 115 mL of each treatment solution is 1.6 g. The room temperature treatments were only able to reach about 65% of reacted lithium compared to that of the treatments at elevated temperature. The percent change from the starting solutions to the reacting solutions of the room temperature treatments were around a 55% decrease in lithium concentration, whereas, in the 80 °C treatments the change was roughly 85%. Final concentrations and percent changes are summarized in Table 2.

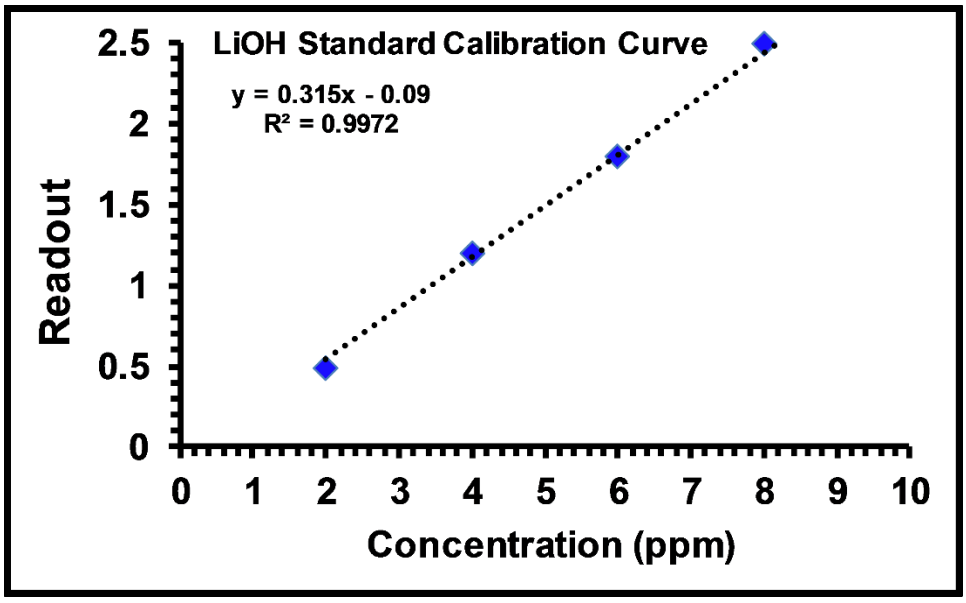

Figure 8: Standard calibration curve for Li using flame photometry.

Table 1: Lithium results from flame photometry.

Treatment	Flame Photometry Readout	Final [Li^+] (ppm)	Change (%)
25 °C Single Treatment LiOH	1.8	720	-54%
25 °C Double Treatment LiOH	1.7	680	-57%
80 °C Single Treatment LiOH	0.7	260	-84%
80 °C Double Treatment LiOH	0.5	200	-87%

A single treatment with LiOH worked very well in reducing ASR, leading us to investigate multiple treatments of the sand with LiOH. All four samples had similar very steep increase in expansion over the first 2 days (Figure 9). However after two days, the mortar bars containing lithium treated sand deviated majorly from the control bar since their expansion is almost completely halted. After the first 14 days, 3 of the 4 mortar bars passed the 0.10% limit set by the ASTM C 1260 test (Figure 9). The room temperature single treatment mortar bar finished the 14 days slightly above the 0.10% threshold at 0.117%. This suggests that this sample contains close to the threshold amount of lithium silicate sufficient to inhibit ASR expansion. The mortar bar made using the room temperature twice coated sand came in slightly below the threshold at 0.095% and the single and double treatment at the elevated temperature had an expansion of 0.080% and 0.076%. These three mortar bars appear to act as if they contain aggregate that is not

prone to ASR. These mortar bars were then followed for an extended time to record any changes that might occur. The average expansion at the end of the 80 day test for the sand that was treated once at room temperature was 0.52% and it was 0.41% for the sand treated twice, a large reduction from the control that had an expansion of 0.95%. Note that in the two room temperature LiOH treated samples, the inhibited or flat phase of expansion ended after 15 days and then began to expand again at the same rate as the control mortar bar containing untreated sand. The tests performed with sand reacted at 80 °C had a drastic reduction of ASR expansion and after the initial rise at 2 days, the growth was nearly flat throughout the whole 80 day test. The single treated sample had an average expansion of 0.20% and the doubly treated test had an average expansion of 0.12% over the 80 days (Figure 10). We hypothesize the improved expansion in the elevated temperature samples is due to increasing the kinetics of the LiOH reaction with the sand in the initial treatments. This is borne out by the lithium analysis. Presumably, using longer reaction times for the room temperature treatments may also provide similar results.

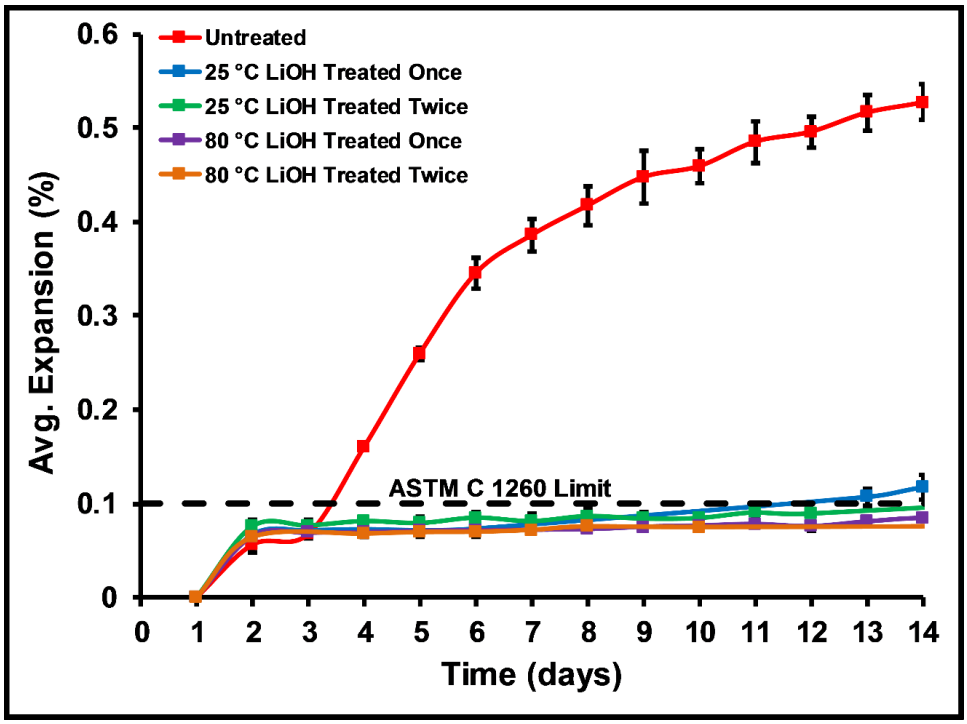

Figure 9: ASR test results for mortar bars using LiOH treated sand at room temperature and 80°C over 14 days.

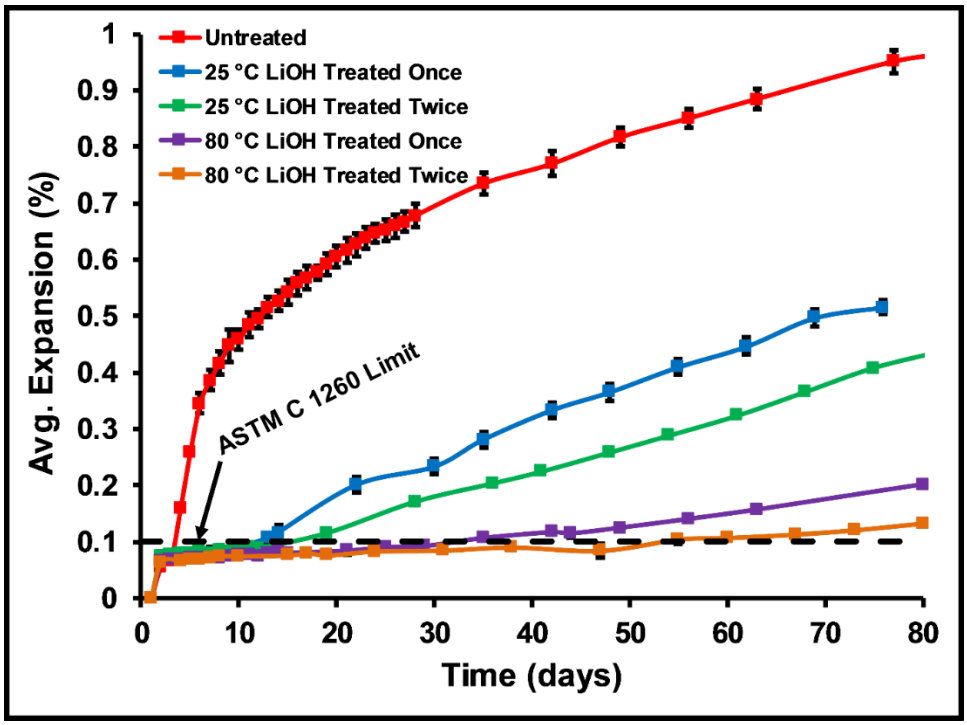

Figure 10: ASR test results for mortar bars using LiOH treated sand at room temperature and 80°C over 80 days.

Table 2: Percent reduction in ASR expansion over 14 and 80 days.

Treatment	14 days	80 days
Single Treatment $Ba(OH)_2$[15]	23%	17%
Double Treatment $Ba(OH)_2$[15]	45%	41%
$Ca(OH)_2$	14%	14%
25°C Single Treatment LiOH	78%	46%
25°C Double Treatment LiOH	81%	54%
80°C Single Treatment LiOH	84%	79%
80°C Double Treatment LiOH	86%	86%

Following the ASR expansion over 80 days, the expansion undergoes two separate rates of reactions. The initial reaction is a steep increase in expansion followed by the second rate that is a much slower increase in expansion. The various different minerals (chert and feldspar) that make up the Jobe sand could be the cause of these different rates of expansion.[17] In the untreated material, we see an initial increase with a slope of 0.0380 over the first 14 days and gradual slope increase after 45 days until the end of the experiment (80 days) of 0.0047. The work done by Cannon using single and double treatments of $Ba(OH)_2$ showed the slope over the first 14 days to flatten out, but

after 45 days slope for the single treatment is close to that of the untreated experiment and the double treatment has reduced 34% to 0.0031.[15] This trend can be seen with the treatment of $Ca(OH)_2$ and LiOH. These changes in expansion slopes can be found in Table 3. We can deduce that in terms of the $Ca(OH)_2$, as well as within the $Ba(OH)_2$ done by Cannon, that treatment of the aggregate impacts the initial highly reactive species on the surface of the aggregates, thus effects the sharpness of the expansion taking place over the first 14 days. It is not the same in the LiOH treatments. In these treatments, the slope was reduced significantly for the first 14 days and for the aggregate treated at room temperature there was an increase of slope as the reaction continues past the 45 day mark. In regards to the 80 °C treated aggregates, the change of slope was still significantly reduced from the untreated slope. The greatest slope reduction takes place with the LiOH double treatment at 80 °C. Table 3 summarizes the slopes of the treated materials over the different time frames, as well as the percent change from the untreated material.

Table 3: Slopes of ASR expansion and the percent change from the untreated material.

Treatment	Slope over the first 14 days	Slope from 45 days to 80 days	% change over 14 days	% change from 45 to 80 days
Untreated	**0.0380**	**0.0047**	**-**	**-**
Single Treatment $Ba(OH)_2$[15]	**0.0302**	**0.0042**	**-20.5%**	**-10.6%**
Double Treatment $Ba(OH)_2$[15]	**0.0206**	**0.0031**	**-45.8%**	**-34.0%**
$Ca(OH)_2$	**0.0350**	**0.0045**	**-7.9%**	**-4.3%**
25°C Single Treatment LiOH	**0.0043**	**0.0056**	**-88.7%**	**+19.1%**
25°C Double Treatment LiOH	**0.0022**	**0.0053**	**-94.2%**	**+12.8%**
80°C Single Treatment LiOH	**0.0012**	**0.0023**	**-96.8%**	**-51.1%**
80°C Double Treatment LiOH	**0.0008**	**0.0008**	**-97.9%**	**-83.0%**

Conclusion

It was possible to drastically reduce expansion due to the alkali-silica reaction within the mortar bars, and in some cases almost completely prevent ASR. Using $Ca(OH)_2$ to reactively neutralize the reactive aggregate, which is responsible for ASR within the concrete, led to a reduction of expansion by 14% within the first 14 days and

14% over the total 80 day testing period. This positive result could possibly be improved with additional treatments of the aggregate, but the low solubility of the $Ca(OH)_2$ leads to a difficulty of providing a highly-concentrated solution, requiring a large number of treatments. When the aggregate was treated with LiOH, as the neutralizing reactant, the ASR was limited even further. Since the use of $LiNO_3$ is already a standard practice, neutralization using LiOH was hypothesized to provide a similar response to the formation of ASR expansion, but reducing the amount of chemical necessary. Over the first 14 days of the standardized test, 3 of the 4 samples were within the passing 0.10% limit. The single room temperature treatment was slightly above the limit at 0.12%. Extending the test to 80 days the single room temperature treatment saw a total expansion reduction of 46%, while the room temperature doubly treated sample was reduced 54%. The final reduction of expansion for the mortar bar made with the sand that was treated once with LiOH at 80 °C was 79% and 86% for the sand that was treated twice. To summarize, treatments using $Ca(OH)_2$ showed positive results in limiting the effect of ASR on the mortar bars, but the solubility problems and the number of treatments necessary led us to investigate other metal hydroxides. The treatments with LiOH provided an aggregate that was shown to neutralize the reactive silica within known ASR prone sand into material that would not undergo ASR. This was all done with a small amount of chemical in a pre-treatment step. Long-term testing is needed on these treated aggregates to follow the expansion over a much longer period.

References

1. Association, P. C. How cement is made. cement.org/cement-concrete-applications/how-cement-is-made#.

2. Jeff Thomas, H. J. The Science of Cement. iti.northwestern.edu/cement/index.html.

3. Dirks, D. An FHWA Technical Update on Alkali-Silica Reactivity *Reactive Solutions* [Online], 2009. fhwa.dot.gov/pavement/concrete/reactive/v02issue02.cfm.

4. Ahlstrom, G. An FHWA Technical Update on Alkali-Silica Reactivity *Reactive Solutions* [Online], 2012. fhwa.dot.gov/pavement/concrete/reactive/v05issue04.cfm.

5. Pan, J.; Feng, Y.; Xu, Y.; Jin, F.; Zhang, C.; Zhang, B., Chemo-damage modeling and cracking analysis of AAR-affected concrete dams. *Science China Technological Sciences* 2013**,** *56* (6), 1449-1457.

6. Thaulow, N.; Jakobsen, U. H.; Clark, B., Composition of alkali silica gel and ettringite in concrete railroad ties: SEM-EDX and X-ray diffraction analyses. *Cement and Concrete Research* 1996**,** *26* (2), 309-318.

7. Dent Glasser, L. S.; Kataoka, N., The chemistry of 'alkali-aggregate' reaction. *Cement and Concrete Research* 1981, *11* (1), 1-9.

8. Diamond, S., A review of alkali-silica reaction and expansion mechanisms 2. Reactive aggregates. *Cement and Concrete Research* 1976, *6* (4), 549-560.

9. Fernandes, I.; Broekmans, M. A. T. M., Alkali–Silica Reactions: An Overview. Part I. *Metallography, Microstructure, and Analysis* 2013, *2* (4), 257-267.

10. Snellings, R.; Mertens, G.; Elsen, J., Supplementary Cementitious Materials. *Reviews in Mineralogy and Geochemistry* 2012, *74* (1), 211-278.

11. K. J. Folliard, R. B., T. Drimalas, S. Garber, J. Ideker, T. Ley, S. Williams, M. Juengar, M. D. A Thomas *Preventing ASR/DEF in New Concrete*; TxDOT project # 4085; 2006.

12. Shafaatian, S. M. H.; Akhavan, A.; Maraghechi, H.; Rajabipour, F., How does fly ash mitigate alkali–silica reaction (ASR) in accelerated mortar bar test (ASTM C1567)? *Cement and Concrete Composites* 2013, *37*, 143-153.

13. Diamond, S., Unique response of LiNO3 as an alkali silica reaction-preventive admixture. *Cement and Concrete Research* 1999, *29* (8), 1271-1275.

14. Islam, M. S.; Ghafoori, N., Experimental study and empirical modeling of lithium nitrate for alkali-silica reactivity. *Construction and Building Materials* 2016, *121*, 717-726.

15. Cannon, C. R. New technologies for the improvement of concrete properties with application in catalysis and homeland security. Ph.D. Dissertation, Oklahoma State Univeristy, Stillwater, OK, USA, 2014.

16. Phillips, W. J. Alkali Silica Reaction Mitigation Using High Volume Class C Fly Ash. University of Arkansas, 2015.

17. Thomas, M. D. A., Fournier, B., Folliard, K.J. *Selecting Measures to Prevent Deleterious Alkali-Silica Reaction in Concrete: Rationale for the AASHTO PP65 Prescriptive Approach*; The Transtec Group, Inc.: 2012.

18. ASTM C1260-14 Standard Test Method for Potential Alkali Reactivity of Aggregates; Mortar-Bar Method. ASTM International: 2014.

CHAPTER III

Development of Single Source Mixed Metal Pyruvic Acid Oxime Complexes for the Synthesis of Mixed Metal Oxides for the Use in the Remediation of Aqueous Arsenic.

Introduction

This chapter discusses the synthesis and characterization of mixed iron and zinc pyruvic acid oxime complexes and the mixed metal oxides derived from them. The metal oxides were used for sorption of arsenic species from aqueous solution. The synthesis of the single source precursors takes place via a ligand exchange reaction between a soluble metal salt and pyruvic acid oxime sodium salt (NaPAO). The synthesis of NaPAO can be achieved by the simple reaction of sodium pyruvate and hydroxylamine in water. The metal PAO complexes are thermally unstable and decompose at low temperature to small volatile organic fragments (CO_2, CH_3CN and H_2O) and the corresponding metal oxide (Scheme 1).[1]

It has been previously found that for many of the 3d transition metals (Fe^{2+}, Co^{2+}, Ni^{2+}, Cu^{2+}, and Zn^{2+}) are isostructural and adopt the identical binding motif of a 5-member metallocycle with chelation from the carboxylate oxygen to the metal ion center, as well as, from the nitrogen of the oxime group (Figure 1).[2,3]

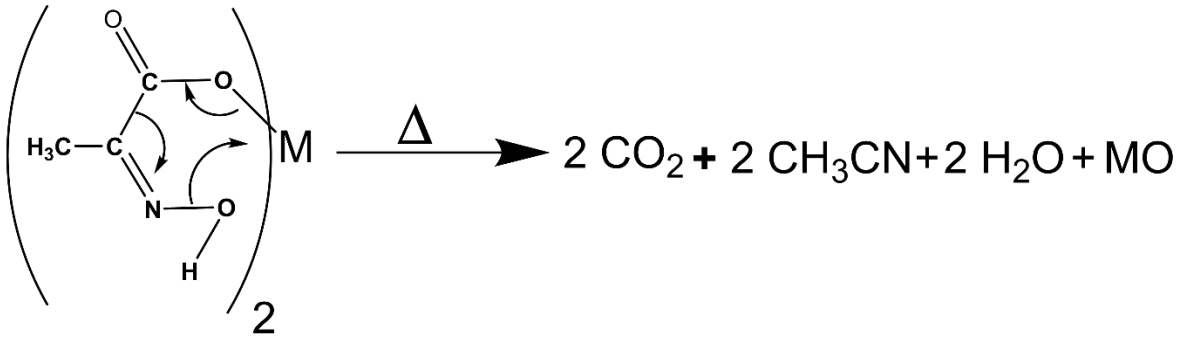

Scheme 1: Decomposition of a metal pyruvic acid oxime complex.

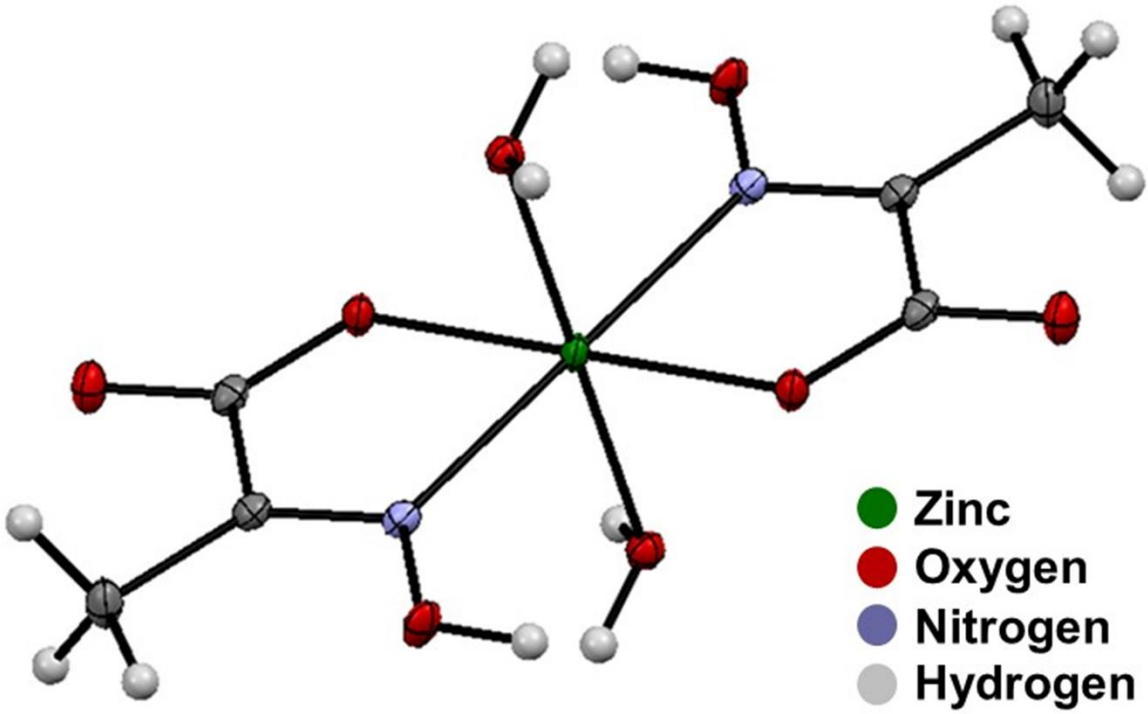

Figure 1: Crystal structure for $ZnPAO_2 \cdot 2H_2O$.[2]

The isostructural nature of the 3d transition metal pyruvic acid oxime complexes allows for the precipitation of the mixed metal complexes by use of a method described in the literature as the solid solution method.[4] This method is based on the ability of homogeneous mixed metal solutions to undergo co-precipitation, and as long as the final complexes for the metals are isostructural, allowing both metal ions to be present within the same lattice with random occupation of the metal sites. The close proximity of the metals allows for reduced diffusion distances that allows for improved temperature for the formation of mixed metal oxides.[5]

The Apblett research group has previously demonstrated achieving highly porous, nanocrystalline metal oxide materials through the low temperature decomposition of metal pyruvic acid oxime complexes.[2,3,6,7] Bagabas and coworkers investigated the thermal properties and spectroscopic characteristics of $Zn(PAO)_2$ and the ZnO obtained after calcination. An average crystallite size of the ZnO produced at 290 °C, was 6.2 nm with a surface area of 150 m^2/g.[8] In addition, published work by Georgieva has shown the ability to produce ceria precursors doped with either Sm^{3+}, Nd^{3+} or Th^{4+}. Using the co-precipitation method with NaPAO, the bimetallic precursor's stoichiometry could be controlled by controlling the initial molar ratio of the metal salt solution.[3]

The contamination of ground water with arsenic has become a major concern in many communities around the world. The largest source of contamination of groundwater comes from naturally occurring sources. Soluble inorganic species of arsenic includes the arsenate (5+) and arsenite (3+) forms. Both these inorganic species exhibit toxicity, but arsenite is considered to be the most toxic, with a lethal dose in the range of 1 to 3 mg/kg.[9] In pH neutral waters, arsenite is found in its acidic form (H_3AsO_3) while arsenate

is found in ionic forms ($H_2AsO_4^-$ and $HAsO_4^{2-}$).[10] The redox interconversion of arsenate and arsenite occurs naturally but at a very slow rate. This leads to contaminated waters having a variety of arsenic species present, making the development of a method for removal of arsenic difficult.[11] Countries that suffer from arsenic contamination in their ground water due to natural sources include Bangladesh, Chile, China, and the United States of America to name a few.[12] The exposure of people to this contaminated ground water results from drinking water, water used in food preparation, and water used for crops. Anthropogenic sources of arsenic in the environment come from a broad spectrum of industries including glass processing, textiles, pigments, and wood preservation.[12] The health effects of arsenic for an acute exposure can include gastrointestinal problems, numbness or tingling of extremities, and death, if the concentration is high enough. The more common issues stem from the long term low-level exposure that can cause mild to severe skin issues (Figure 2), bladder cancer, cardiovascular disease, and increased adverse pregnancy outcomes and infant mortality.[13]

Figure 2: Hyperkeratosis caused by long term exposure to arsenic contaminated drinking water.[13]

In 1993, the World Health Organization set water regulations for arsenic at a maximum contaminant level of 10 ppb. This guideline was put into place due to the evidence of arsenic being carcinogenic to humans.[14] The United States, under the regulation of the Environmental Protection Agency, set their maximum contaminate level for drinking water to 10 ppb to match the WHO standard in 2001.[15]

Varieties of techniques have been used to remove arsenic from contaminated water supplies. Some of these techniques include precipitation, ion exchange, reverse osmosis and adsorption.[16] Adsorption offers a cheap and effective method to remove arsenic by use of an insoluble material that takes advantage of specific surface features associated with the material. In most cases, the adsorption of the pollutant is achieved by physical attractions, but adsorption can also be achieved by weak chemical bonding.[16] Metal oxides are a cornerstone material for use in adsorption technologies because they

provide key features that are necessary for the adsorption process. These include insolubility, ease of synthesis, cost effectiveness, and the added advantage of the option of synthesizing these materials on the nanoscale.[17] Nanomaterials are simply defined as materials that fall into the size range of 1 to 100 nm. These materials provide unique properties that might not be shown in the bulk material.[17] Nano-scale metal oxides developed for remediation of pollutants provide additional benefits to a technique that is already widely used. Nano-scale metal oxides, like nanometric iron oxide, provide improved surface area, controlled morphology and magnetic properties. Synthesis of nanomaterials can be achieved through several routes, using physical methods such as high-energy ball milling, or chemical methods such as co-precipitation, the sol-gel method, or hydrothermal synthesis.[16-18] Materials that are used to remove arsenic from water are numerous but iron oxides are common. Iron oxides consist of various natural forms, such as magnetite, hematite, and maghematite. These various forms of iron oxide provide diverse customization, low toxicity, and high abundance that have made iron oxides a perfect option for arsenic remediation.[17,19]

The goal for this project was to develop mixed iron and zinc precursors that when decomposed, at low temperatures, will lead to iron and zinc mixed metal oxide nanomaterials that could be used to remove arsenate and arsenite from stock aqueous solutions, real life samples, and fruit juice. Treating real life samples and fruit juice allowed for the investigation into how the materials would function in complex matrices or in the presence of different competing ions. Being able to control the stoichiometry of the iron and the zinc allows for the tailoring of the material to improve arsenic uptake and the determination of how composition affects the uptake of arsenate and arsenite.

Introducing softer zinc ions into the metal oxide was predicted to improve arsenic uptake, especially of arsenite. Lewis hard/soft acid/base rules define arsenite as being a soft Lewis base and arsenate as being a borderline Lewis base.[20,21,22]

Materials

The pyruvic acid (Tokyo Chemical Industry, Co., LTD.), sodium carbonate (Malinckrodt), hydroxylamine hydrochloride (Alfa Aesar), zinc chloride (Alfa Aesar), iron (II) chloride tetrahydrate (Alfa Aesar), cobalt (II) chloride hexahydrate (Fisher Scientific) used in the synthesis of the iron/zinc pyruvic acid oxime precursors were used as purchased with no further purification. Arsenic trioxide (Mallinckrodt), sodium hydrogen arsenate heptahydrate (Alfa Aesar) and potassium dihydrogen arsenate (Sigma) were used, as purchased, to make stock solutions of arsenic for the remediation trials. 1,000 ppm arsenic, iron and zinc standards were purchased from Ricca Chemical Company for making standards for the microwave plasma atomic emission spectrometer. Unless otherwise stated, all reactions take place at room temperature (23 °C) in deionized water (18 MΩ·cm) obtained from a Barnstead E-Pure System.

Synthesis of the Metal Pyruvic Acid Oxime Complexes

To produce the desired metal pyruvic acid oxime salts, a simple metathesis reaction was performed starting with sodium pyruvic acid oxime monohydrate ($NaPAO{\cdot}H_2O$) and a soluble metal salt. $NaPAO{\cdot}H_2O$ was synthesized following the method previously reported by the Apblett research group.[6] This involves slow addition of Na_2CO_3 to an aqueous solution of sodium pyruvate and hydroxylamine hydrochloride. The solution was stirred for 1 hour and left refrigerated at 10 °C for several days until

colorless needle-like crystals formed. The crystals were separated by vacuum filtration and rinsed with 100 mL of deionized H_2O and left to dry in ambient air. Single metal pyruvic acid oxime complexes were prepared (Fe^{2+}, Co^{2+}, and Zn^{2+}) by following previously published methodology, where the corresponding metal salt was mixed with a sodium pyruvic acid oxime solution in a 1:2 molar ratio. After 24 hours, a powder is precipitated that was subsequently analyzed using a variety of analytical techniques.[2-3] The synthesis of the mixed metal PAO complexes was achieved by controlling the stoichiometry of the metal salts in the initial reaction solution. By changing the metal ratios to 1:1 or 1:2 etc. while still keeping the overall molar ratio of metal to $NaPAO{\cdot}H_2O$ the same (1:2) final materials that exhibited specific metal ratios were produced.

Preparation of 2:1 Fe:Zn(PAO)$_2$. A $FeCl_2$ solution (10 mmol) was combined with a $ZnCl_2$ solution (5 mmol) and stirred. The mixed metal solution was added to a NaPAO solution (30 mmol) and mixed thoroughly. The solution was then left overnight to allow the reaction to reach completion. A bright greenish-yellow solid was precipitated. The solid was obtained by vacuum filtration and the air-dried and stored at room temperature. The reaction produced 4.70 g resulting in a yield of 77%. IR (cm^{-1}): 3057(m, br), 2823(m, br), 2263(w, br), 1668(m), 1639(s), 1533(w), 1477(m), 1433(w), 1387(m), 1361(s), 1212(m), 1041(s), 855(vs), 764(vs), 692(s), 559(m).

Preparation of 1:1 Fe:Zn(PAO)$_2$. A $FeCl_2$ solution (5 mmol) was combined with a $ZnCl_2$ solution (5 mmol) and mixed until homogenous. The mixed metal chloride solution was then added to a NaPAO solution (20 mmol) and thoroughly mixed. The solution was then left overnight to allow the reaction to reach completion. A bright greenish-yellow solid was precipitated out of the solution. The solid was vacuum filtered,

air dried and then stored at room temperature. The reaction produced 2.90 g resulting in a yield of 96.5%. IR (cm^{-1}): 3061(m, br), 2825(m, br), 2257(w, br), 1669(m), 1641(s), 1532(w), 1478(m), 1431(w), 1387(m), 1361(s), 1213(s), 1042(s), 854(s), 763(vs), 693(s), 558(m).

Preparation of 1:2 Fe:Zn(PAO)$_2$. A $FeCl_2$ solution (5 mmol) was combined and thoroughly mixed with a $ZnCl_2$ solution (10 mmol). The mixed metal solution was then added to a NaPAO solution (30 mmol) and stirred. The solution was then left overnight to allow the reaction to reach completion. A greenish-yellow solid was precipitated out of solution. The solid was vacuum filtered, air-dried and then stored at room temperature. The reaction produced 4.23 g resulting in a yield of 87%. IR (cm^{-1}): 3061(m, br), 2824(m, br), 2257(w), 1670(m), 1641(s), 1532(w), 1479(m), 1361(s), 1213(s), 1043(s), 854(vs), 763(vs), 698(s), 558(m).

Pyrolysis of Mixed Metal Pyruvic Acid Oxime Complexes

Pyrolysis of the metal PAO complexes took place in a Vulcan temperature programmable muffle furnace. The pyrolysis was done in ambient air at temperatures that corresponded to the decomposition temperature determined by the TGA experiments. The solid was collected for characterization and further experiments.

Pyrolysis of 2:1 Fe:Zn(PAO)$_2$. A sample of 0.100 g of 2:1 Fe:Zn(PAO)$_2$ was added to an empty 125 mL Erlenmeyer flask and loosely plugged with glass wool. The sample was placed in a muffle furnace and heated to 350 °C to produce .034 g (34%) of a brown solid. IR (cm^{-1}): 3367(w, br), 1471(w), 1367(w), 551(w), 534(w).

Pyrolysis of 1:1 Fe:Zn(PAO)$_2$. A sample of 0.107 g of 1:1 Fe:Zn(PAO)$_2$ was added to an empty 125 mL Erlenmeyer flask that was loosely plugged with glass wool to reduce loss of sample. The sample was heated for 4 h to 350 °C in the muffle furnace to yield 0.032 g (29.9%) of a brown solid. IR (cm^{-1}): 3382(w, br), 1488(w), 1382(w), 541(w), 526(w).

Pyrolysis of 1:2 Fe:Zn(PAO)$_2$. 0.103 g of 1:2 Fe:Zn(PAO)$_2$ was heated for 4 h at 350 °C in a 125 mL Erlenmeyer flask that was loosely plugged with glass wool to reduce loss of sample. The pyrolysis yielded .031 g (30.1%) of a light brown powder. IR (cm^{-1}): 3347(w, br), 1474(w), 1382(w).

Characterization

Infrared spectra were obtained of both the PAO complexes and the thermal decomposition products using a Nicolet iS50 FT-IR spectrometer. Thermal gravimetric analysis was performed on a Mettler-Toledo TGA/DSC 1 instrument. Sample sizes used were between 7 and 12 mg and experiments were performed in flowing dry air. The temperature range used was 25 °C to 700 °C, unless otherwise stated, and a temperature ramp of 5 °C per minute was utilized. X-ray diffraction for both the metal pyruvic acid complexes and the oxides were collected at Oklahoma State University – Tulsa using a Bruker AXS D8 Discover X-ray diffractometer with a GADDS detector. Scanning electron microscope (SEM) images were obtained on a FEI Quanta 600 field emission gun environmental scanning electron microscope. An Agilent 4200 microwave plasma atomic emission spectrometer was used to determine concentrations of arsenic within the aqueous samples and the iron and zinc content of the mixed precursors.

Results and Discussion

Synthesis of PAO complexes

The synthesis of the metal PAO complexes starts with the synthesis of NaPAO·H_2O following a procedure from a previously published study by Apblett and coworkers.[6] In this synthesis, hydroxylamine is produced in situ from the reaction of its hydrochloride with sodium bicarbonate. A second equivalent of sodium bicarbonate deprotonates the pyruvic acid. The pyruvate then reacts with hydroxylamine to produce NaPAO·H_2O that crystallizes as long needle like crystals (Scheme 3). These crystals were collected by filtration and then air-dried.

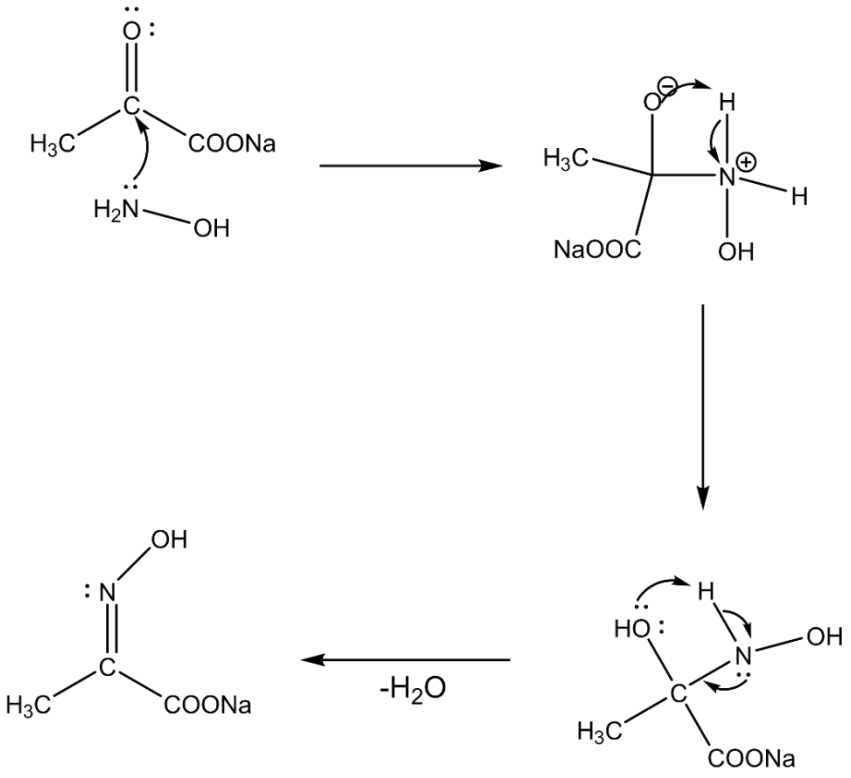

Scheme 2: Proposed mechanism of oxime formation in the reaction of sodium pyruvate and hydroxylamine.

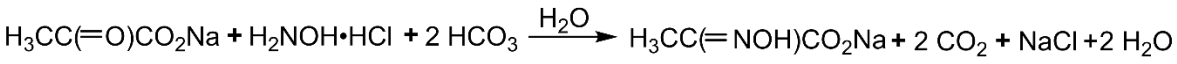

Scheme 3: Synthesis of NaPAO·H_2O.

Metal PAO complexes were synthesized via a ligand exchange with the metal chlorides and NaPAO (Scheme 4). This method was adapted from work that was used by Georgieva and coworkers to produce bimetallic PAO complexes for the synthesis of Nd^{3+}, Sm^{3+}, and Th^{4+} doped ceria.[3]

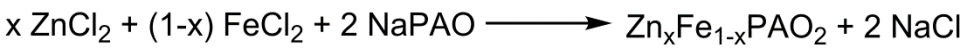

Scheme 4: Synthesis of iron and zinc PAO complex.

Thermal gravimetric analysis of the precursors was performed to determine the decomposition temperatures. Apblett and coworkers have shown that the pyruvic acid oxime ligand decomposes at low temperatures.[6] It was expected that the mixed metal PAO complexes would follow the same type of decomposition pathways that were observed for $Fe(PAO)_2$ and the $Zn(PAO)_2$ in previous work.[2-3] This pathway involves a single decomposition step where the loss of both the ligands takes place at the same time in the case of $Fe(PAO)_2$. $Zn(PAO)_2$, however, appears to lose its ligands in stepwise fashion. When the ligand decomposes, it produces volatile organic fragments (CO_2 and CH_3CN) and water (Scheme 1).[6] Decomposition for the three precursor materials starts at around the same temperature (100 °C) and around 350 °C the ligand is completely removed. Depending on the iron content, there is a small weight loss at higher temperature due to dehydroxylation. This weight loss is prominent in $Fe(PAO)_2$, but is

absent for $Zn(PAO)_2$. The temperature of 350 °C was chosen as the temperature used to calcine the precursors. There are visual color changes that take place as the precursors are calcined at 350 °C. All three precursors start out as a bright greenish-yellow powder (Figure 3) and after calcination they turn a shade of brown (Figure 4).

Figure 3: 1:1 Fe:Zn PAO complex.

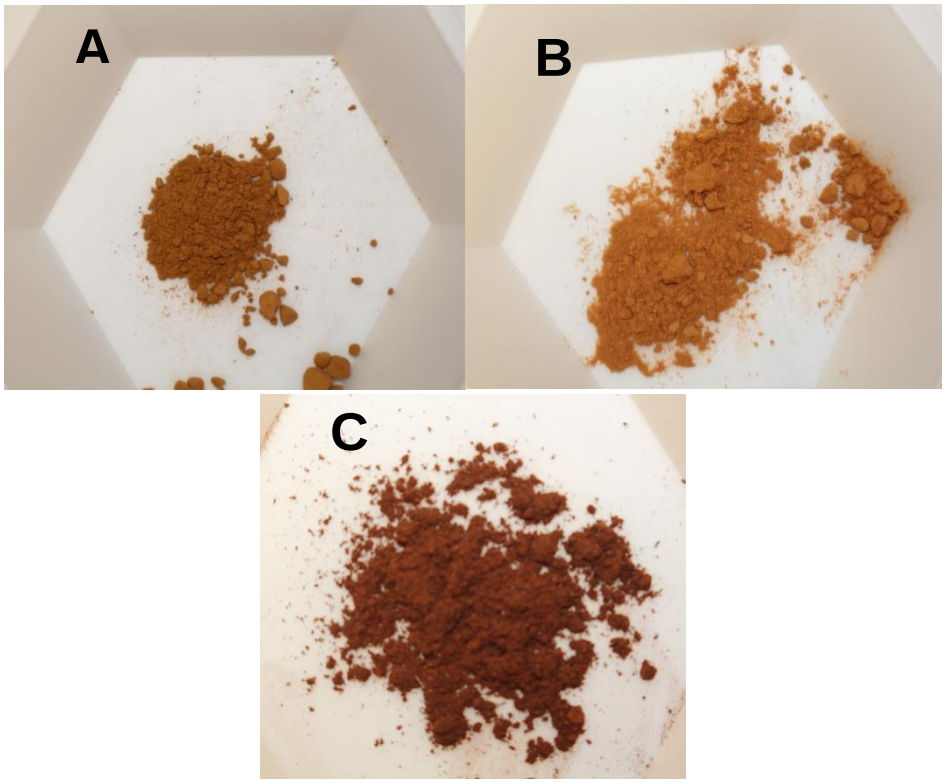

Figure 4: Visible color changes of the PAO precursors after calcination at 350 °C; 1:1 Fe:Zn (A), 1:2 Fe:Zn (B), 2:1 Fe:Zn (C).

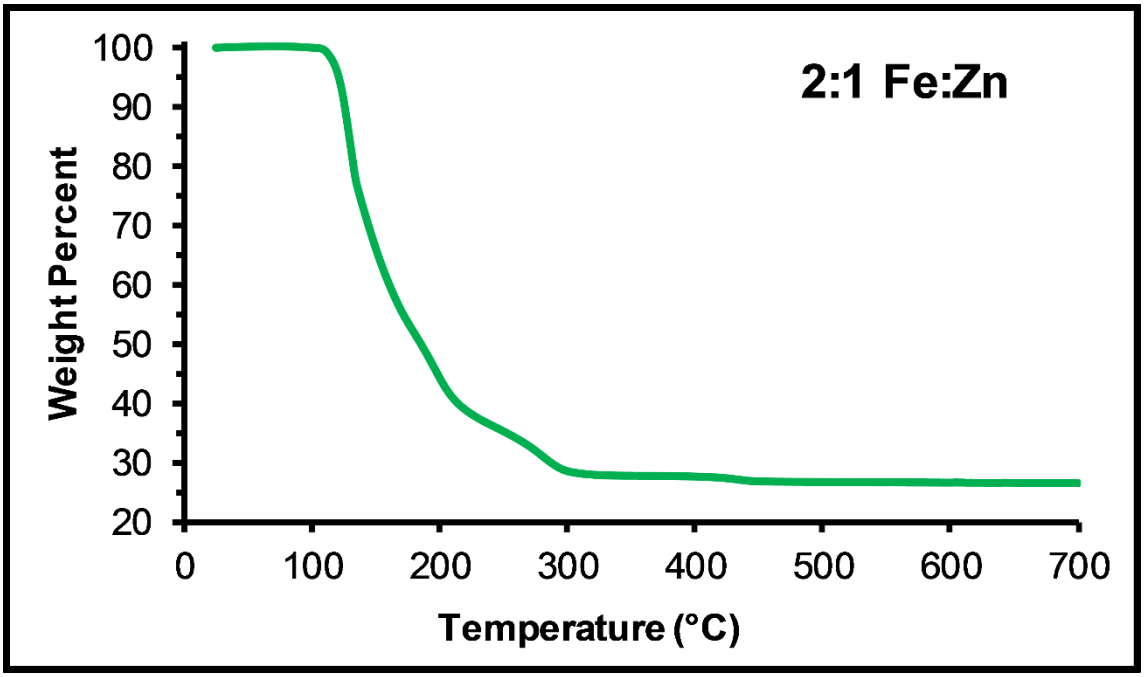

Figure 5: TGA trace for 2:1 Fe:Zn PAO complex heated in air at 5 °C/min.

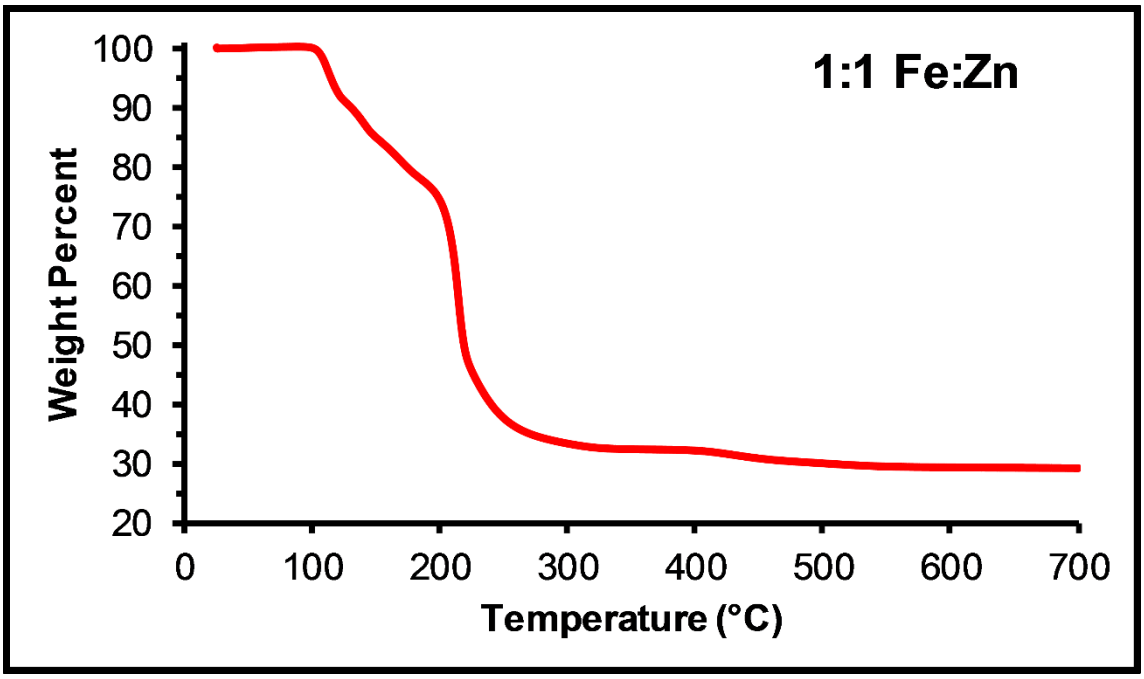

Figure 6: TGA trace for 1:1 Fe:Zn PAO complex heated in air at 5 °C/min.

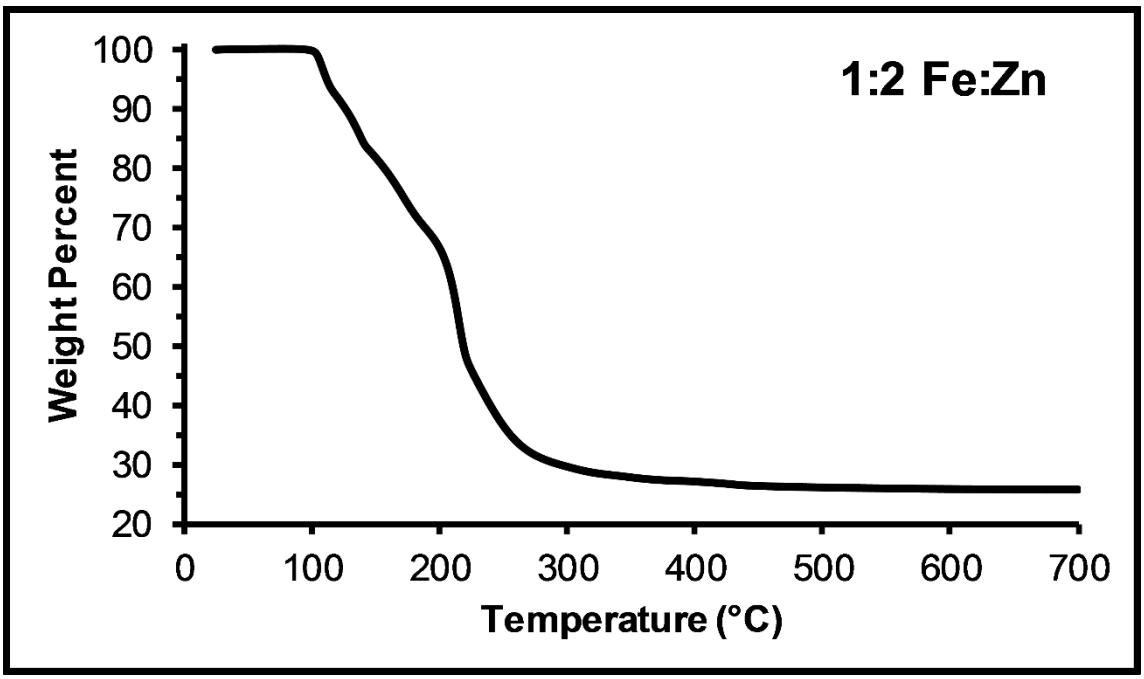

Figure 7: TGA trace for 1:2 Fe:Zn PAO complex heated in air at 5 °C/min.

The molar ratios of zinc and iron in each of the three final mixed metal oxides was determined by MP-AES. Initially, 0.050 g of material was digested using 30 mL of 5 M HCl at 80 °C until the volume of the flask was approximately 0.5 mL. When this volume was achieved, the sample was then diluted to 5 mL using deionized water. These samples were then diluted again to bring the concentration of the solution into the calibrated range of the instrument. The calibrated range was 1 to 20 ppm for both iron and zinc determinations. The MP-AES was calibrated using zinc standards that were diluted from stock Alfa Aesar 1,000 ppm zinc standard solutions. The analytical results for the molar ratios are summarized in Table 3. The 1:1 Fe:Zn ratio was determined to be zinc rich with a molar ratio of iron to zinc of 1:1.33. In the case of the 1:2 Fe:Zn and the 2:1 Fe:Zn the found iron to zinc ratios were 1:1.86 and 1.90:1. The final mole percent of the material is affected by the solubility of the $Fe(PAO)_2$ precursor. $Fe(PAO)_2$ is slightly soluble in water (0.113 g/L) while $Zn(PAO)_2$ has no measurable solubility. Surface areas were measured for all of the mixed metal oxides using nitrogen physisorption via the BET method. The surface areas are reported in Table 3. The composition has a marked effect on the surface area of the metal oxide. The samples with either higher or lower zinc composition either had significantly lower surface areas but were still high in comparison to normal third row transition metal oxides.

Table 1: Surface areas and the molar ratios of Fe and Zn within the mixed metal oxides.

Mixed Metal Oxide	Zn Mole Percent	Surface Area (m^2/g)	Ceramic Yield
Fe_2O_3	0	126 ± 11	28%
2:1 Fe:Zn	35	52 ± 3	34%
1:1 Fe:Zn	57	108 ± 22	30%
1:2 Fe:Zn	71	83 ± 4	30%
ZnO*	100	42	26%

*Experimental values obtained from previously published work.[7]

The highest surface area was for the pure iron oxide, but this result may be skewed by the presence of FeOOH (Figure 8). Among the mixed metal oxides, there is a maximum at $\chi_{Zn} = 0.57$. The composition $Fe_{0.29}Zn_{0.71}O_{1.15}$ is expected to have a low surface are because its proximity to the spinel composition. $ZnFe_2O_4$, is expected to allow it to sinter more easily. The sample, highest in zinc content, is expected to have a higher surface area then ZnO since the iron is expected to prevent sintering of zincite. Apparently, these phenomena reach the maximum in resistance to sintering at approximately 1 Zn : 1 Fe, where there is no clear preference for the formation of spinel or zincite nanocrystals.

Infrared spectra were obtained for the three PAO complexes to identify characteristic features of the precursors. The vibrational frequencies from the IR spectra of the corresponding single metal precursors and the mixed metal precursors are

summarized in Table 1. In all cases except the asymmetric carboxylate stretch, the infrared sorptions resembled those of $Fe(PAO)_2$ more than they did $Zn(PAO)_2$.

Table 2: Characteristic IR frequencies (cm^{-1}) for the PAO complexes.

Compound	$\nu_{(C=N)}$	$\nu_{as\ (COO)}$	$\nu_{s\ (COO)}$	$\nu_{(N—O)}$
$ZnPAO_2$ [7]	1680	1650	1395	1060
$Fe_{0.29}Zn_{0.71}PAO_2$	1670	1641	1387	1042
$Fe_{0.43}Zn_{0.57}PAO_2$	1669	1641	1387	1042
$Fe_{0.65}Zn_{0.35}PAO_2$	1667	1638	1386	1040
$FePAO_2$ [2]	1668	1650	1389	1045

When comparing infrared spectra for molecules that contain a carboxylate functionality one key observation that can be made is an insight into the structure around the carboxylate functional group. Carboxylates adopt four different conformations depending on the overall structure of the carboxylate group, type of solvent used, nature of the ligand, and which metal ion is present.[23,24] These conformations include uncoordinated, monodentate, bidentate, and bridging and are depicted in Scheme 5.

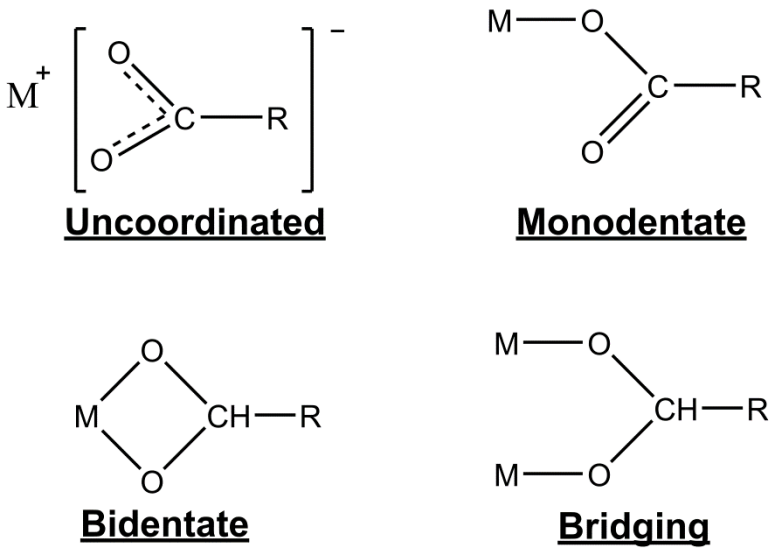

Scheme 5: The possible options for binding behavior of carboxylates.

The various binding modes leads to a measurable difference between the frequencies of the asymmetric carboxylate and symmetric carboxylate stretching bands.[24] The difference between these frequencies for the monodenate and uncoordinated modes tend to be the highest (>250 cm^{-1}), followed by bidentate (>225 cm^{-1} but >250 cm^{-1}), and finally bridging has the lowest difference (>225 cm^{-1}).[2] In Table 2, the differences of the asymmetric and symmetric carboxylate stretches are listed. The large value for all three complexes is strong evidence that the coordination of the carboxylate to the metal is monodentate.

Table 3: Change in $\nu_{as\ (COO)}$ and $\nu_{s\ (COO)}$.

Compound	$\Delta\nu_{(COO)}$*
$Fe_{0.65}Zn_{0.35}PAO_2$	252 cm^{-1}
$Fe_{0.43}Zn_{0.57}PAO_2$	254 cm^{-1}
$Fe_{0.29}Zn_{0.71}PAO_2$	254 cm^{-1}

*$\Delta\nu_{(COO)}$ was calculated from $\Delta\nu_{(COO)} = \nu_{as\ (COO)} - \nu_{s\ (COO)}$

X-ray powder diffraction was performed on the oxide materials to identify the crystalline phases present, but the mixed metal oxide's diffraction patterns showed that they were amorphous materials. This demonstrates the utility of the low temperature synthesis of mixed metal oxides where large scale diffusion of metal ions does not occur and formation of a crystalline product is prevented. Instead, a solid solution of zinc and iron oxides is derived from the solid solution present in the precursor. There may be some localized ordering of ions but there is definitely no long-range order. The XRD pattern of iron oxide from the decomposition of the $Fe(PAO)_2$ precursor is shown in Figure 8. It can be seen that the material is crystalline and has a match in the database from the International Centre for Diffraction Data for γ-Fe_2O_3. The low intensity broad peaks not due to hematite are from the presence of FeOOH, possibly on the surface of the hematite. As noted earlier, this phase likely contributes to the elevated surface area of the product.

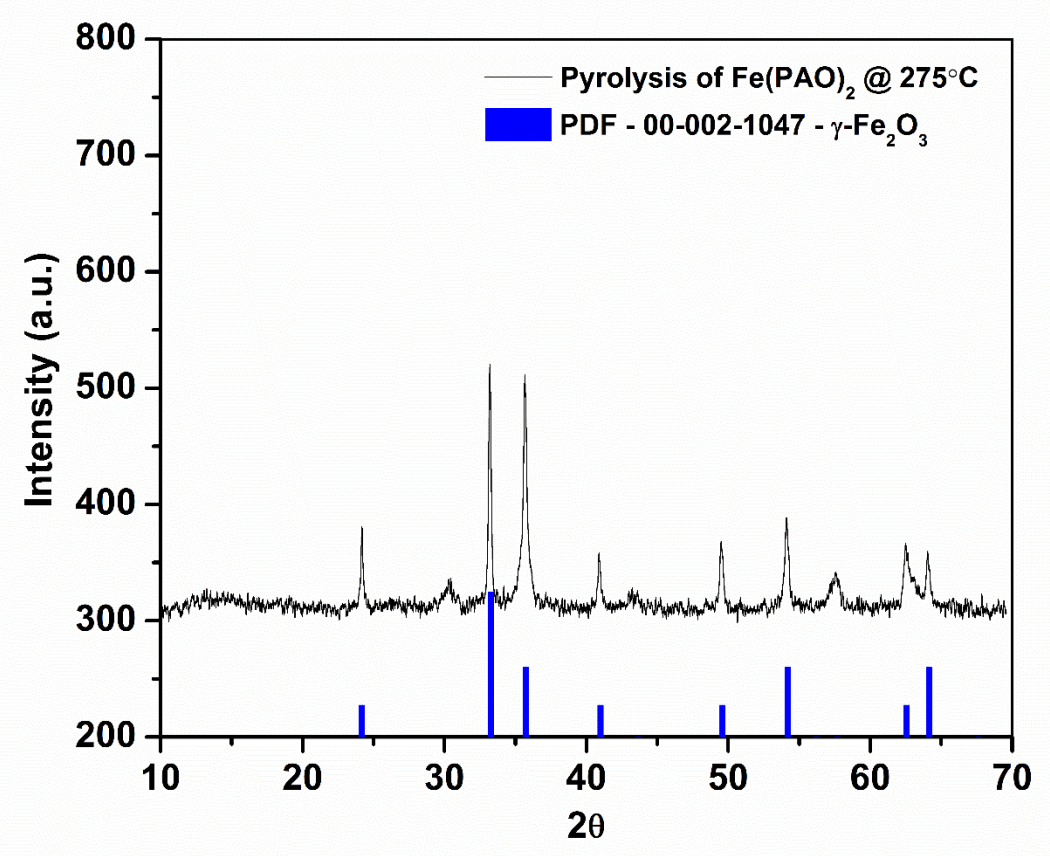

Figure 8: X-ray diffraction pattern for $Fe(PAO)_2$ after decomposition at 275 °C and the matching PDF from the ICDD.

Scanning electron microscopy was used to provide insight on the morphological and surface features of the oxide materials and their precursors. All three precursor materials have ribbon or sea urchin type morphologies with smooth surfaces. After calcination, the morphology is retained but instead of the smooth surfaces, the surfaces have become severely cratered. This cratering helps to provide increased surface area for the final materials.

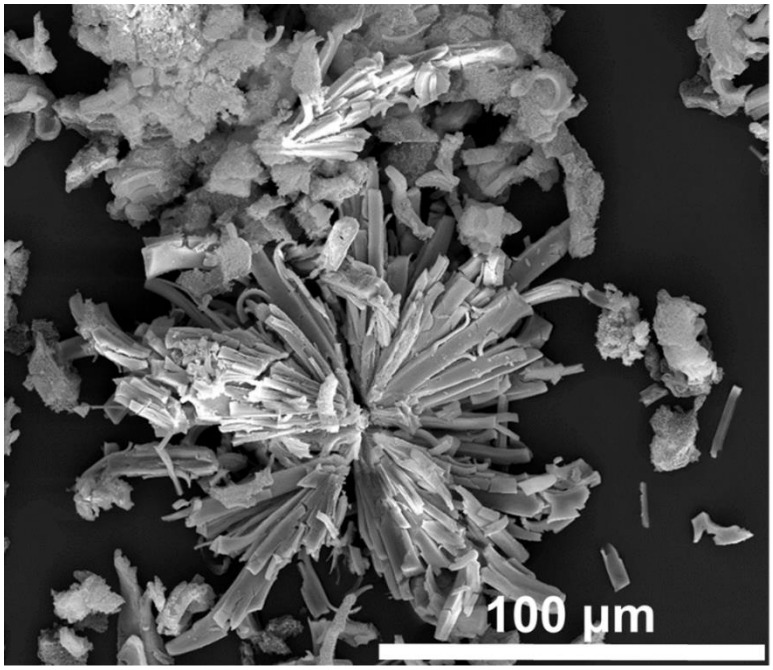

Figure 9: Scanning electron micrograph of 1:2 Fe:Zn PAO precursor.

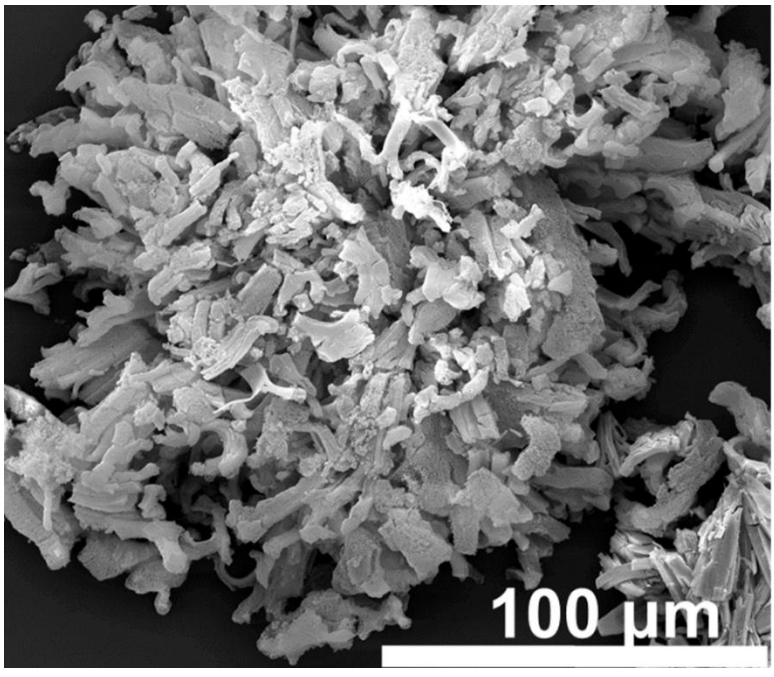

Figure 10: Scanning electron micrograph of 1:2 Fe:Zn after calcination at 350 °C.

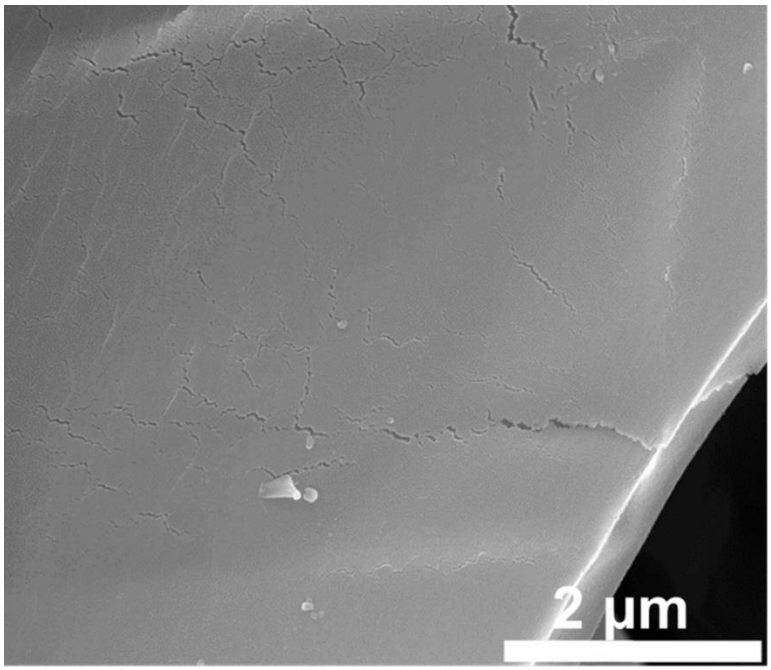

Figure 11: Scanning electron micrograph of 1:2 Fe:Zn PAO precursor.

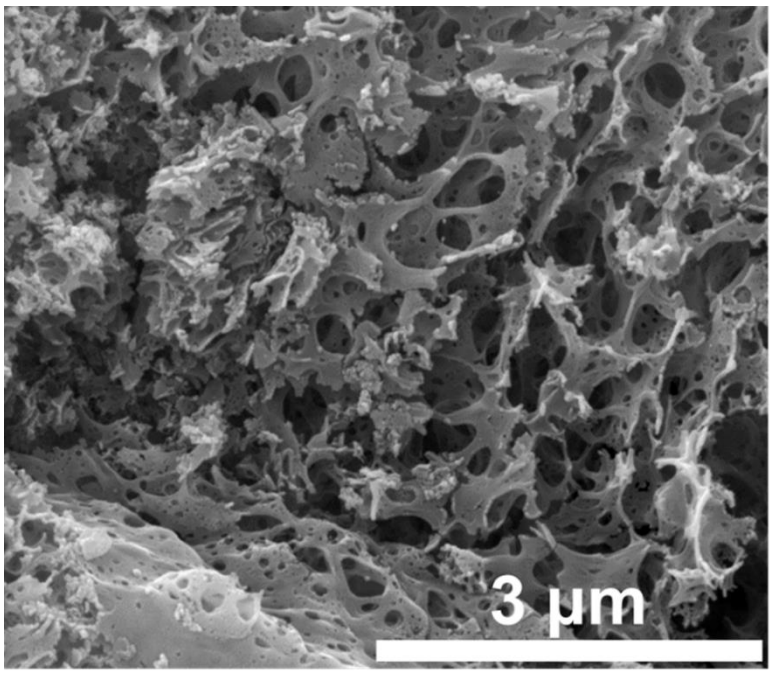

Figure 12: Scanning electron micrograph of 1:2 Fe:Zn after calcination at 350 °C.

Mixed metal oxides for arsenic remediation

Stock arsenic solutions were made by dissolving the corresponding arsenic salts in deionized water. Sodium hydrogen arsenate was used for the monobasic stock solution, potassium dihydrogen arsenate was used for the dibasic stock solution, and arsenic trioxide was used for the arsenite stock solution. Both arsenate solutions were mixed until all of the solid material had dissolved. In the case of the arsenite solution, the solubility of As_2O_3 is low, making it necessary to let the solution mix for 3 to 5 days. This solution can also be heated to increase dissolution of the As_2O_3. After several days of stirring, the solution was filtered to remove any undissolved solid. The concentrations of the stock solutions were determined via MP-AES. The wavelength used on the MP-AES for arsenic determination was 193.70 nm. Initial concentrations for both arsenate and arsenite stock solutions along with starting pHs are reported in Table 4.

Table 4: Initial concentration and pH of the stock arsenic solutions.

Stock Solution	Concentration (ppm)	pH
Monobasic Arsenate	102	4.5
Dibasic Arsenate	109	8.1
Arsenite	110	6.7

Calibration of the MP-AES was achieved using dilutions from 1,000 ppm standard solutions purchased from RICCA Chemical Company. The standard calibration range for high concentration solutions of arsenic was from 1 to 20 ppm. In the case of solutions that were below this standard calibration range, the use of a hydride generation was used to determine concentrations in the 10 to 500 ppb range. Hydride generator

involved the use 1% L-cysteine and 1% HCl for 1 hour as a pre-reductant to reduce any As^{V} species to As^{III} and then further reduction is caused by NaOH stabilized sodium borohydride (1.25%) to produce arsine gas.[25] This reduction to arsine has the advantage of being achieved with low acid concentrations. The accepted mechanism for the formation of the hydride is described below in Scheme 6. Producing arsine in this manner for low concentrations of arsenic allows for the reduction of any interference that might occur from high levels of acid within the sample as well as reduction of the amount of interference from other elements.[26]

$$2\ \text{Cys-SH} + H_3AsO_4 \longrightarrow 2\ \text{Cys-S-S-Cys} + As(OH)_3 + H_2O$$

$$3\ \text{Cys-SH} + As(OH)_3 \longrightarrow As(\text{-S-Cys})_3 + 3\ H_2O$$

$$As(\text{-S-Cys})_3 + 3\ BH_4^- \longrightarrow AsH_3 + 3\ BH_3 + 3\ \text{Cys-S}^-$$

Scheme 6: Reduction from arsenate to arsine by pre-reduction step of L-Cysteine and BH_4^-.[26]

Various amounts of the three bimetallic oxides as well as iron oxide from the decomposition of $Fe(PAO)_2$ were used to treat 20 mL of the 100 ppm arsenic stock solutions. All treatments were carried out in 20 mL scintillation vials and were performed at room temperature (23 °C). The length of the treatments was determined to be 3 days by following the concentration of the solution and identifying the time required for equilibrium to be reached. All experiments were performed without altering the pH or the temperature throughout the duration of the treatments. Samples were mixed by use of a mechanized rotor. At the end of the treatment all samples were filtered using 25 mm syringe filters with 0.2 μm nylon membranes and were then diluted to be analyzed by

MP-AES. 50 mg treatments are reported below to demonstrate the change in concentration after treatment of the arsenic containing solutions. Notably, the amount of $H_2AsO_4^-$ removed increased linearly with the mole fraction of zinc in the sorbent (Figure 14).

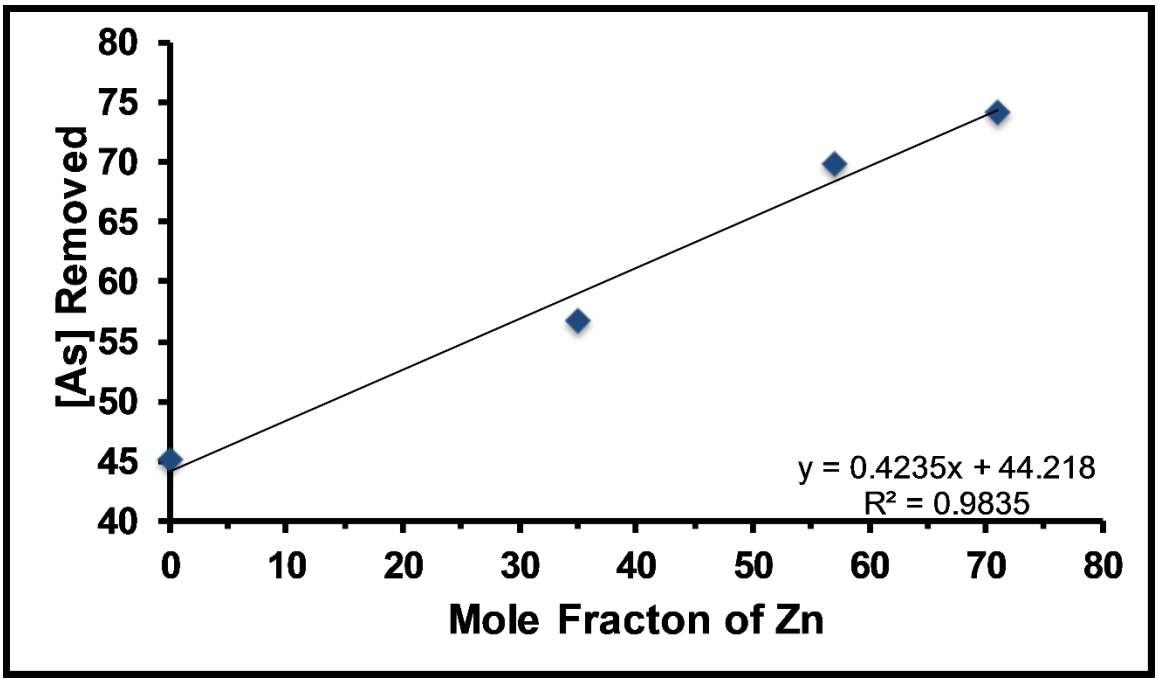

Figure 13: The linear trend of the increase in $H_2AsO_4^-$ removal with increasing mole fraction of zinc.

There was an increase of approximately 4.24 ppm of arsenic removed occurred with every 10% increase for zinc in the metal oxide. However, the sorption of the arsenate at higher pH ($HAsO_4^{2-}$) showed no statistical differences between the different bimetallic oxides and these all performed poorly compared to pure Fe_2O_3. Fe_2O_3 was also the best performing sorbent for arsenite, but aside from $Fe_{0.65}Zn_{0.35}O_{1.33}$, the differences were not statistically significant. It may be concluded that pH plays an important role in sorption by these metal oxides and only at lower pH is it possible to discern a change in

arsenic sorption with changing composition of the sorbent. Most notably, the higher the surface area of the sorbents corresponds to a higher arsenic adsorption. From this, it may be concluded that the sorption of the arsenic species relies on the concentration of active sites on the surface and the total surface area.

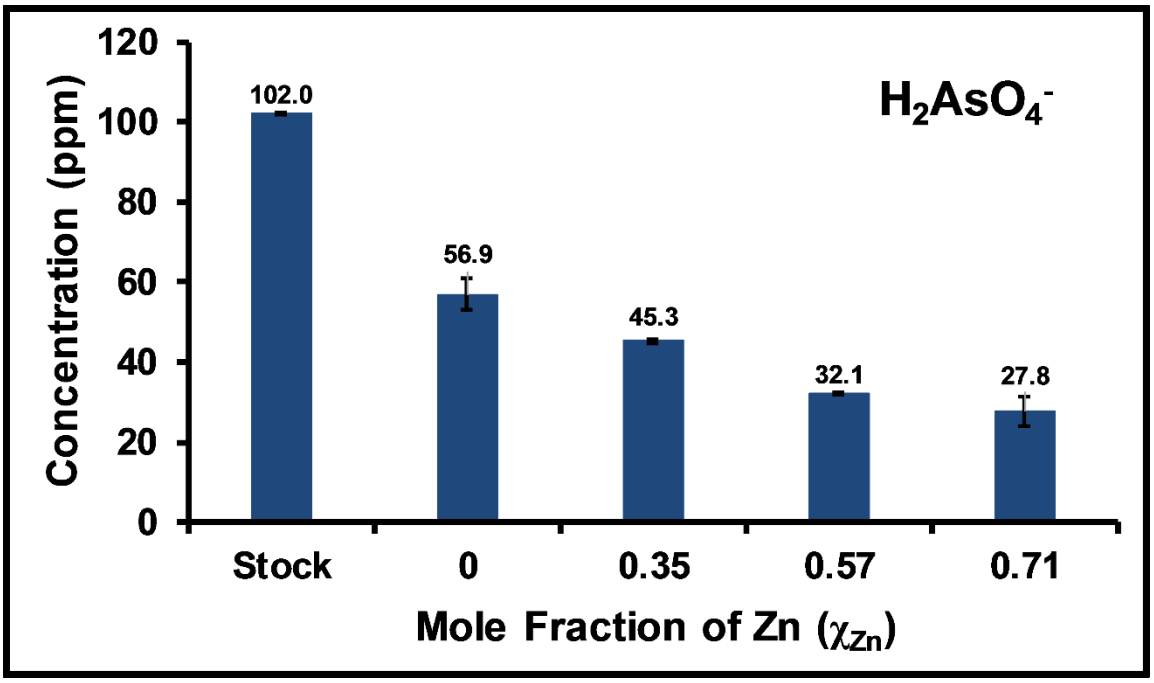

Figure 14: Change in arsenate ($H_2AsO_4^-$) concentration after a 3 day treatment by 50 mg of the metal oxides.

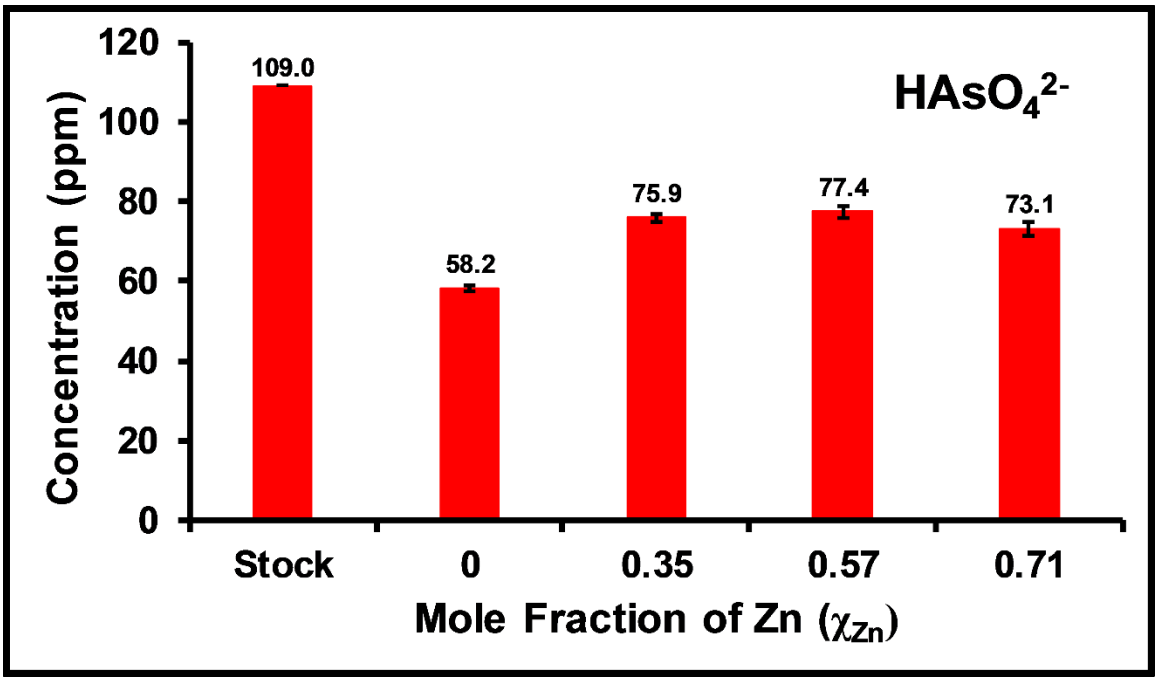

Figure 15: Change in arsenate ($HAsO_4^{2-}$) concentration after a 3 day treatment by 50 mg of the metal oxides.

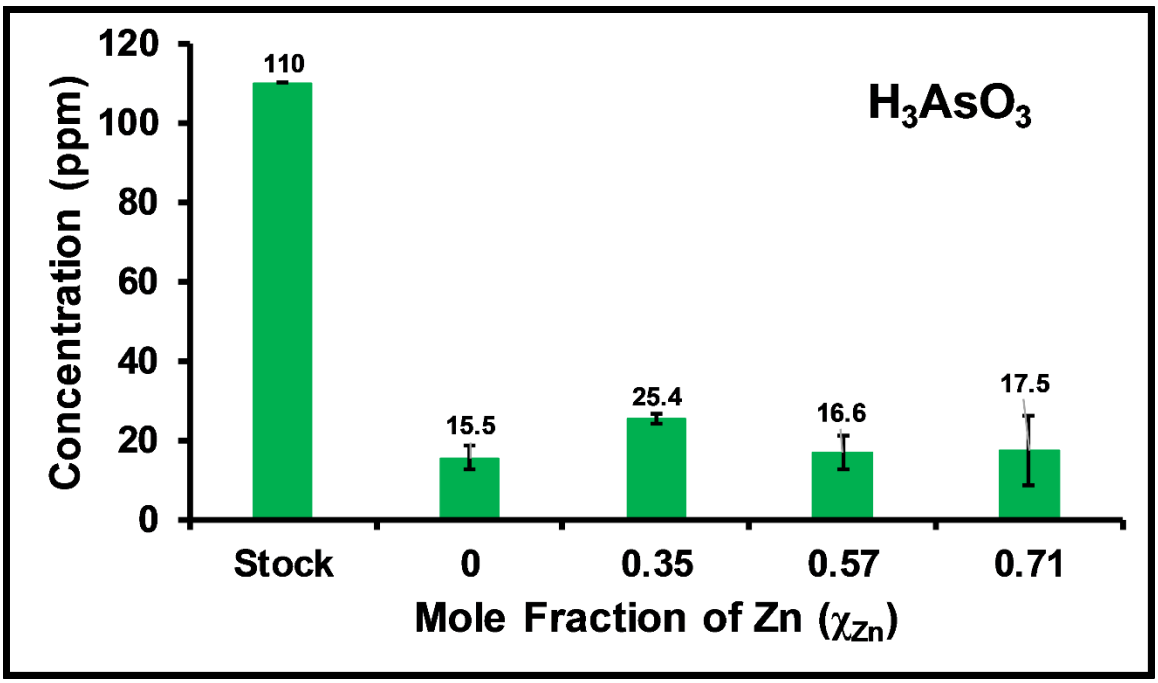

Figure 16: Change in arsenite (H_3AsO_3) concentration after a 3 day treatment by 50 mg of the metal oxides.

To determine the sorption capacities of the sorbents, the amount of sorbent added was varied while keeping the concentration of the stock solution constant. After three days, the filtrate of the treated solution was diluted and analyzed by MP-AES. The Langmuir and Freundlich adsorption isotherm models were applied to this data to solve for maximum uptake capacity. The Langmuir adsorption model is often used to characterize the adsorption onto the surface of a material. The assumptions that the Langmuir model uses is that there are a fixed number of identical sites that can undergo adsorption. Each of these sites can adsorb only a single molecule, and due to this, a single monolayer is formed on the surface.[27,28] The Langmuir adsorption model can be expressed by Equation 1.

$$Q_e = \frac{Q_m K_L C_e}{1 + K_L C_e}$$

Equation 1: Langmuir adsorption isotherm equation.[27]

Where, Q_e is the amount adsorbed at equilibrium (mg/g), Q_m is the maximum adsorption capacity (mg/g), C_e is the equilibrium concentration (mg/L), and K_L is the Langmuir constant (L/mg). This equation can be linearized (Equation 2) to allow for plotting of C_e/Q_e vs. C_e to provide both the maximum adsorption capacity (Q_m) and the Langmuir constant (K_L). The resulting maximum capacities achieved by using the Langmuir model are summarized in the Tables 5-7 below.

$$\frac{C_e}{Q_e} = \frac{1}{Q_m} C_e + \frac{1}{K_L Q_m}$$

Equation 2: Linearized Langmuir adsorption model equation.[29]

The Freundlich adsorption isotherm describes adsorption onto a heterogeneous surface. This model deviates from the Langmuir model's monolayer adsorption parameter and instead describes multilayer adsorption onto the surface.[29,30] The non-linear expression can be seen below in Equation 3.

$$q_e = K_F C_e^{1/n}$$

Equation 3: Non-linear equation for Freundlich adsorption model.[30]

Where, q_e is the amount adsorbed at equilibrium time (mg/g), C_e is the equilibrium concentration (mg/L), K_F is the capacity of the adsorbent, and n is the Freundlich intensity constant. This equation can be linearized (Equation 4) to allow for plotting of log q_e vs log C_e to solve for K_F. If the concentration of the solution is kept constant and the variation is in the amount of adsorbent then the maximum uptake capacity (q_m) can be calculated (Equation 5).[31] The maximum uptake capacities and the range of the R^2 values are summarized in Tables 5-7 below. The missing values within the tables did not correlate well with the isotherms. These samples gave R^2 values of less than 0.5.

$$log(Q_e) = \log(K_F) + \frac{1}{n_F}\log(C_e)$$

Equation 4: Linearized equation for the Freundlich adsorption model.[29]

$$K_F = \frac{q_m}{C_e^{1/n}}$$

Equation 5: Freundlich maximum adsorption capacity.[31]

Table 5: Monobasic arsenate ($H_2AsO_4^-$) treatment capacities from Langmuir and Freundlich adsorption isotherms.

Isotherm	Fe_2O_3	$Fe_{0.65}Zn_{0.35}O_{1.33}$	$Fe_{0.43}Zn_{0.57}O_{1.22}$	$Fe_{0.29}Zn_{0.57}O_{1.15}$
Langmuir				
q_m (mg/g)	22.9 ± 1.7	65.8 ± 5.6	-	58.0 ± 6.5
R^2	0.98 – 0.99	0.87 – 0.99		0.89 – 0.95
Freundlich				
q_m (mg/g)	22.4 ± 1.2	-	95.4 ± 7.0	74.3 ± 9.2
R^2	0.96 – 0.99		0.87 - 0.99	0.98 – 0.99

Table 6: Dibasic arsenate ($HAsO_4^{2-}$) treatment capacities from Langmuir and Freundlich adsorption isotherms.

Isotherm	Fe_2O_3	$Fe_{0.65}Zn_{0.35}O_{1.33}$	$Fe_{0.43}Zn_{0.57}O_{1.22}$	$Fe_{0.29}Zn_{0.57}O_{1.15}$
Langmuir				
q_m (mg/g)	36.3 ± 3.1	-	28.9 ± 5.1	18.0 ± 6.2
R^2	≥ 0.99		≥ 0.99	0.80 – 0.97
Freundlich				
q_m (mg/g)	27.5 ± 0.6	24.4 ± 2.6	23.1 ± 2.0	-
R^2	0.97 - 0.99	0.91 - 0.97	0.92 - 0.99	

Table 7: Arsenite treatment (H_3AsO_3) capacities from Langmuir and Freundlich adsorption isotherms.

Isotherm	Fe_2O_3	$Fe_{0.65}Zn_{0.35}O_{1.33}$	$Fe_{0.43}Zn_{0.57}O_{1.22}$	$Fe_{0.29}Zn_{0.57}O_{1.15}$
Langmuir				
q_m (mg/g)	51.1 ± 0.4	29.6 ± 0.8	66.0 ± 2.3	50.8 ± 5.5
R^2	≥ 0.99	≥ 0.99	0.93 – 0.96	≥ 0.99
Freundlich				
q_m (mg/g)	57.0 ± 1.3	-	68.4 ± 2.8	55.2 ± 8.6
R^2	0.95 – 0.99		0.95 – 0.96	≥ 0.99

When inspecting the data from the monobasic arsenate treatments, the Freundlich model overall fits best for the materials, with the exception of $Fe_{0.65}Zn_{0.35}O_{1.33}$. This suggests that there is potentially more than a monolayer forming on the surface of the materials or that the surface has more than one type of sorption site. In the case of the bimetallic sorbents, the latter is a safe assumption. There is heterogeneity of the surface sites due to iron and zinc both being present at the surface. There is a significant increase in capacity of the materials as they move from the iron only species to the iron/zinc mixed species. Zinc provides softer sorption sites, as described by the Pearson hard-soft acid base theory, which would be more attractive to the softer arsenate species. For all of the arsenic species, the maximum adsorption capacity was observed for $Fe_{0.43}Zn_{0.57}O_{1.22}$ indicating that there is a maximum in the amount of incorporated zinc to yield a material with the highest capacity. There were major differences observed in the relative behavior of the various sorbents in the 50 mg treatments as compared to the results from the sorption isotherms. This suggests that at higher relative concentrations of arsenic to sorbent molar ratios, additional sites on the sorbents are occupied by arsenic species. This conclusion is in keeping with the better fit of the Freundlich model to the isotherm.

When analyzing the dibasic arsenate treatments a significant decrease in the capacity was observed for all four materials in comparison to the monobasic arsenate capacities. This decrease in capacity is speculated to be due to the solution's pH. In the monobasic arsenate solutions, the starting pH is acidic (4.5) leading to the surface of the adsorbent to be protonated, but with the dibasic arsenate solutions the starting solutions are basic (8.1). This basic environment leads to a surface covered in hydroxyls that are negatively charged. The presence of hydroxyls on the surface leads to repulsion of the negative anions, which reduces the adsorption process and lowers the material's capacity.[32] When modeling the adsorption, the Langmuir model best described all but one of the materials ($Fe_{0.65}Zn_{0.35}O_{1.33}$). This model provides insight that there is a monolayer of adsorption and that the sites are homogenous. This deviation from what is seen in the monobasic arsenate modeling is hypothesized to be from the drastic change in pH. The pH for the treatments are all around the zero point charge for these materials. In previously published work, the zero point charge for iron oxide can be found in the range of around 8.5 and around 9.0 for zinc oxide.[33,34] The zero point charge of a material is the point at which the surface of the material goes from an overall positive charge to an overall negative charge.[34] This change in overall charge of the surface as the pH increases can lead to a homogeneity of the sites and in return, a more compatible fit to the Langmuir adsorption model. It is possible that surface protonation masks one type of site (perhaps iron) more than the other(s).

In modeling the arsenite treatments, the Langmuir model provided the best fit for all four materials. The capacities calculated from the Langmuir model were all within the same capacity range, with the addition of the zinc not causing a decrease in capacity seen

within the iron oxide. Arsenite is known to be difficult to adsorb onto metal oxides due to it being a neutral species in pH below 9.2.[35] The neutrality of the arsenite species means there is no electrostatic attraction to the metal oxide surface resulting in lower capacities.

Arsenic uptake from wastewaters and natural waters

The metal oxides that were used to treat stock arsenic solutions were also used to treat two arsenic containing wastewater samples and one natural water sample that was reported to have an arsenic concentration above the EPA action limit (10 ppb). The two wastewater samples were from different industrial waste streams and the natural water sample was from an underground well source. The advantage of having these samples to treat is to allow for real life samples with a variety of compositional matrices to test against the samples. These samples were treated as received. The initial concentrations and pH are summarized in Table 8.

Table 8: Initial concentrations and pH of wastewater and natural water samples.

	Initial As Concentration (ppm)	Initial pH
Industrial 1	33.00	8.0
Industrial 2	1.5	5.0
Natural 1	0.014	7.6

The sorbents were added to the contaminated waters in varying amounts with the goal to take the solution concentrations below detection limit of the MP-AES (2.5 ppb). 20 mL samples of the selected waters were treated using various amounts of sorbent. The samples were treated at room temperature without adjustment of the pH and continuously

mixed by a motorized rotor. These treatments were carried out over 3 days, giving sufficient time for equilibrium to be reached. Samples were then filtered using 25 mm syringe filters with a 0.2 μm membrane and the filtrate was diluted for analysis by MP-AES. The treatments were performed in the same manner described earlier in the treatments of the arsenic stock solutions. All of the treatments for all of the water samples were able to achieve an arsenic concentration below the detection limit of the MP-AES.

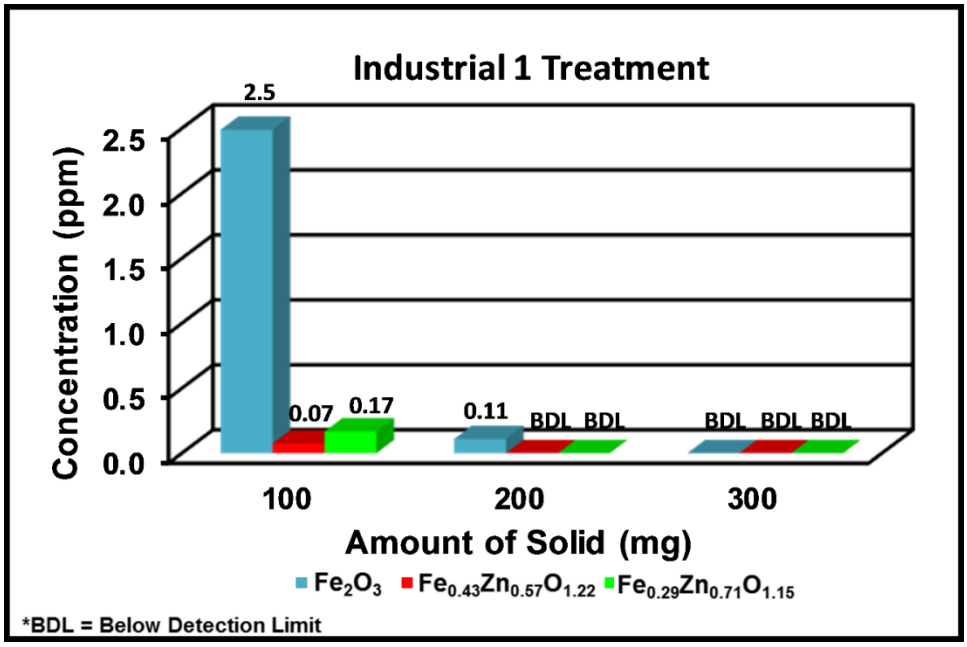

Figure 17: Change in arsenic concentration from industrial produced water using various amounts of material.

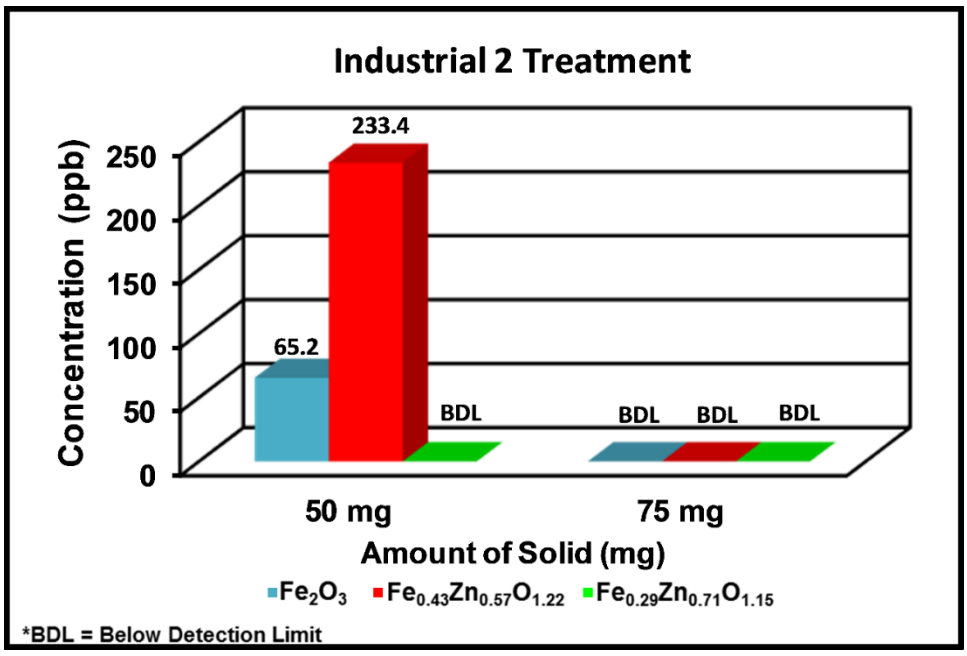

Figure 18: Change of arsenic concentration from an industrially produced water using various amounts of material.

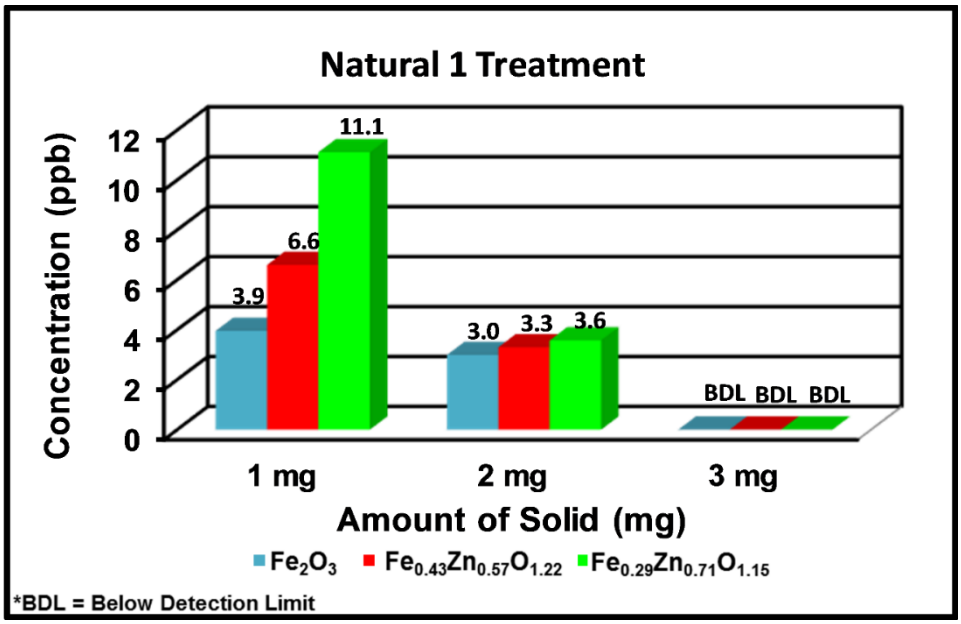

Figure 19: Change of arsenic concentration from natural occurring water using various amounts of material.

In the case of the pH 8.0 Industrial 1 wastewater, the $Fe_{0.43}Zn_{0.57}O_{1.15}$ sorbent performed the best, reducing the arsenic concentration to 0.07 ppm with a 100 mg treatment. This is in accord with the sorption capacity measurements. Notably, both the zinc containing sorbents performed better than the Fe_2O_3. However, for the other wastewater (Industrial 2) that was acidic, the $Fe_{0.29}Zn_{0.71}O_{1.15}$ sample performed far better than the other sorbents. $Fe_{0.43}Zn_{0.57}O_{1.22}$ performed extremely poorly in this case, in comparison to the other two sorbents. If one considers the relative performance of the two zinc-containing sorbents, the results from the Industrial 2 wastewater treatment are in accord with the previously described experiments with $H_2AsO_4^-$. For the groundwater sample, Fe_2O_3 performed the best while $Fe_{0.29}Zn_{0.71}O_{1.15}$ was the poorest performer. This solution is slightly basic and cannot be easily compared to the previously described experiments. Nevertheless, it can be concluded that for all of the test waters, all of the sorbents were able to successfully remove the arsenic concentration below 2.5 ppb with the use of a small amount of sorbent for the treatment. The marked differences between the results for each water delineates the importance of both pH and competing ions in determining both the success of a treatment and how effective one sorbent is with respect with another. More importantly, the results show that varying the ratio of iron to zinc provides the means to tailor a sorbent for a particular application.

Removal of arsenic from apple juice

Consumer Reports reported in 2011 that they had tested almost 90 different brands of apple juice and that 10% of these juices contained arsenic concentrations that exceeded the federal standards for arsenic within water (10 ppb). Within the Consumer Reports study, they found arsenic concentrations as high as 14 ppb in some brands of

apple juice.[36] At the time, the Food and Drug Agency (FDA) currently had a level of concern limit for juice set to 23 ppb but Consumer Reports urged the FDA to adopt a similar standards set by the EPA for drinking water (10 ppb). In July of 2013, the FDA set a new action limit for arsenic in juice matching the 10 ppb action limit of the EPA.[37] Investigation into arsenic contamination from juice sold at local grocers in the Stillwater, Oklahoma area provided us with several samples that when tested all had arsenic concentrations below the newly set 10 ppb action limit. The highest sample tested was determined to contain a concentration of 9 ppb of arsenic.

Treatments of the apple juice were performed using 10 mg of the various metal oxide materials to treat 20 mL of apple juice. The samples were mixed on a vertical rotator for 24 h and then filtered using a 25 mm syringe filter with 0.2 μm nylon membrane. Samples were then digested using a benchtop digestion method of concentrated nitric acid and 30% hydrogen peroxide at 80 °C. This is necessary to remove the complex matrix of the juice. The treated samples were then analyzed by MP-AES. After the 1 day treatments, all the samples were below the detection limit of the MP-AES.

Conclusion

The synthesis of mixed metal oxides was done by a simple decomposition of the corresponding pyruvic acid oxime precursors. This simple precipitation reaction is done using soluble metal salts and sodium pyruvic acid oxime. These precursors' decompositions were investigated by thermal gravimetric analysis and they demonstrated relatively low decomposition temperatures while producing only the metal oxide and

small volatile organic fragments. These metal oxides were then used in treatments of arsenic containing waters. The goal was to use these insoluble metal oxides for the uptake of both arsenate and arsenite species. This feat is often difficult for a single material to accomplish due to varying charge and pH environments that the arsenic species are found in. The mixing of the iron and zinc metal species was hypothesized to allow for a softer character to the material making it more attractive to the arsenate species, while also allowing to keeping the natural arsenite uptake ability found in iron oxide. Batch treatments were then modeled using both Langmuir and Freundlich adsorption isotherms to provide some insight into the possible mechanism of the adsorption process and to allow for the calculation of a maximum uptake capacity. Monobasic arsenate, found predominately in acidic environments, provided the highest uptake for the mixed iron/zinc species with the 1:1 metal ratio performing the best. A significant reduction in uptake capacity is seen when analyzing for uptake of dibasic arsenate. This species being found in basic environments, has natural electrostatic repulsion to the surface of the material and in return lowers the overall uptake capacity. Finally, analysis of the arsenite uptake was performed. This arsenic species is found around neutral pH and unlike both the monobasic and dibasic arsenates, it is a neutral species. These materials were all able to show good adsorption to arsenite.

In addition to the work done in arsenic uptake from stock solutions, the investigation into three “real world” samples were also conducted. These three samples came from different sources with two being industrial waste streams and one coming from a known well source with an elevated arsenic concentration. These samples provided insight into how the materials would function in a more realistic distribution of

arsenic, as well as, competing ions and varying pH ranges. These experiments were performed using the same methodology that was used in the treatment of the stock solutions. Treatment loadings were increased until solutions had an arsenic concentration below the detection limit of the instrumentation. The materials showed an ability to uptake arsenic in real life conditions. Purification of apple juice was also investigated as several reporting agencies documented elevated arsenic levels in this juice. Several brands of apple juice purchased locally showed low levels of arsenic, with the highest having 9 ppb. 10 mg of the metal oxides were used to treat 20 mL of the apple juice overnight to attempt to remove the arsenic from the juice. After 1 day the juice was then filtered, digested and analyzed showing the reduction of the arsenic concentration from 9 ppb to below detection limit.

References

1. Apblett, A. W.; Georgieva, G. D.; Mague, J. T., Incorporation of Radionuclides into Mineral Phases via a Thermally Unstable Complexant Ligand. *MRS Proceedings* 1992**,** *294*.

2. Bagabas, A. A. Low temperature precursors for metal oxide catalysts. Ph.D. Dissertation, Oklahoma State University, Stillwater, OK, USA, 2005.

3. Georgieva, G. D. Metal carboxylate precursors for ceramic materials and waste forms for radionuclides. Ph.D. Dissertation, Tulane University, New Orleans, LA, USA, 1995.

4. Ravindranathan, P.; Patil, K. C., Novel solid solution precursor method for the preparation of ultrafine Ni-Zn ferrites. *Journal of Materials Science* 1987**,** *22* (9), 3261-3264.

5. Vidyasagar, K.; Gopalakrishnan, J.; Rao, C. N. R., A convenient route for the synthesis of complex metal oxides employing solid-solution precursors. *Inorganic Chemistry* 1984**,** *23* (9), 1206-1210.

6. Apblett, A. W.; Georgieva, G. D.; Mague, J. T., Synthesis and Spectroscopic and Thermal Decomposition Studies of Alkali Metal Salts of 2-Oximidopropionate. *Inorganic Chemistry* 1997**,** *36* (12), 2656-2661.

7. Rukundo, E. Metal 2-oximinocarboxylate precursors for low-temperature synthesis of oxide nanomaterials. Ph.D. Dissertation, Oklahoma State University, Stillwater, OK, USA, 2015.

8. Bagabas, A. A. A., Allen W.; Shemsi, Ahsan M.; Seddigi, Zaki S., Synthesis, X-ray crystal structure, spectroscopic characterization, and thermal chemistry of trans-diaqua-bis-(2-hydroxyiminopropionato-N,O) zinc(II), trans-{$(H_2O)_2[H_3CC(=NOH)COO)]_2Zn$} – A precursor for nano-crystalline zincite. *Main Group Chemistry* 2008**,** *7*, 65-81.

9. Hughes, M. F.; Beck, B. D.; Chen, Y.; Lewis, A. S.; Thomas, D. J., Arsenic Exposure and Toxicology: A Historical Perspective. *Toxicological Sciences* 2011, *123* (2), 305-332.

10. Issa, N. B.; Rajaković-Ognjanović, V. N.; Jovanović, B. M.; Rajaković, L. V., Determination of inorganic arsenic species in natural waters—Benefits of separation and preconcentration on ion exchange and hybrid resins. *Analytica Chimica Acta* 2010, *673* (2), 185-193.

11. Cheng, H.; Hu, Y.; Luo, J.; Xu, B.; Zhao, J., Geochemical processes controlling fate and transport of arsenic in acid mine drainage (AMD) and natural systems. *Journal of Hazardous Materials* 2009, *165* (1–3), 13-26.

12. Organization, W. H. Arsenic. who.int/mediacentre/factsheets/fs372/en/.

13. Registry, A. f. T. S. a. D. Arsenic Toxicity : What are the physiologic effects of arenic exposure?

14. Organization, W. H., *Guidelines for Drinking-water Quality*. IWA Publishing: 2004.

15. Agency, E. P. Drinking Water Arsenic History Rule. epa.gov/dwreginfo/drinking-water-arsenic-rule-history.

16. Ali, I., New Generation Adsorbents for Water Treatment. *Chemical Reviews* 2012, *112* (10), 5073-5091.

17. Xu, P.; Zeng, G. M.; Huang, D. L.; Feng, C. L.; Hu, S.; Zhao, M. H.; Lai, C.; Wei, Z.; Huang, C.; Xie, G. X.; Liu, Z. F., Use of iron oxide nanomaterials in wastewater treatment: A review. *Science of The Total Environment* 2012, *424*, 1-10.

18. Hua, M.; Zhang, S.; Pan, B.; Zhang, W.; Lv, L.; Zhang, Q., Heavy metal removal from water/wastewater by nanosized metal oxides: A review. *Journal of Hazardous Materials* 2012, *211–212*, 317-331.

19. Aredes, S.; Klein, B.; Pawlik, M., The removal of arsenic from water using natural iron oxide minerals. *Journal of Cleaner Production* 2012, *29–30*, 208-213.

20. Chappell, W. R., *Arsenic Exposure and Health Effects V*. Elsevier: 2003.

21. Pearson, R. G., Hard and Soft Acids and Bases. *Journal of the American Chemical Society* 1963, *85* (22), 3533-3539.

22. Mohan, D.; Pittman, C. U., Arsenic removal from water/wastewater using adsorbents—A critical review. *Journal of Hazardous Materials* 2007, *142* (1), 1-53.

23. Palacios, E. G.; Juárez-López, G.; Monhemius, A. J., Infrared spectroscopy of metal carboxylates. *Hydrometallurgy* 2004, *72* (1), 139-148.

24. Mehrotra, R. C., *Metal carboxylates*. London New York : Academic Press: London, New York, 1983.

25. Shraim, A.; Chiswell, B.; Olszowy, H., Speciation of arsenic by hydride generation–atomic absorption spectrometry (HG–AAS) in hydrochloric acid reaction medium. *Talanta* 1999, *50* (5), 1109-1127.

26. Carrero, P.; Malavé, A.; Burguera, J. L.; Burguera, M.; Rondón, C., Determination of various arsenic species by flow injection hydride generation atomic absorption spectrometry: investigation of the effects of the acid concentration of different reaction media on the generation of arsines. *Analytica Chimica Acta* 2001, *438* (1), 195-204.

27. Langmuir, I., The Adsorption of Gases on Plane Surfaces of Glass, Mica and Platinum. *Journal of the American Chemical Society* 1918, *40* (9), 1361-1403.

28. Yagub, M. T.; Sen, T. K.; Afroze, S.; Ang, H. M., Dye and its removal from aqueous solution by adsorption: A review. *Advances in Colloid and Interface Science* 2014, *209* (Supplement C), 172-184.

29. Foo, K. Y.; Hameed, B. H., Insights into the modeling of adsorption isotherm systems. *Chemical Engineering Journal* 2010, *156* (1), 2-10.

30. Freundlich, H. M. F., Over the Adsorption in Solution. *J. Phys. Chem.* 1906, *57*, 385-470.

31. Halsey, G. D., The Role of Surface Heterogeneity in Adsorption. In *Advances in Catalysis*, Frankenburg, W. G.; Komarewsky, V. I.; Rideal, E. K., Eds. Academic Press: 1952; Vol. 4, pp 259-269.

32. Hsia, T. H.; Lo, S. L.; Lin, C. F., As(V) adsorption on amorphous iron oxide: Triple layer modelling. *Chemosphere* 1992, *25* (12), 1825-1837.

33. Siddiqui, S. I.; Chaudhry, S. A., Iron oxide and its modified forms as an adsorbent for arsenic removal: A comprehensive recent advancement. *Process Safety and Environmental Protection* 2017, *111* (Supplement C), 592-626.

34. Akyol, A.; Yatmaz, H. C.; Bayramoglu, M., Photocatalytic decolorization of Remazol Red RR in aqueous ZnO suspensions. *Applied Catalysis B: Environmental* 2004, *54* (1), 19-24.

35. Hlavay, J.; Polyák, K., Determination of surface properties of iron hydroxide-coated alumina adsorbent prepared for removal of arsenic from drinking water. *Journal of Colloid and Interface Science* 2005, *284* (1), 71-77.

36. *Arsenic in your juice.*; 2012.

37. Dennis, B., FDA to set new limit on arsenic in apple juice. *The Washington Post* 2013.

CHAPTER IV

Synthesis of Cobalt-Doped Zinc Oxide for the Use in Photovoltaic Applications.

Introduction

This chapter addresses the development of cobalt-doped zinc oxide that has potential applications in several areas including photovoltaics and pigments. Interest in semiconductor materials has expanded to a wide variety of applications such as photovoltaics, photocatalysis, and gas sensing that take advantage of a semiconductor's unique properties. A key distinguishing property becomes apparent when comparing the conduction character for the three classes of electronic materials, namely insulators, semiconductors, and metals. According to Hoffman's band theory (Figure 1), a metal has its bonding band (valence band) and anti-bonding band (conduction band) overlapping allowing electrons to easily flow from band to band.[1,2] A hallmark of a metallic conductivity is a the temperature of the metal increases.[2] In an insulator, the valence and conduction bands have a large gap (band gap) between the valence and conduction bands preventing the flow of electrons.

With a semiconductor, there is a band gap between the valence and the conduction bands but it is small enough that the electrons can be excited and jump from the valence band into the conduction band allowing for a flow of electrons.[2] The defining property of a semiconductor is that its conduction increases as the temperature increases.[2]

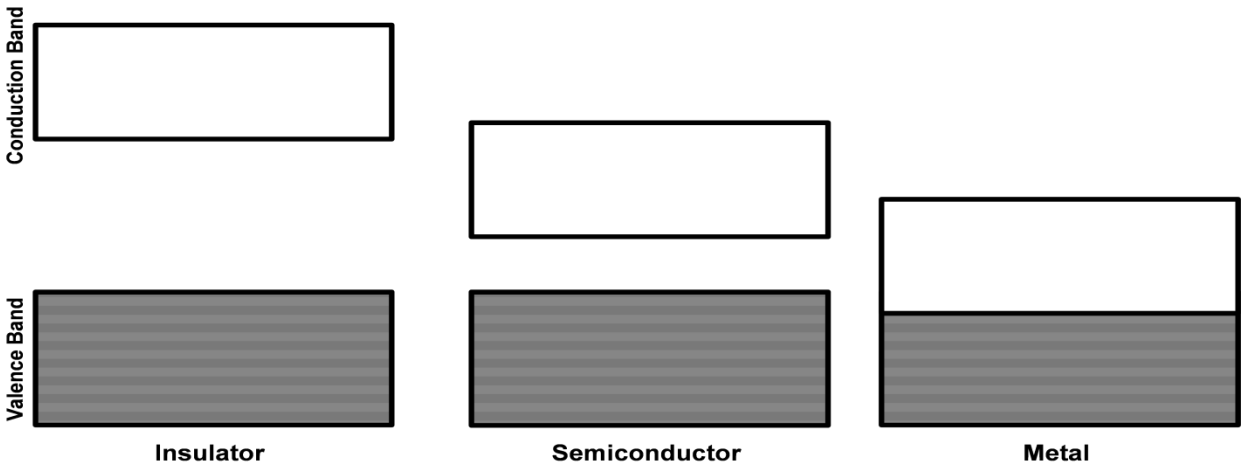

Figure 1: Energy Band separation within an insulator, semiconductor, and metal.

Semiconductors are described as either intrinsic or extrinsic type. Intrinsic semiconductors are pure materials, such as silicon, that exhibit semiconductor behavior naturally. Extrinsic type semiconductors are materials that have a defect or a dopant that provide the material with an excess of electrons or vacancies that allows for conductivity (Figure 2).[2,3] Doping is a term used when a small amount of impurities are added to the crystal lattice. The dopant can have either more or less electrons than the atoms within the crystalline lattice, which in return provides either an excess of electrons or an excess of vacancies. If the dopant has an excess of electrons then it is considered an n-type dopant and results in an n-type semiconductor. The excess of electrons are found in the band gap and allow for less energy to be needed to promote them into the conduction

band.[2] If the dopant is electron deficient, providing an excess of vacancies, it is considered a p-type dopant and the resulting material is called a p-type semiconductor. These excess vacancies lie within the band gap and provide holes at low energy for the electrons to be promoted, thus increasing conductance.[2]

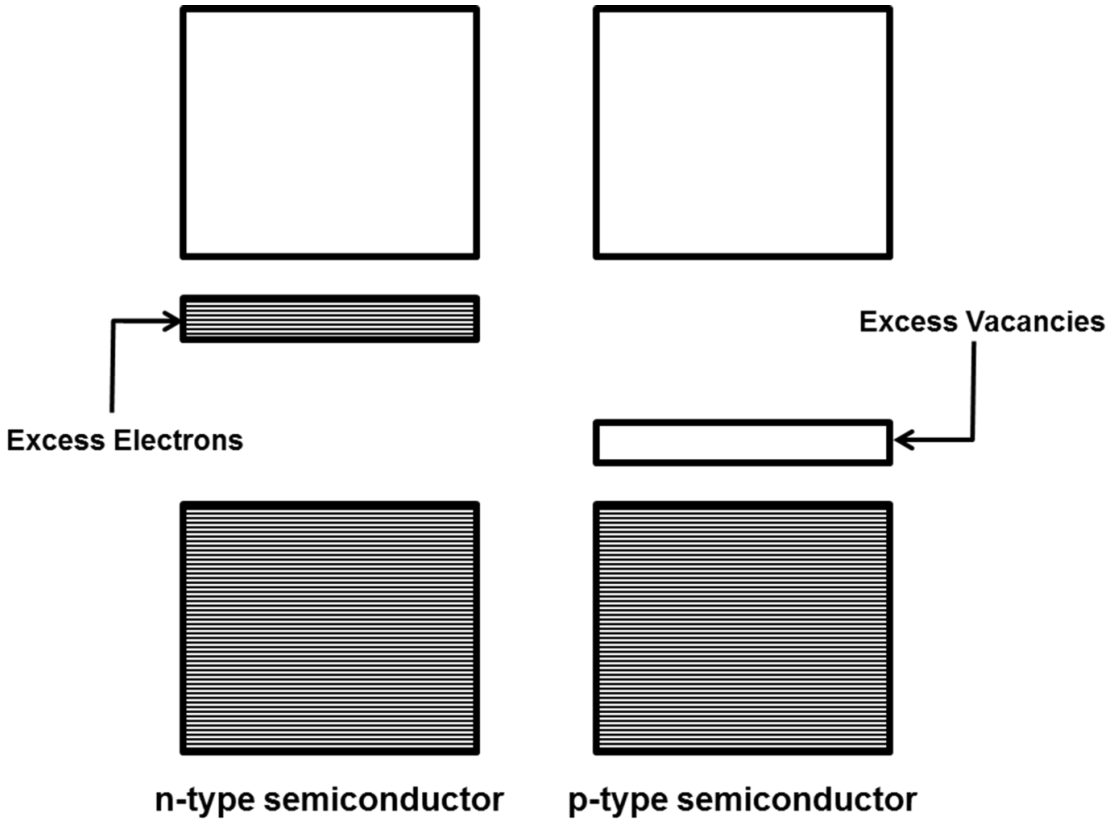

Figure 2: Band diagram for n-type and p-type semiconductors.

Photovoltaics take advantage of the photoelectric effect that allows them to absorb light and convert that energy into electrical conduction, as the electrons are promoted from the valence band to the conduction band (Figure 3). This production of electricity has inspired researchers to work on adapting these devices to our everyday lives and to start advancing towards these devices replacing the dependence on more finite energy sources. During the 1950's, photovoltaic cells were used in the space

program for power sources and then in the 1970's the technology transitioned into use at the ground level during the oil embargo.[4] First generation photovoltaics were made using single crystal or multi-crystal silicon wafers. These devices were quite expensive with both the materials and the manufacturing leading to this high price, but had high efficiency of 16 to 21%.[5] Second generation photovoltaics reduced cost by adopting thin film technology. Materials such as amorphous silicon and cadmium telluride were suitable for thin film applications but the resulting efficiency suffered and was lowered to 5 to 15%. The current generation of photovoltaics consists of multi-layer cells and quantum dots. These materials aim to take advantage of the complete visible light spectrum to increase the efficiency reaching over 23% while using cheap materials.[5,6]

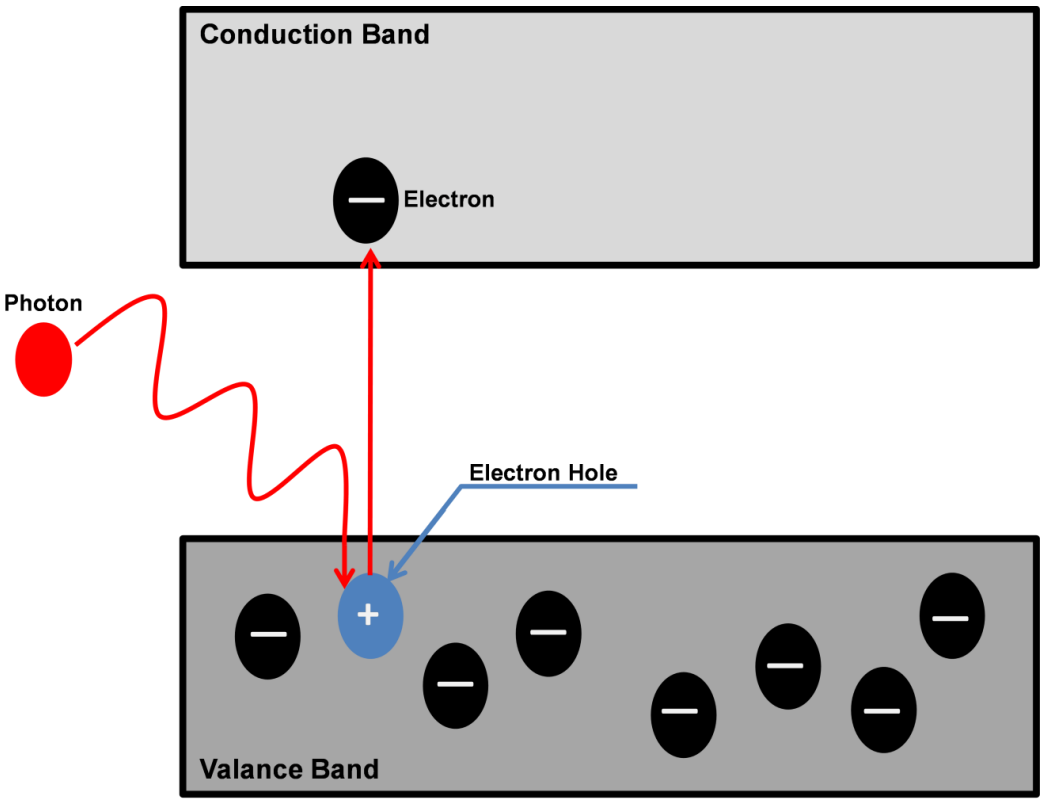

Figure 3: The photoelectric effect.

The semiconductor that will be discussed within this chapter will be zinc oxide. It is commonly found in either wurtzite (hexagonal) or zincblende (cubic) crystalline form. Wurtzite is more common due to it being a more stable structure under ambient conditions.[3] Zinc oxide is considered an n-type wide band gap semiconductor. A semiconductor with a wide band gap is said to have a band gap around 2.2 – 4.0 eV.[7] At room temperature, zinc oxide has a band gap of 3.37 eV.[8] This energy gap corresponds to that of the near ultraviolet region (300-400 nm), so there is a lot of interest in doping ZnO to alter the band gap to allow for absorption into the visible spectrum.[3] The n-type feature of ZnO comes with some debate since there are two main hypotheses. The first hypothesis is that either there are oxygen vacancies within the crystal lattice or extra zinc ions are trapped in the interstitial areas.[8,9] This would lead to an excess of electrons and provide the n-type character. The second hypothesis is that hydrogen impurities are unintentionally introduced into the interstitial areas of the ZnO crystal lattice.[8,10] Zinc oxide also shows other promising features for semiconductor use with attractive features such as high electron mobility, high thermal conductivity, low toxicity, and ready availability.[3,11]

Due to ZnO's band gap corresponding to the near ultraviolet region, there is a significant amount of the solar spectrum unused. Being able to alter this band gap and move the energy required to promote an electron by use of light in the visible spectrum would allow for a more efficient use of natural light. Band gap engineering is a term given to the exploration of the effects of dopants and defects to change the natural band gap of a specific material to a more desired band gap.[12] Band gap engineering in materials for photovoltaics aims to provide a wider or a more specific range of absorption

of light with the desired material to improve the efficiency of the device. The goal for this project was to develop ZnO and cobalt-doped zinc oxide with varying extents of doping. Cobalt doping will allow for the alteration of the band gap of ZnO allowing for the absorption of light to be moved from the near ultraviolet range to the visible region. This synthesis was done using two different approaches; the first was by the low temperature single source precursor method, introduced in Chapter 3, to produce cobalt-doped zinc oxide powder. The second approach involved the use of a low temperature chemical bath deposition to produce films on glass substrates. Exploration of various cobalt-doping percentages was performed using both synthetic methods.

Materials

All chemicals were purchased commercially and used with no further purification. Pyruvic acid (Tokyo Chemical Co.), sodium carbonate (Malinckrodt), hydroxylamine hydrochloride (Alfa Aesar), zinc chloride (Alfa Aesar), and cobalt chloride hexahydrate (Alfa Aesar) were used in the synthetic steps for the single source precursor method. The chemical bath deposition used zinc chloride (Alfa Aesar), zinc nitrate heptahydrate (Alfa Aesar), cobalt chloride hexahydrate (Fischer Scientific), cobalt nitrate hexahydrate (Alfa Aesar), and hexamethylenetetramine (Sigma Aldrich) in the development of the films. Films were grown on 3x1 inch plain microscope slides from Sargent-Welch. These were cleaned prior to use with a 5 M HCl solution, followed by acetone, and finally deionized water. Standards employed for elemental analysis using the MP-AES were purchased from Alfa Aesar. Unless otherwise stated, all reactions took place at room temperature (23 °C) in deionized water (18 MΩ·cm) obtained from a Barnstead E-Pure System.

Experimental

Single Source Precursor Approach

The synthetic method for the synthesis of the NaPAO has been previously described in Chapter 2. The synthesis of the cobalt-doped zinc oxide precursors involves the precipitation of the metal pyruvic acid oxime complex using various concentrations of aqueous zinc and cobalt salts and NaPAO in a 1:2 total molar ratio. The ratios targeted in this study were pure zinc as well as doping with 5% and 10% cobalt. The doping was achieved by controlling the stoichiometry of the initial solution when synthesizing the precursor. For example, for the 5% cobalt sample the molar ratio of cobalt to zinc used was 0.05 to 0.95 moles. In all cases, these precursors were collected by vacuum filtration and washed with 250 mL of deionized H_2O. These materials were then air-dried and stored at room temperature for further investigation.

Chemical Bath Deposition Approach

The method for this approach was adapted from previously published work by Vayssieres and Hari. [13,14] In this method, hexamethylenetetramine (5.62 g, 40 mmol) was dissolved in 20 mL of deionized H_2O. This was reacted with an equimolar solution of metal ions produced by dissolving anhydrous $ZnCl_2$ and $CoCl_2{\cdot}6H_2O$ in 20 mL of H_2O. In the case of these reactions, varying percentages of $CoCl_2{\cdot}6H_2O$ were used to produce the corresponding final material. The two solutions are then stirred for 1 hour. With the addition of the hexamethylenetetramine to the metal salt solution, a precipitation of the metal-hexamethylenetetramine complex occurs.[15,16] After 1 hour, the reaction was vacuum filtered and the filtrate was transferred to a reaction jar. A small hole was drilled

into one of the ends of a pre-cleaned glass slide to allow its suspension into the filtrate by a nylon string. The lid of the jar was then screwed on to tightly seal the chemical bath. The jar was then placed into a 95 °C oven for 6 hours. The hexamethylenetetramine used in this reaction was a source for hydroxyl ions that can react with the Zn^{2+} in solution ultimately producing ZnO (Scheme 1). After 6 hours, the glass slide was removed from the reaction solution and gently rinsed with deionized water and left to air dry for further analysis. These film growth experiments were performed using several different dopant percentages along with several different metal salts including chlorides, nitrates, acetates and sulfates. Uniform film growth was achieved using the nitrate and chloride salts, but the acetate and sulfate solutions produced non-uniform films and were not further explored.

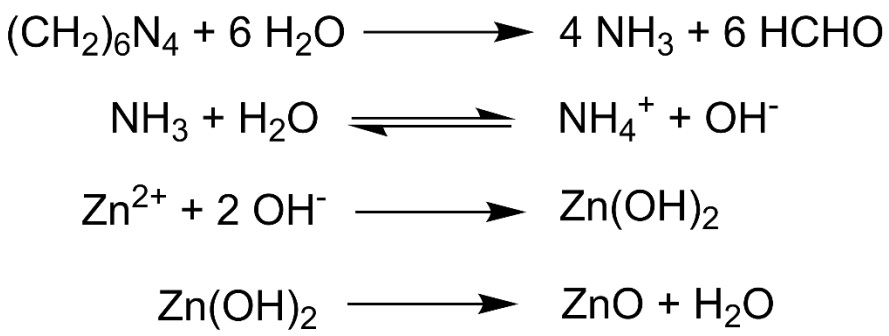

Scheme 1: Reaction mechanism for the growth of ZnO film using hexamethylenetetramine.

Results and Discussion

Characterization

Infrared spectra were collected for the PAO precursors and their decomposition products using a Nicolet iS50 FT-IR spectrometer. Thermal gravimetric analyses were

performed using a Mettler-Toledo TGA/DSC 1. The TGA traces of the PAO precursors were used to determine decomposition temperatures. Elemental analysis was performed using an Agilent 4200 microwave plasma atomic emission spectrometer for the digested solutions of the PAO decomposition products and the films grown on the glass slides. An Orbis micro X-ray fluorescence analyzer was used to analyze the films grown on the glass slides to determine the presence of cobalt within the films. Powder X-ray diffraction was performed on the final products of the PAO precursors and the films grown on the glass slides. This was done to determine crystallinity, crystallite size and identify crystal structure. Identification of crystalline phases was achieved by matching with published structures in the International Centre for Diffraction Data (ICDD) database. A JM magnetic susceptibility balance was used to measure the magnetic susceptibility for the PAO calcined products.

Synthesis of Cobalt-Doped Zinc Precursors

The synthesis of the cobalt-doped zinc pyruvic acid oximes was realized by simple ligand exchange reaction of NaPAO with $CoCl_2$ and $ZnCl_2$ in specific molar ratios (Scheme 2). The target molar ratios were 5% and 10% cobalt.

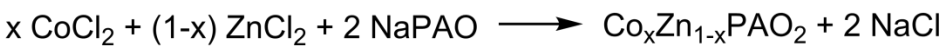

Scheme 2: Synthesis of cobalt zinc pyruvic acid oxime. x = 0.05 or 0.10.

Thermal gravimetric analysis performed over a temperature range of 25 °C to 500 °C with a heating ramp of 5 °C/min. When pyruvic acid oxime complexes decompose, they produce into small organic fragments and leave behind the corresponding metal

oxide. Decomposition of the ligand produces CO_2, CH_3CN, and H_2O. Decomposition of the doped precursors both began around 120 °C and the final metal oxide was produced around 300 °C (Figures 4 & 5). 350 °C was chosen as the temperature used to produce the cobalt doped metal oxide by bulk pyrolysis.

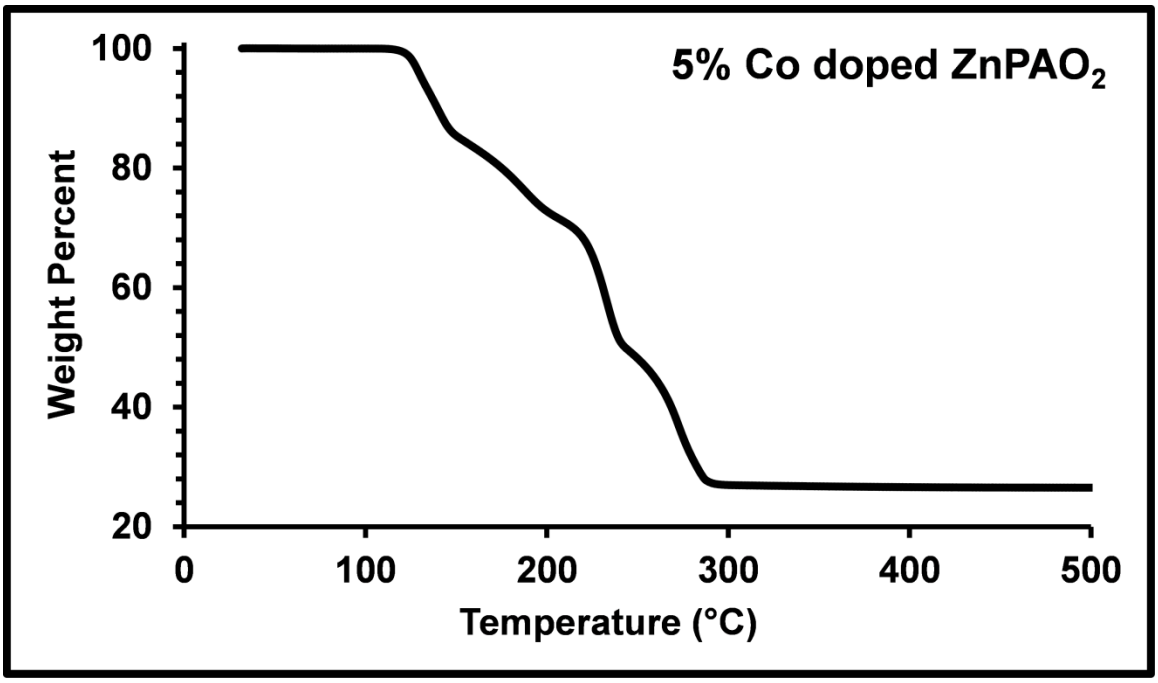

Figure 4: TGA trace for the decomposition of 5% Co doped $ZnPAO_2$ heated in air at 5 °C/min.

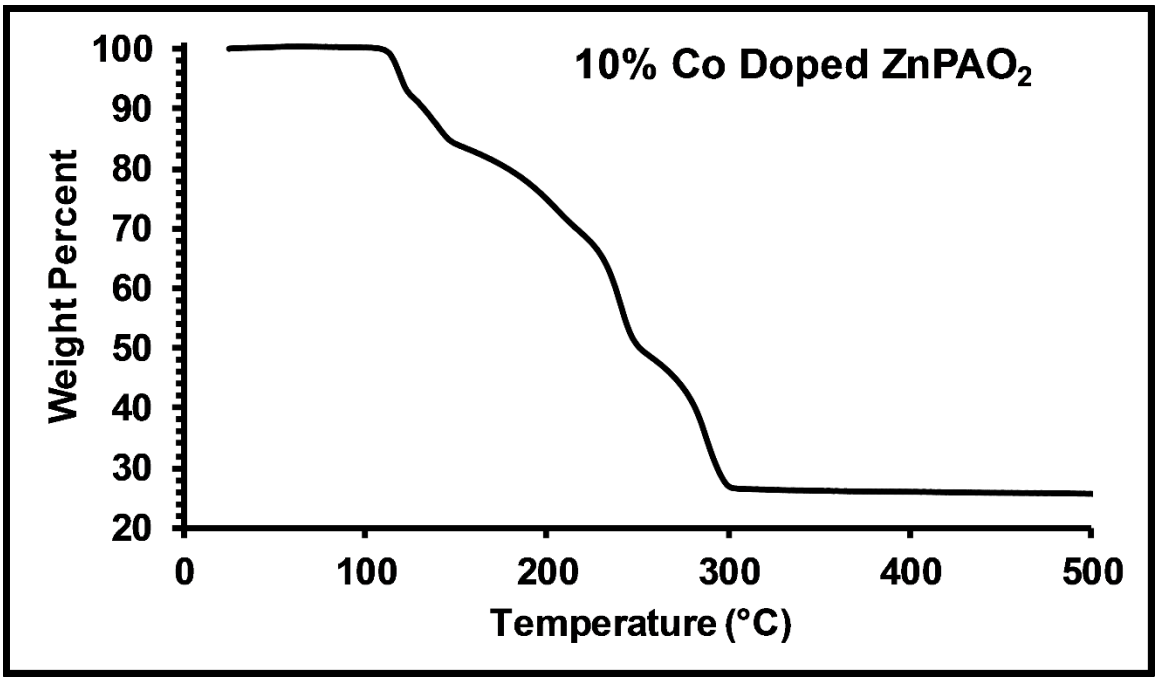

Figure 5: TGA trace for the decomposition of 10% Co doped $ZnPAO_2$ heated in air at 5 °C/min.

A major physical change that occurred through the decomposition of the precursors was a evident change in color. The starting precursor is light pink in color (Figure 6) and after the decomposition; a dark green powder is produced (Figure 7). The hue of the green appears to become darker as the cobalt concentration increases. This drastic color change from the white color of pure ZnO is caused by the alteration of the band gap. This red shift into the visible spectrum is attributed to the addition of cobalt within the tetrahedral holes of the ZnO.[17] Notably, the cobalt-doped oxides appear to be excellent green pigments.

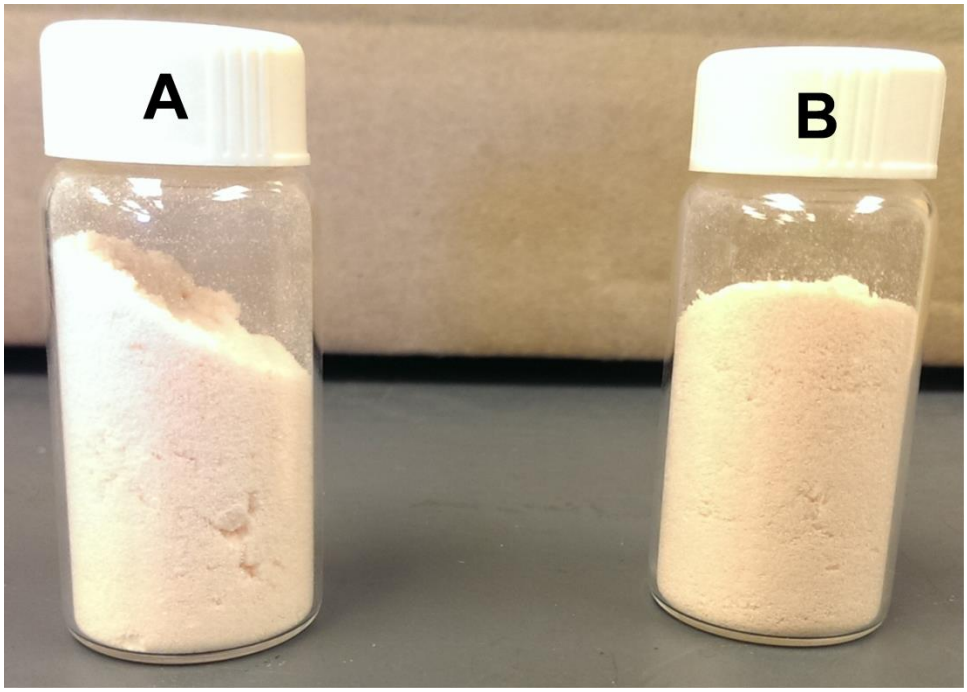

Figure 6: Cobalt-doped zinc pyruvic acid oxime precursors; (A) 5% cobalt, (B) 10% cobalt.

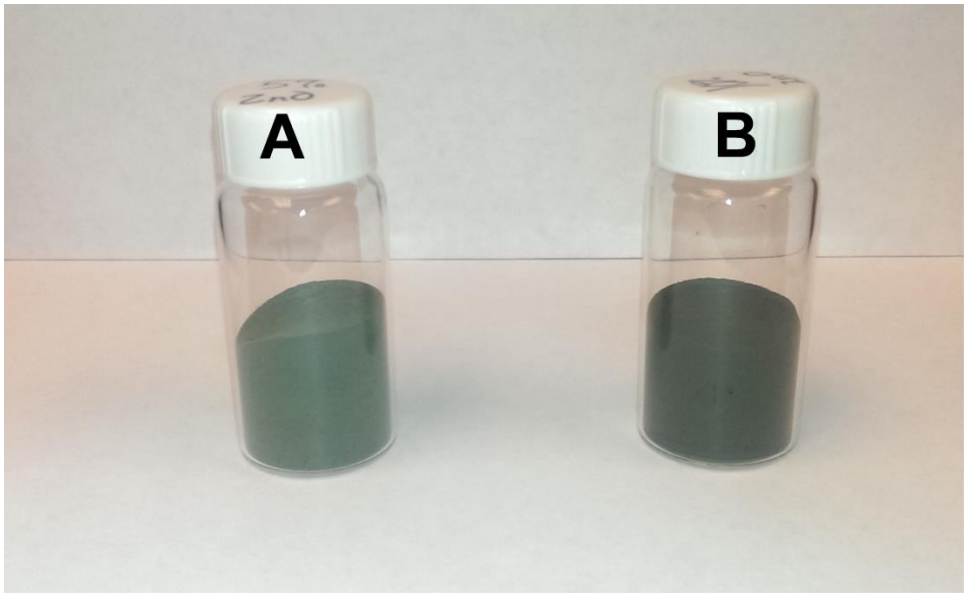

Figure 7: Cobalt-doped zinc oxide after pyrolysis at 350 °C; (A) 5% cobalt, (B) 10% cobalt.

Infrared spectra were recorded for the two starting PAO materials to identify any characteristic peaks for the complexes. The distinctive peaks are shown below in Table 1. Comparing the symmetrical and asymmetrical stretches for the carboxylate group, we can observe a difference in frequencies (Table 2) greater than 250 nm corresponding to monodentate coordination.

Table 1: Characteristic IR frequencies (cm^{-1}) for the PAO complexes.

Compound	$\nu_{(C=N)}$	$\nu_{as\ (COO)}$	$\nu_{s\ (COO)}$	$\nu_{(N—O)}$
5% Co $ZnPAO_2$	1671	1643	1388	1048
10% Co $ZnPAO_2$	1671	1643	1388	1047

Table 2: Change in $\nu_{as\ (COO)}$ and $\nu_{s\ (COO)}$

Material	$\Delta\nu_{(COO)}$*
5% Co $ZnPAO_2$	255 cm^{-1}
10% Co $ZnPAO_2$	255 cm^{-1}

*$\Delta\nu_{(COO)}$ was calculated from $\Delta\nu_{(COO)} = \nu_{as\ (COO)} - \nu_{s\ (COO)}$

X-ray powder diffraction patterns were obtained for the cobalt-doped zinc PAO complexes. The products were determined to be crystalline, but there were no matches in the International Center for Diffraction Database (Figure 8 & 9). Diffraction patterns were also recorded for the doped metal oxides after calcination. These patterns show broadening of the peaks that can be attributed to the nanocrystallinity of the materials (Figure 10 & 11).[18] These powder patterns match that of wurtzite ZnO found within the ICDD database (PDF = 00-036-1451). Increasing the amount of cobalt doping into the

zinc oxide wurtzite structure leads to a distortion of the wurtzite crystal lattice causing the powder pattern to display broadening of the peaks. The crystallite size for the cobalt doped zinc oxide materials were calculated using the Scherrer equation (Equation 1) and are summarized in Table 3.[19] The crystallite size is calculated by using a size factor (K) of 0.9 and the wavelength of the copper radiation source (λ) (1.5405 Å) and dividing that by the full width at half maximum (β) of a specific peak multiplied by the Bragg angle (θ) (Equation 1).

$$\text{Crystallite Size} = \frac{K\lambda}{\beta \text{Cos}\theta}$$

Equation 1: Scherrer Equation.

Table 3: Crystallite Size for Co doped ZnO.

Material	Crystallite Size (nm)
5% Co ZnO	18.5
10% Co ZnO	13.2

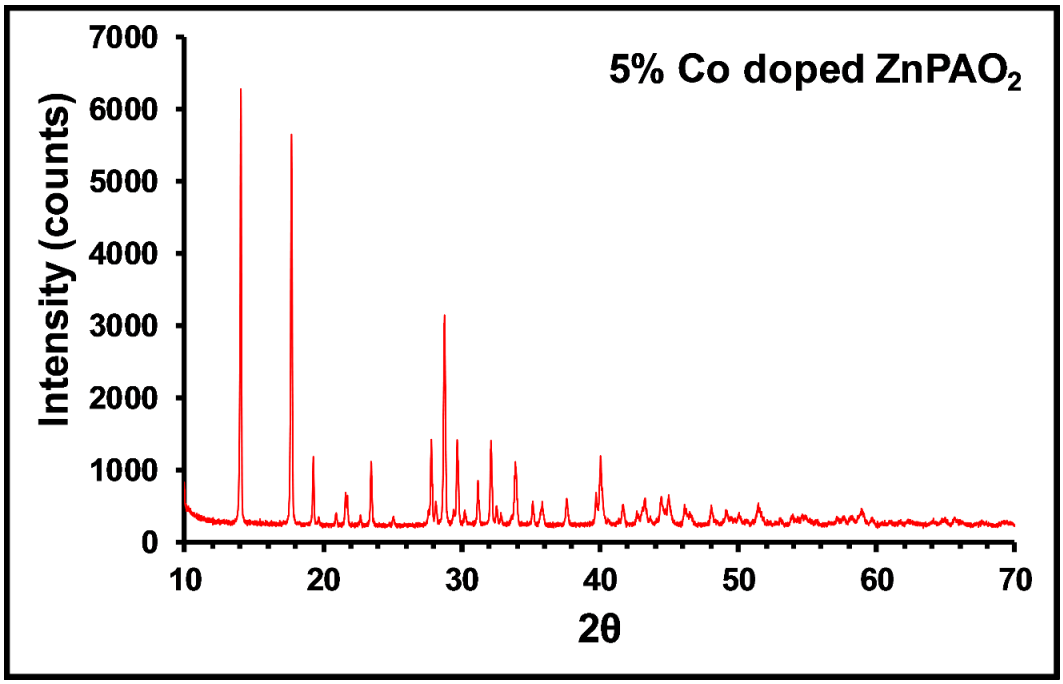

Figure 8: Powder X-ray diffraction pattern of 5% cobalt-doped zinc pyruvic acid oxime complex.

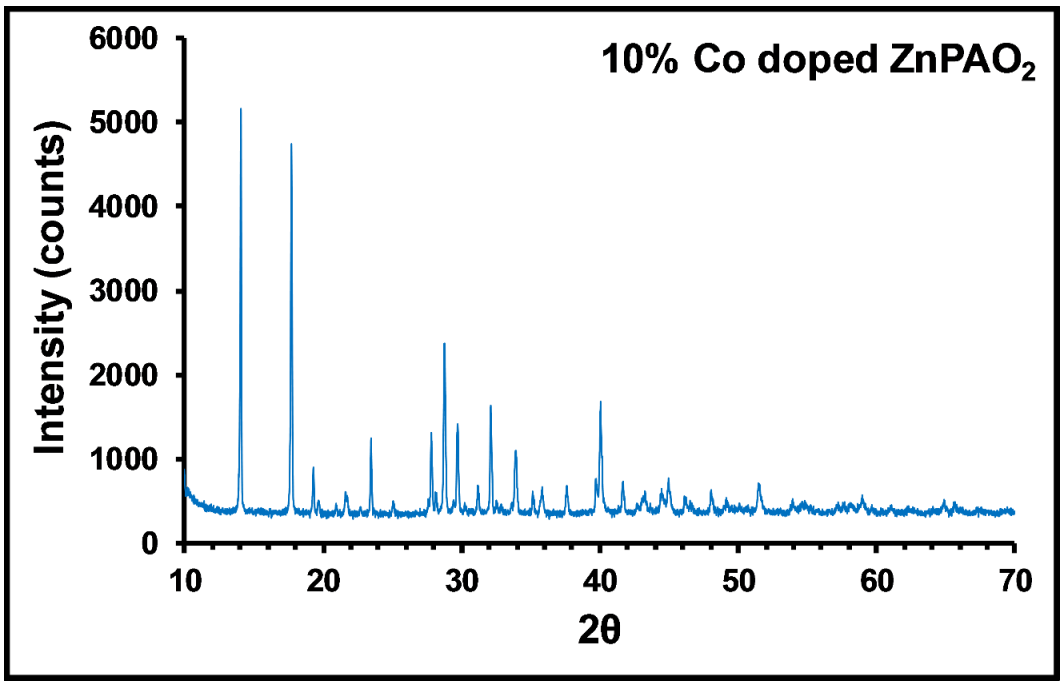

Figure 9: Powder X-ray diffraction pattern of 10% cobalt-doped zinc pyruvic acid oxime complex.

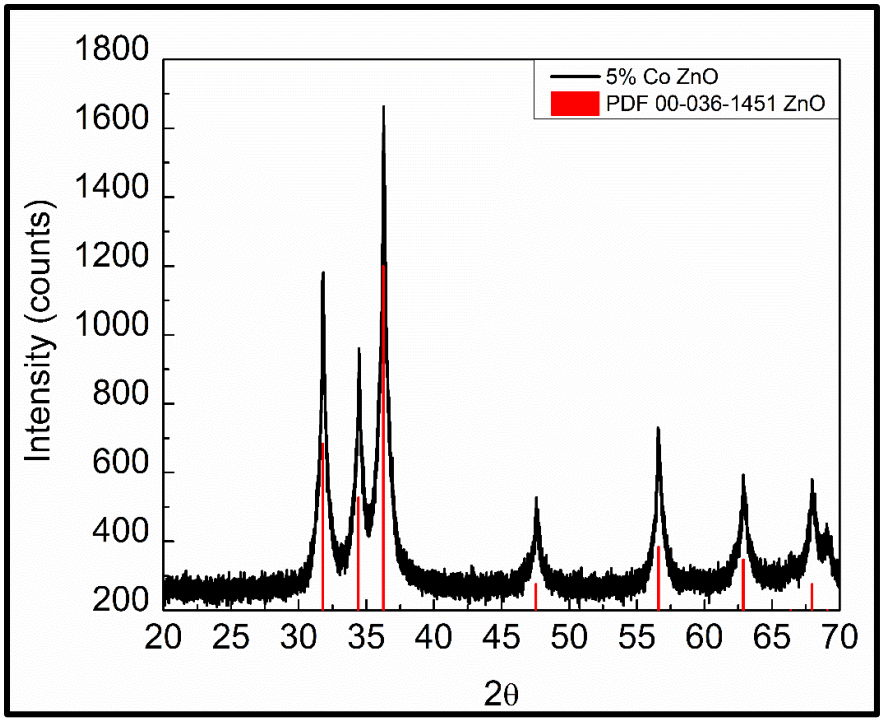

Figure 10: Powder X-ray diffraction pattern of 5% cobalt-doped zinc oxide matched with wurtzite ZnO (PDF=00-036-1451).

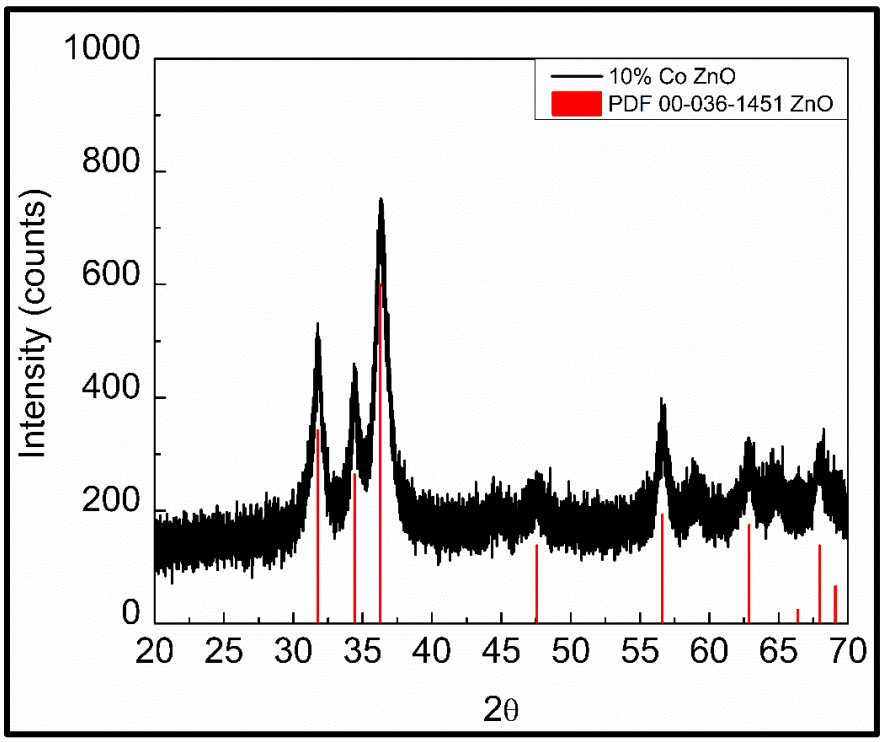

Figure 11: Powder X-ray diffraction pattern of 10% cobalt-doped zinc oxide matched with wurtzite ZnO (PDF=00-036-14510).

The morphology of the complexes before and after the pyrolysis was investigated by scanning electron microscopy. Similar to results for other PAO complexes presented in Chapter 2, ribbon or sea urchin type motifs are present within the micrographs (Figure 12). These shapes are retained after the materials undergo decomposition (Figure 13) with the significant change being severe cratering (Figure 14).

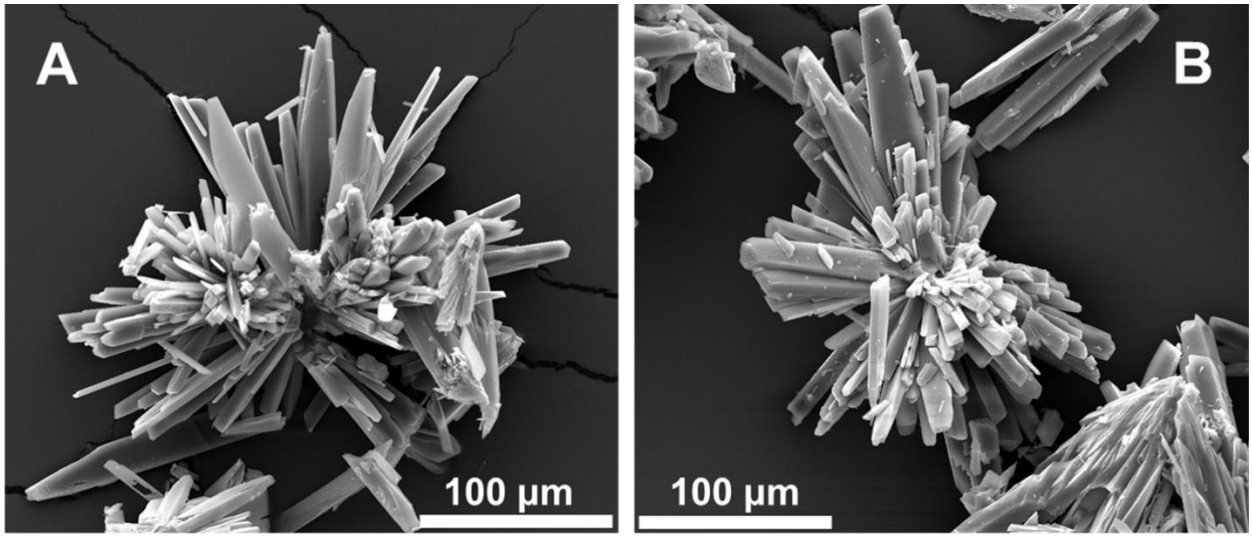

Figure 12: Scanning electron micrographs of Co doped $ZnPAO_2$; (A) 5% Co, (B) 10% Co.

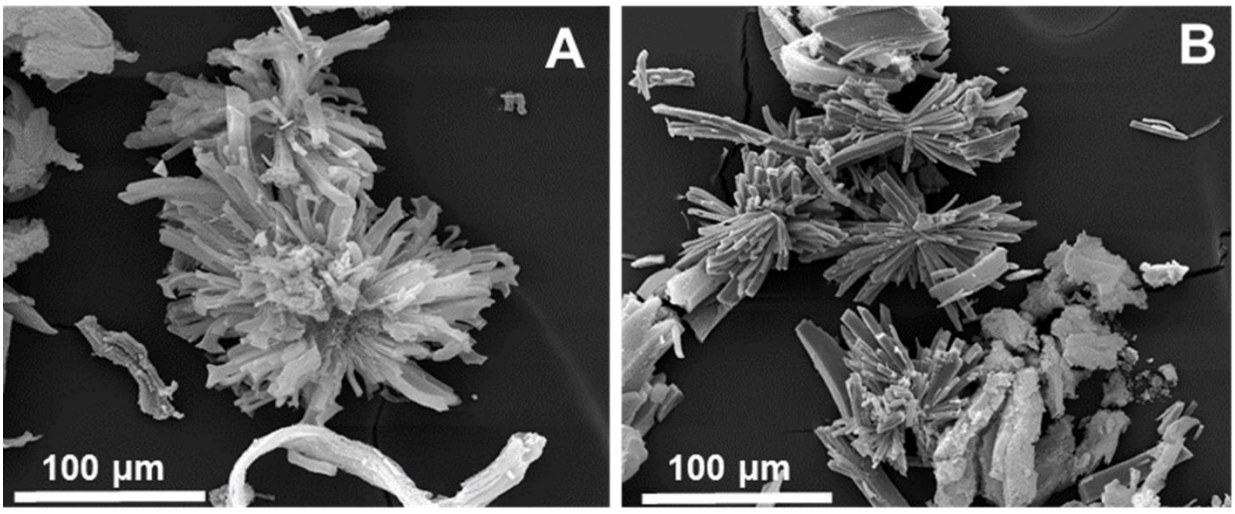

Figure 13: Scanning electron micrographs of Co doped ZnO after decomposition at 350°C; (A) 5% Co, (B) 10% Co.

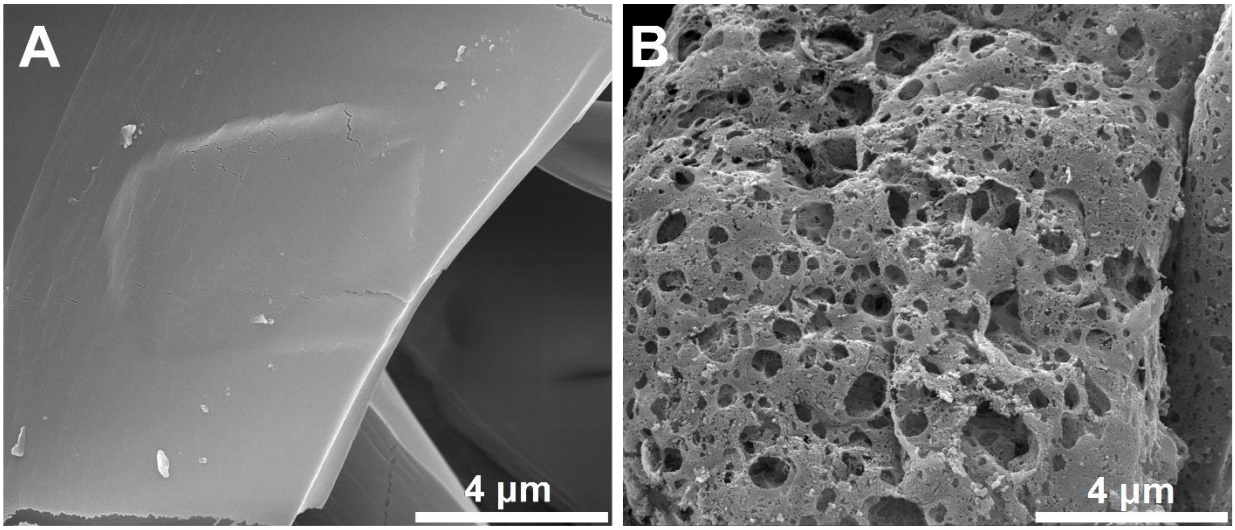

Figure 14: Scanning electron micrograph of 5% Co doped complexes before (A) and after (B) decomposition at 350°C.

Magnetic susceptibility measurements were performed to identify the oxidation state of the cobalt within the final ceramic material. These were measured using a Johnson Matthey Auto magnetic susceptibility balance (Evans balance). This balance uses a stationary sample and movable magnets that are positioned opposite to each other on a balanced beam. Inserting a sample into the balance causes force to be put on the magnets which tips the beam. The balance then provides an electric current to compensate for the off balanced beam. This current is proportional to the sample's magnetic force on the magnets.[20] Using the readings from the Evans balance, mass susceptibility can be solved (Equation 2). In a solid sample, the volume susceptibility of air term is ignored and the equation is replaced with Equation 3.

$$\chi_g = \frac{L}{m}\left[C(R - R_o) + \chi_v' A\right]$$

Equation 2: The general expression for mass magnetic susceptibility.

$$\chi_g = \frac{CL(R - R_o)}{m * 10^9}$$

Equation 3: Mass magnetic susceptibility equation ignoring the volume susceptibility of air.

The mass magnetic susceptibility can be solved by the multiplication of the balance calibration constant (C) with the sample length in cm (L) and the difference of the sample reading (R) and the reading from a empty sample tube (R_o) and then dividing that total by the sample mass in grams (m) multiplied by 1 x 10^9. The balance calibration constant is calculated from the instrument by running an experiment with a standard with a known mass susceptibility. The standard used was mercury (II) tetrathiocyanatocobaltate (II) ($Hg[Co(SCN)_4]$), that has a known mass magnetic susceptibility of 1.644 x 10^{-5} erg·$G^{-2}cm^{-3}$. Once the mass magnetic susceptibility is found, the molar mass susceptibility (χ_M) can be calculated by multiplication of the mass magnetic susceptibility and the molecular weight of the sample (Equation 4).

$$\chi_M = M * \chi_g$$

Equation 4: Molar magnetic susceptibility.

At this time, the molar magnetic susceptibility includes contributions from both the paramagnetic (unpaired electrons) and diamagnetic (paired electrons) sources. Diamagnetic contributions are often found tabulated and can be summed and subtracted

from the molar magnetic susceptibility to provide only the paramagnetic component of the molar susceptibility. This is shown in Equation 5 and results in the term χ_A, which is called the corrected magnetic susceptibility.

$$\chi_A = \chi_M - \sum \chi_\alpha$$

Equation 5: Equation for the corrected magnetic susceptibility.

The corrected magnetic susceptibility can be used to solve for the effective magnetic moment (μ_{eff}) shown in Equation 6. The effective magnetic moment is a representation of how many unpaired electrons are present within the material. If the material is paramagnetic, meaning that there are unpaired electrons present, then their value for the μ_{eff} will be a positive value. In a diamagnetic material, where there are no unpaired electrons, the value for μ_{eff} will be negative value.

$$\mu_{eff} = 2.828\sqrt{\chi_A T}$$

Equation 6: Equation to determine the effective magnetic moment.

Analysis of the cobalt-doped zinc oxide samples is of interest to help determine the oxidation state of the cobalt present in the material. Cobalt will be paramagnetic, having unpaired d electrons, unlike zinc, which is diamagnetic and has no unpaired d electrons. Co^{2+} has 7 total d electrons that when in a high spin configuration have a total of 3 unpaired electrons or when it is in a low spin configuration have a total of 1 unpaired electron. Co^{3+}, on the other hand, will have four unpaired electrons in the high spin

orientation and be diamagnetic if it is low spin. These high spin and low spin states are affected by the field splitting caused by ligands attached to the metal as well as other factors such as geometry. In the case of the materials developed in these experiments, we expect Co^{2+} to be present in high spin orientation due to the low position of oxide in the spectrochemical series and the tetrahedral geometry. The spin-only magnetic moment is equal to $\sqrt{(n)(n+2)}$. Thus for Co^{2+}, the magnetic moment would be 3.87 (n = 3) while for Co^{3+} it would be 2.82 (n = 2). Thus it may be concluded that the cobalt is present as Co^{2+} and the cobalt ions are not predominantly adjacent to each other. If the latter were the case, antiferromagnetic ordering would lower the magnet moment. Notably, the effective magnetic moments that were found experimentally (Table 4) also correspond to that published for other high spin Co^{2+} complexes.[21]

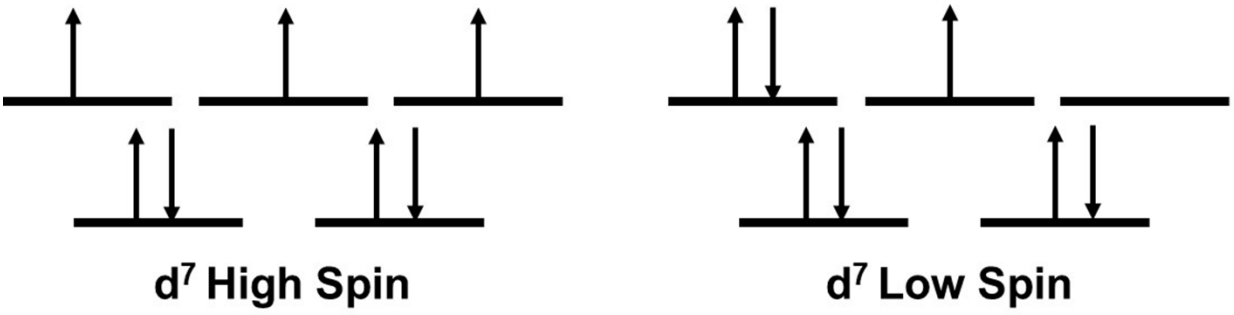

Figure 15: Orbital occupancy for d electrons in a d^7 tetrahedral complex.

Table 4: Effective magnetic moments.

Material	μ_{eff}
5% Co ZnO	3.95
10% Co ZnO	3.85

The elemental composition of the cobalt-doped zinc oxide was determined by microwave plasma atomic emission spectroscopy. Acid digestion was carried out on the oxide powder to solubilize the sample. This method involves dissolving 50 mg of the cobalt-doped zinc oxide in 30 mL of 5 M HCl. This solution was then heated at 80 °C until the solution reaches almost complete dryness (total sample weight > 0.5 g). When this final weight is achieved, the solution was initially diluted with deionized H_2O to a total volume of 5 mL and then can be further diluted with deionized H_2O to move the metal concentrations into the range of the machine calibration. The calibration range used in both the cobalt and zinc determinations was 1 to 20 ppm and standards were made using dilutions from 1,000 ppm stock solutions purchased from Alfa Aesar. Analysis of the elements on the MP-AES was conducted at 340.51 nm for cobalt and 213.85 nm for zinc. The findings of the specific molar ratios of Co and Zn are given in Table 5. In both materials, the achieved dopant level was within a mole percent of the theoretical goal.

Table 5: Molar ratio of Co and Zn within the mixed metal oxides.

Material	Co Mole Percent
5% Co ZnO	6.2
10% Co ZnO	9.8

Development of a sputtering target was the original goal for these materials. The dimensions of these targets were 2.44” in diameter and .125” thick. This size was chosen to allow for further design and development of the target for photovoltaic applications. The targets were made using a pressing die that was manufactured on-site at Oklahoma State University (Figure 16). 10 g of each material was used for the fabrication of the

targets. The targets were formed under 2 tons of pressure that was achieved by use of a hydraulic press. Images of the final targets are shown in Figure 17. Sputtering of a copper backing was required to allow these targets to be further developed for the photovoltaic device. Unfortunately, the sputtering process resulted in severe cracking that destroyed the targets. Since these targets were material intensive, the shift of research emphasis to developing cobalt doped ZnO films on glass slides was determined to be a better use of materials.

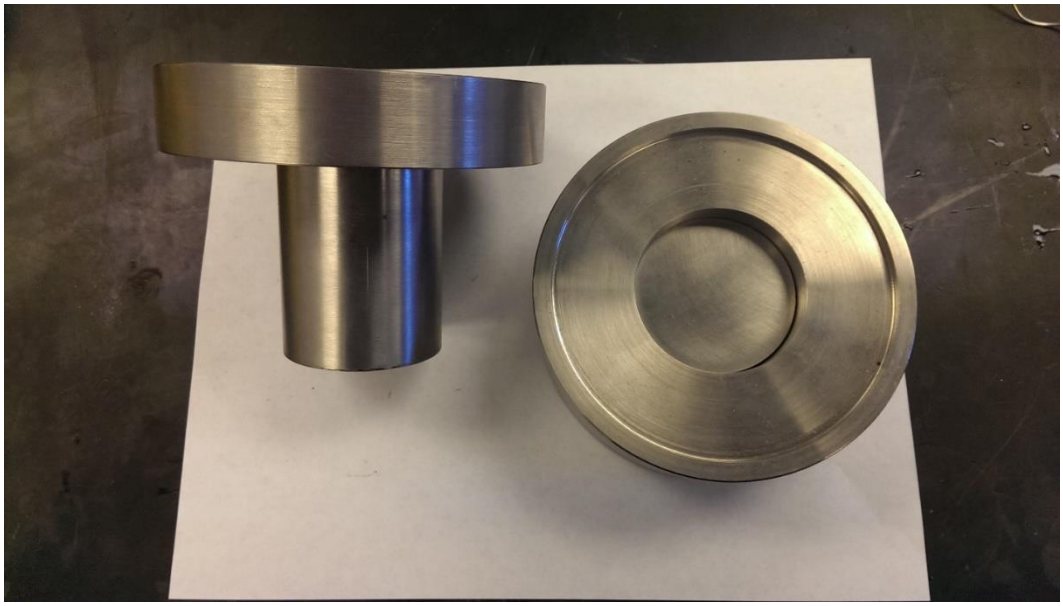

Figure 16: Dry press die for fabrication of the Co doped ZnO targets.

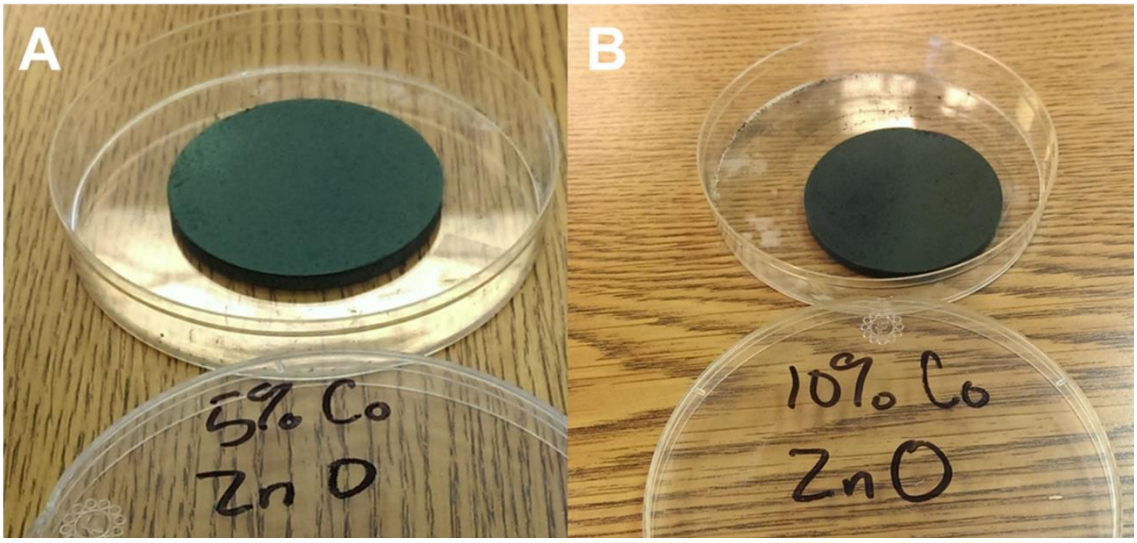

Figure 17: Fabricated Co doped ZnO targets: (A) 5% cobalt, (B) 10% cobalt.

Characterization of Products from the Chemical Bath Method

X-ray fluorescence spectroscopy was used initially to check for the presence of cobalt within the films on the glass slides. The cobalt containing slides, in fact, show the presence of a cobalt peak in the expected range of 6.93 keV (Figure 20) when compared to a pure ZnO film (Figure 21). The presence of cobalt can also be seen visually by the changes of the overall color of the films. When using the chloride salts, the final film is a green hue (Figure 18) while the film from the nitrate salts was pink in color (Figure 19).

Figure 18: 5% cobalt-doped Zn film grown using chloride salts on glass.

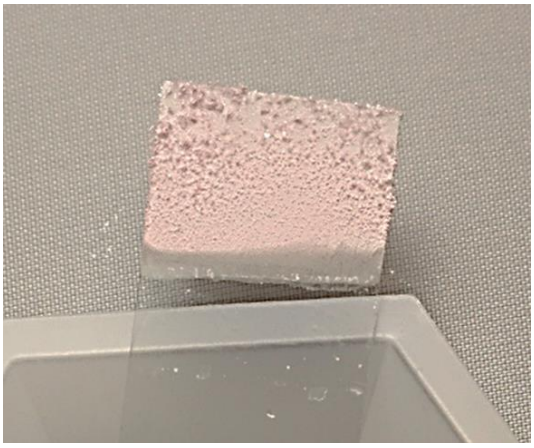

Figure 19: 10% cobalt-doped Zn film grown using nitrate salts on glass.

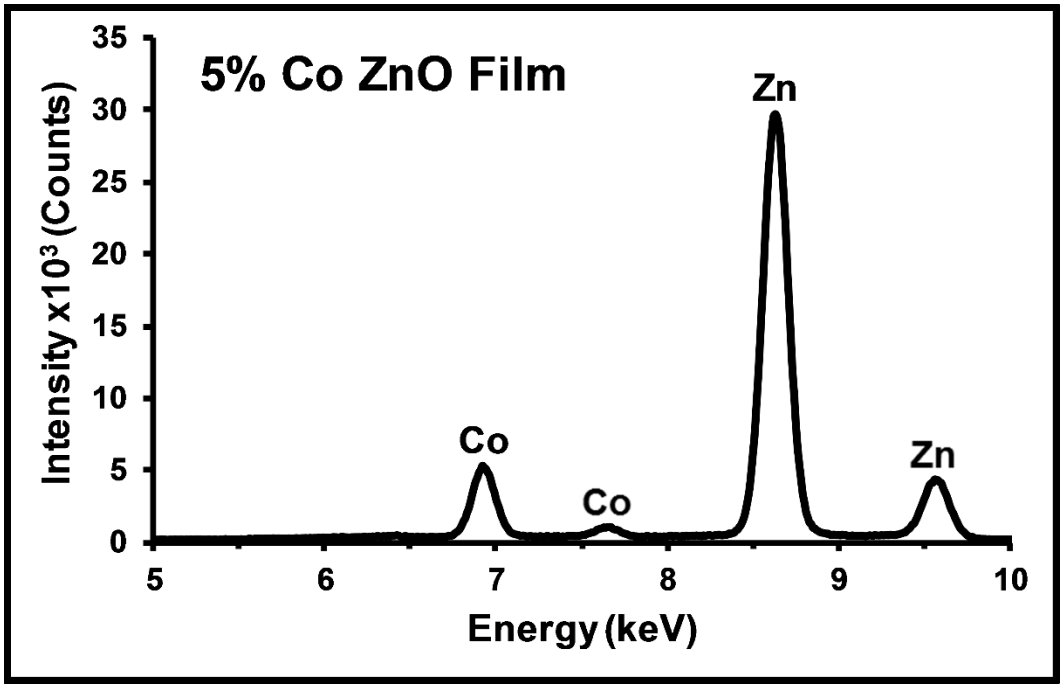

Figure 20: XRF spectrum of the 5% cobalt-doped ZnO film grown on glass.

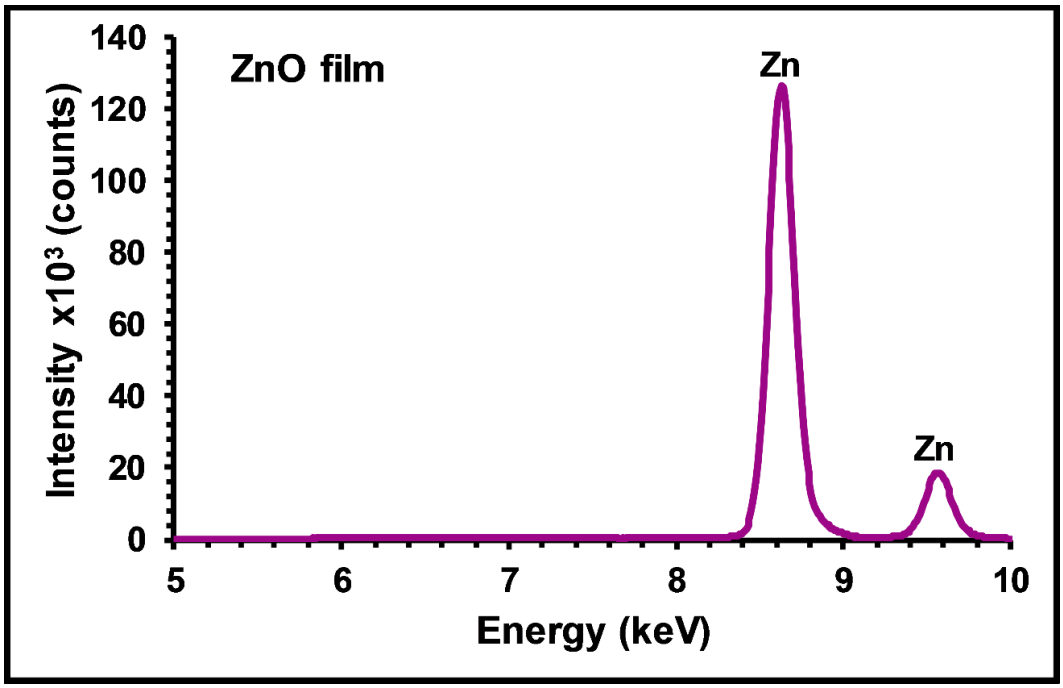

Figure 21: XRF spectrum of the pure ZnO film grown on glass.

X-ray powder diffraction was used to further investigate the crystallinity of the films. The first series of films investigated were those made by the use of zinc and cobalt nitrate salts. This pink film provided a crystalline diffraction pattern and using the ICDD database it was found that this pattern corresponded to the diffraction pattern of zinc hydroxide nitrate ($Zn_5(OH)_8(NO_3)_2 \cdot 2H_2O$) (Figure 22).[22,23] This material has a layered structure where the double chains are built from edge-sharing octahedral $Zn(OH)(NO_3)(H_2O)$ units.[23,24] In this structure, the divalent metal occupies three of the four octahedral sites and the two tetrahedral sites (Figure 23).[25] The nitrates in the system are found between the layers and do not take part in any bonding or coordination with the other species present. Due to the proximity in size of the ionic radii of Zn^{2+} (0.74 Å) and high spin Co^{2+} (0.75 Å) the cobalt ions can replace the zinc ions within the crystal structure.[25]

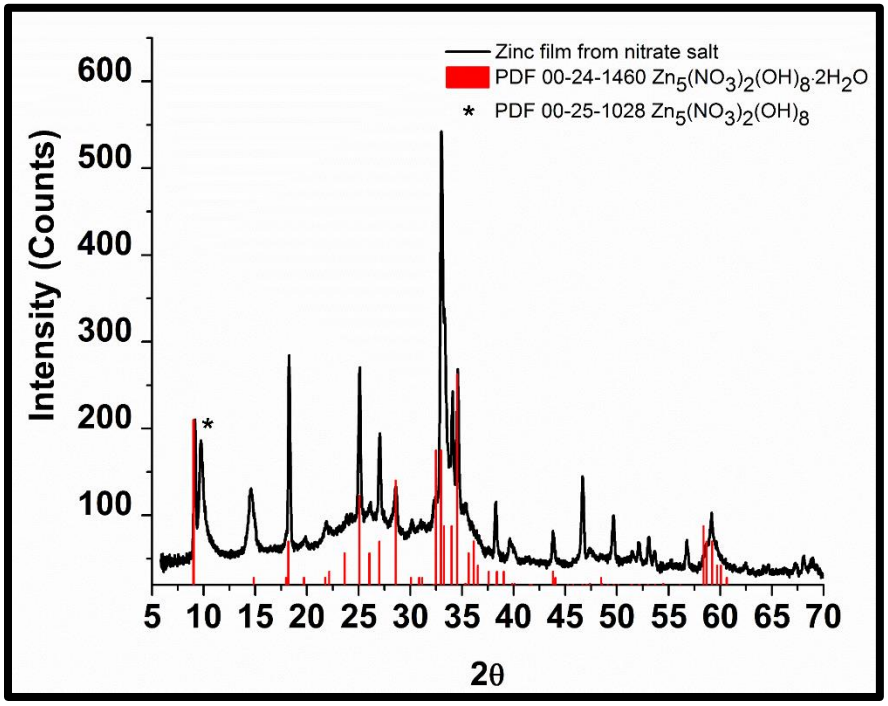

Figure 22: X-ray diffraction pattern of 10% cobalt-doped zinc film grown by nitrate metal salts with matching PDFs from the ICDD.

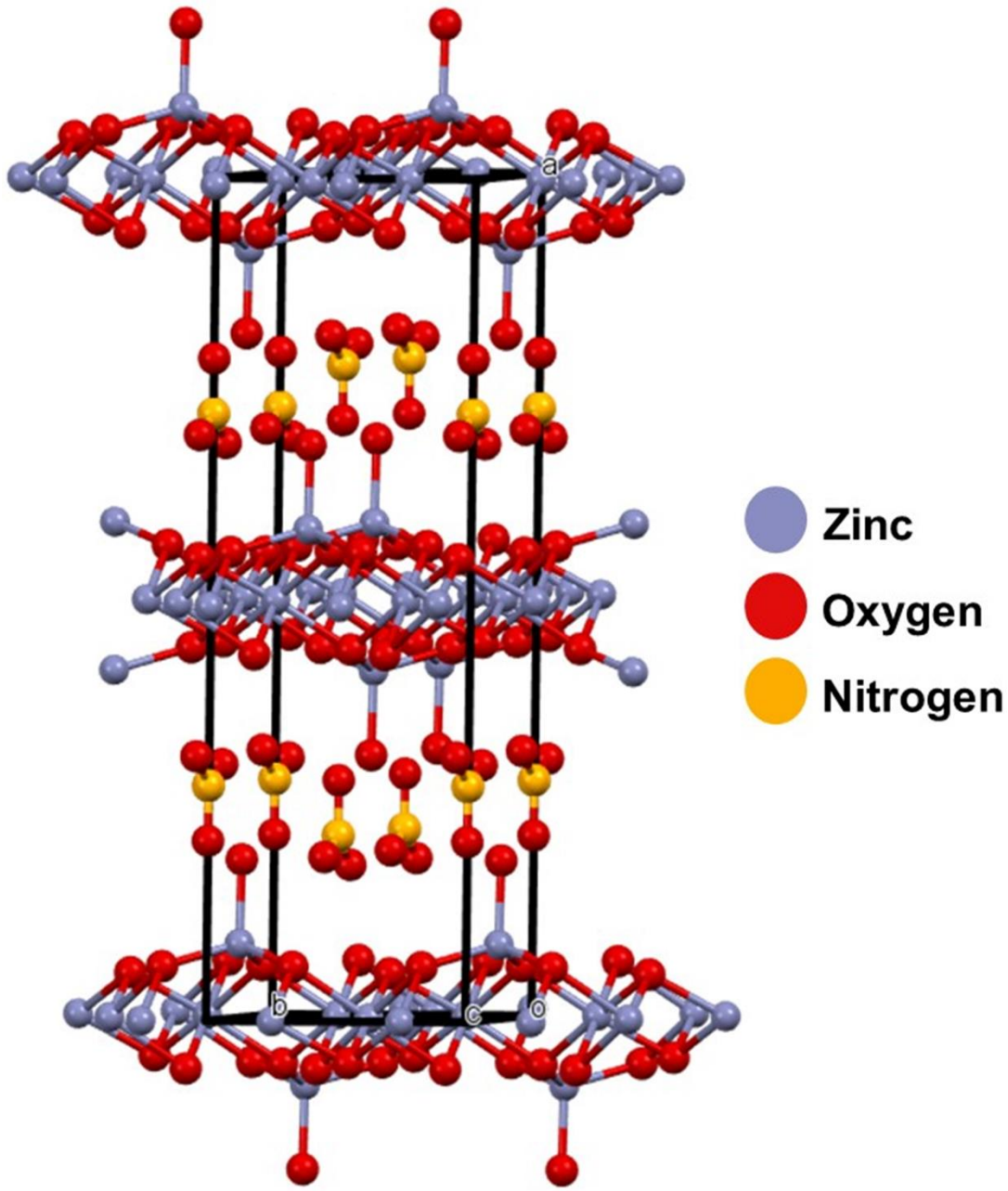

Figure 23: Crystal structure for $Zn_5(OH)_8(NO_3)_2$.[23]

The diffraction pattern for the green films that were produced using chloride salts (Figure 24) matched that of zinc hydroxide chloride monohydrate ($Zn_5(OH)_8(Cl)_2 \cdot H_2O$).

This compound can be found naturally as the mineral Simonkolleite. Its crystal structure is quite similar to that of the material produced by the use of the nitrate salts. It is a layered hydroxide structure with the Zn^{2+} being found in three of the four octahedral sites as well as the two tetrahedral sites (Figure 25). The major difference within this crystal structure is that unlike the NO_3^-, the Cl^- is within the layers where it is coordinated to the Zn^{2+} found in the tetrahedral sites.[26]

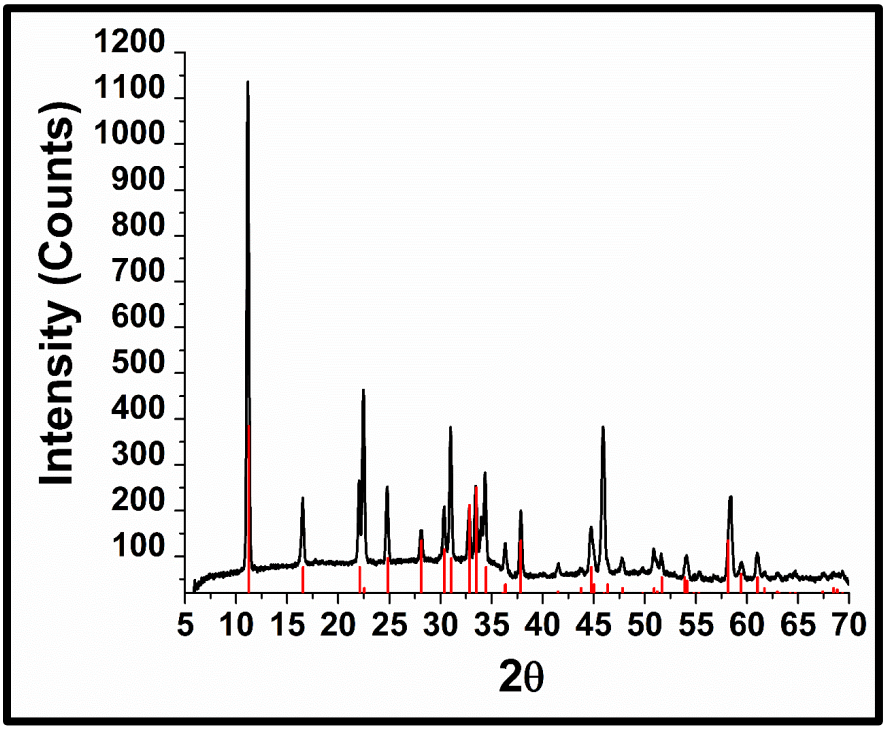

Figure 24: X-ray diffraction pattern of 10% cobalt-doped zinc film grown by chloride salts matched using ICDD for $Zn_5(OH)_8(Cl)_2 \cdot H_2O$ (PDF : 00-007-0155).

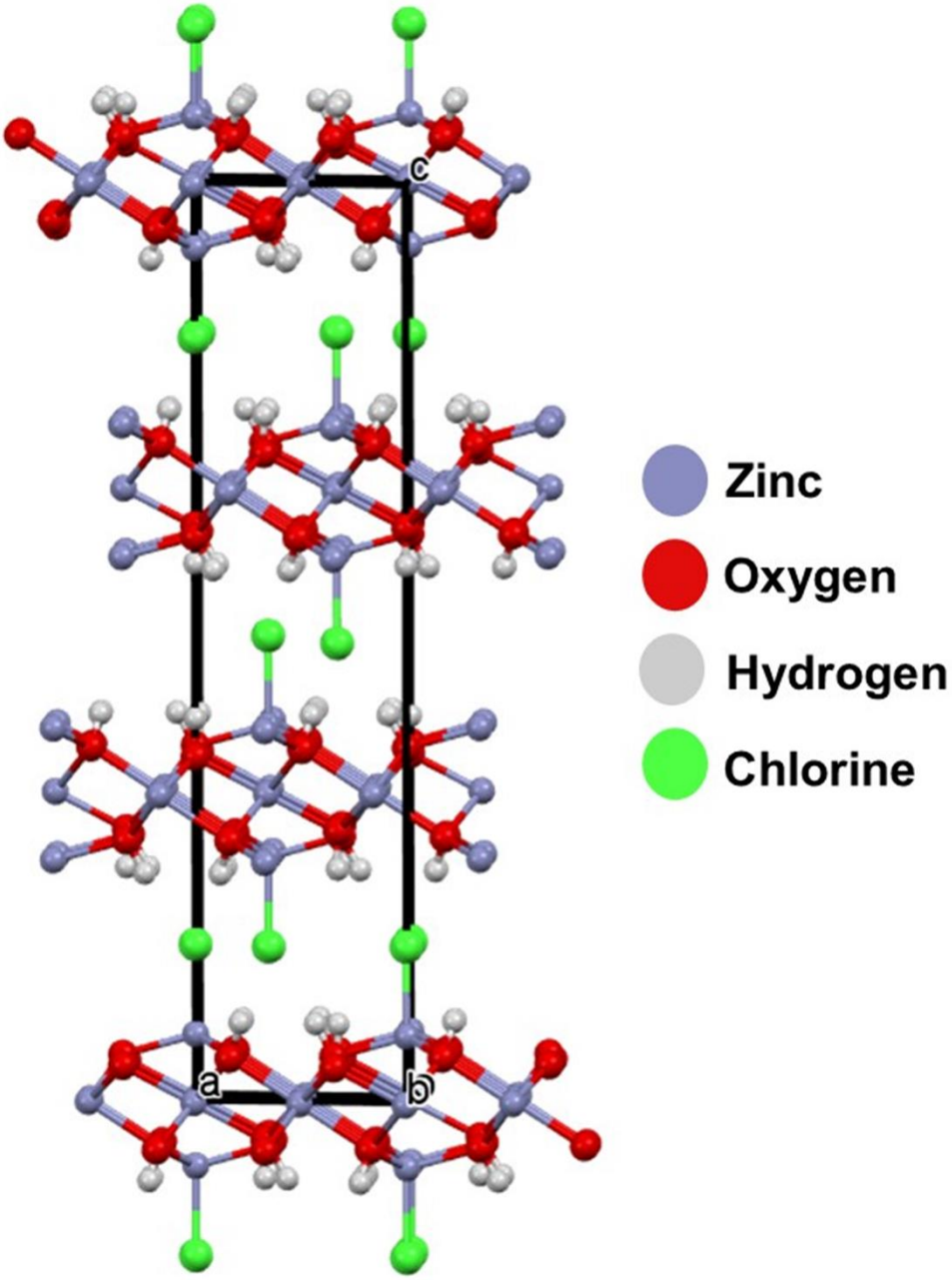

Figure 25: Crystal structure for $Zn_5(OH)_8(Cl)_2$.[27]

The differences in color between these two different films can be attributed to the position occupied by Co^{2+} in the structures. Neilson *et al.* has shown that the color of these layered hydroxide cobalt materials depends on what sites the cobalt occupies. Co^{2+}

found within the octahedral sites produces final materials that are pink in color and when the Co^{2+} ions are found within the tetrahedral sites the material is found to be a green-blue color.[28,29] This color change due to the spatial occupancy of the cobalt ions provides an explanation as to why there are differences in color between the final materials for both the chloride and the nitrate films. Notably, the cobalt-doped zinc oxide produced from the PAO complexes is also green and has Co^{2+} in tetrahedral sites.

The morphology of these films was probed using scanning electron microscopy. Due to these materials being semiconductors, carbon was sputtered onto the film to reduce the amount of charging in the electron beam. Looking at the films grown from chloride salts, micrographs of the pure Zn films grown showed unoriented hexagonal particles of various sizes (Figure 26). The introduction of cobalt into the system shows similar unoriented hexagonal particles, but it appears that the particles are uniform in size (Figure 27). When growing films using the nitrate salts, there is a shift in morphology from the hexagonal particles to fuzzy balls of what appears to be clusters of very fine plate-like particles. Both the pure ZnO film and the cobalt-doped zinc hydroxyl nitrate films have very similar particles present with no noticeable variation from the pure material to the doped (Figure 28 & 29).

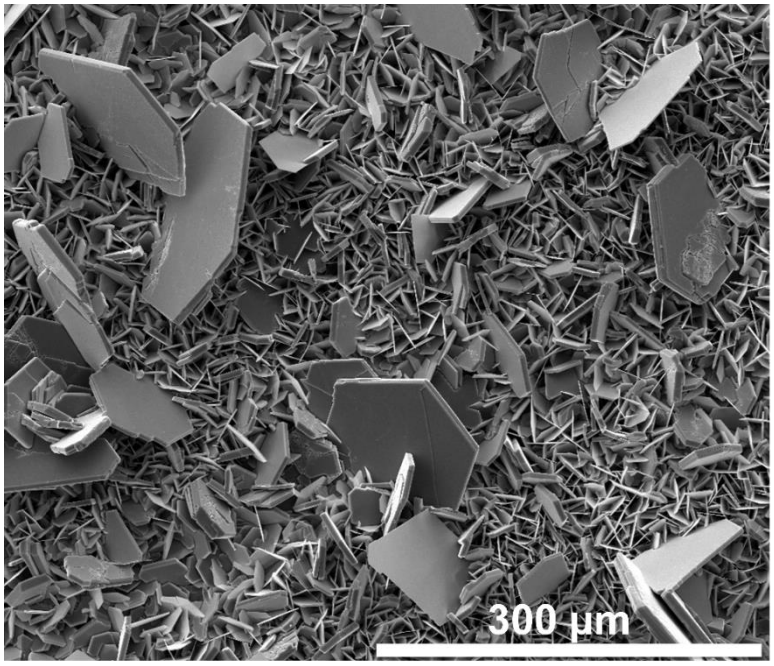

Figure 26: Scanning electron micrograph of a pure zinc film grown using chloride salts on a glass slide.

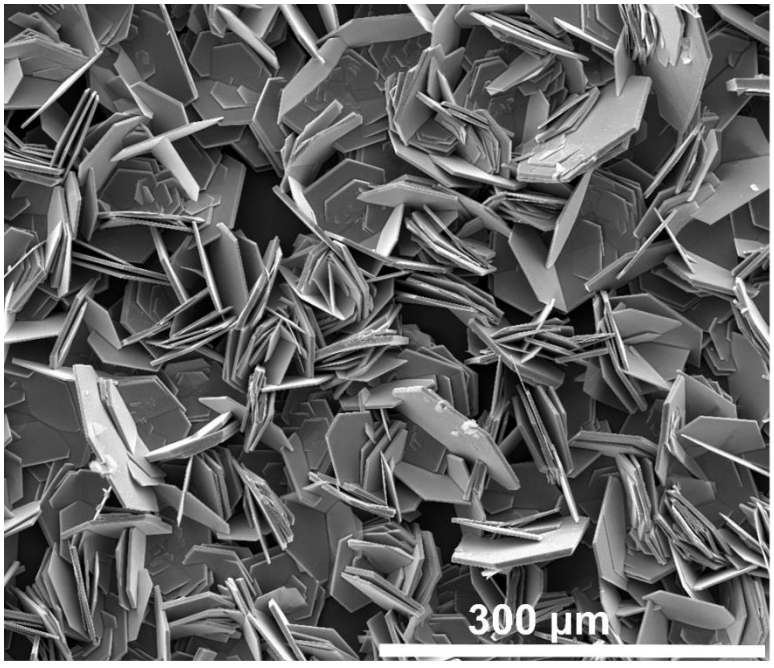

Figure 27: Scanning electron micrograph of a 5% Co doped zinc film grown using chloride salts on a glass slide.

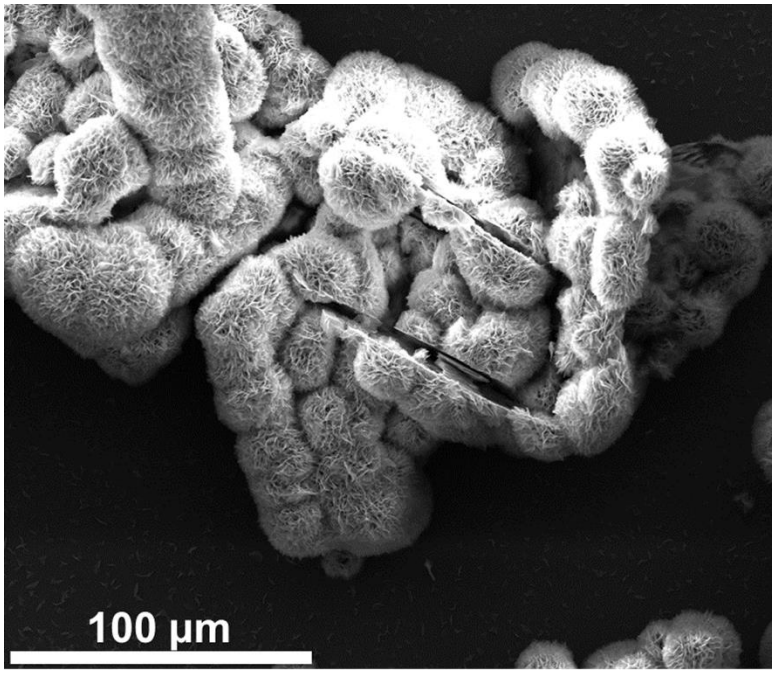

Figure 28: Scanning electron micrograph of a pure zinc film grown using nitrate salts on a glass slide.

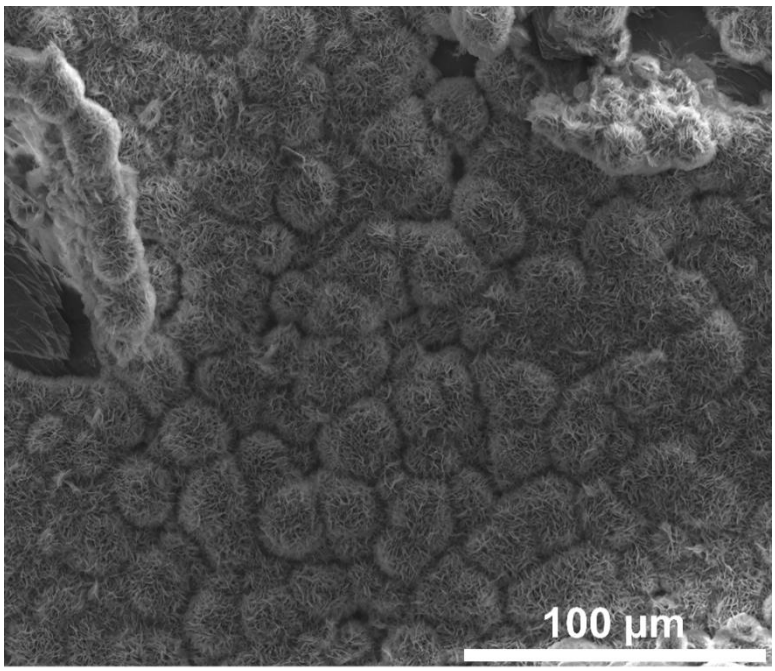

Figure 29: Scanning electron micrograph of a 5% Co doped zinc film grown using nitrate salts on a glass slide.

The elemental composition of the films was determined by microwave plasma atomic emission spectroscopy. These films were solubilized by digestion using 5M HCl at 80 °C. This digestion was followed by evaporation to almost complete dryness (> 0.5 g) and then the final volume was raised to 5 mL in total. The solubilized solutions were then diluted into the range of the standard calibration curve of cobalt and zinc. In both cases, the range of 1 to 20 ppm was used with standards made from 1,000 ppm standards purchased from Alfa Aesar. Table 6 & 7 summarizes the mole percent of cobalt found within the range of films investigated.

Table 6: Mole percent of cobalt within the films grown by chloride salts.

Target Material	Co Mole %
1.25% $CoZn_5(OH)_8(Cl)_2$	3.8 ± 0.7
2.50% $CoZn_5(OH)_8(Cl)_2$	6.0 ± 0.8
3.75% $CoZn_5(OH)_8(Cl)_2$	9.9 ± 0.7
8.00% $CoZn_5(OH)_8(Cl)_2$	17.4 ± 2.6

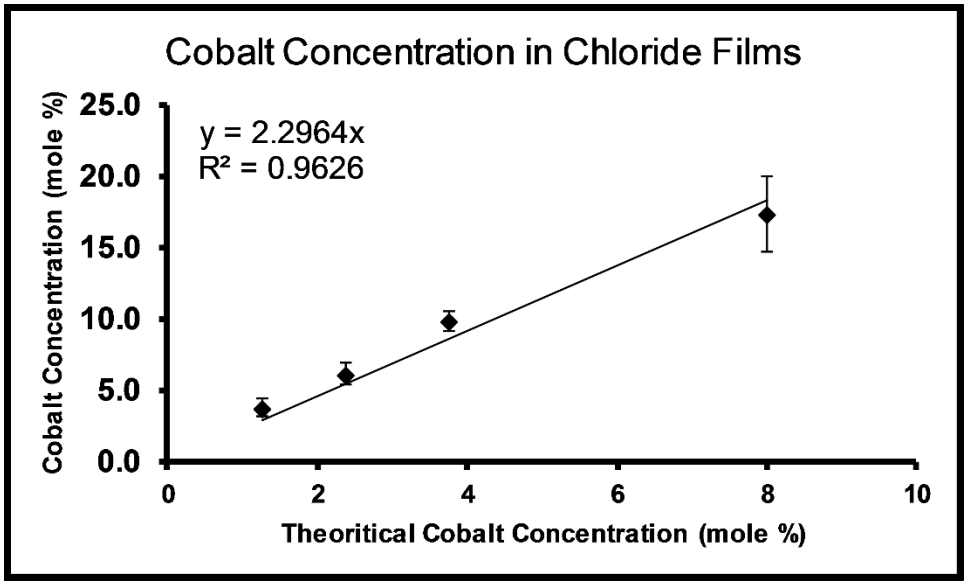

Figure 30: Cobalt mole percent trend within the chloride films.

Table 7: Mole percent of cobalt within the films grown by nitrate salts.

Target Material	Co Mole %
5% $CoZn_5(OH)_8(NO_3)_2$	2.7 ± 0.4
10% $CoZn_5(OH)_8(NO_3)_2$	6.4 ± 2.1
20% $CoZn_5(OH)_8(NO_3)_2$	11.4 ± 1.1

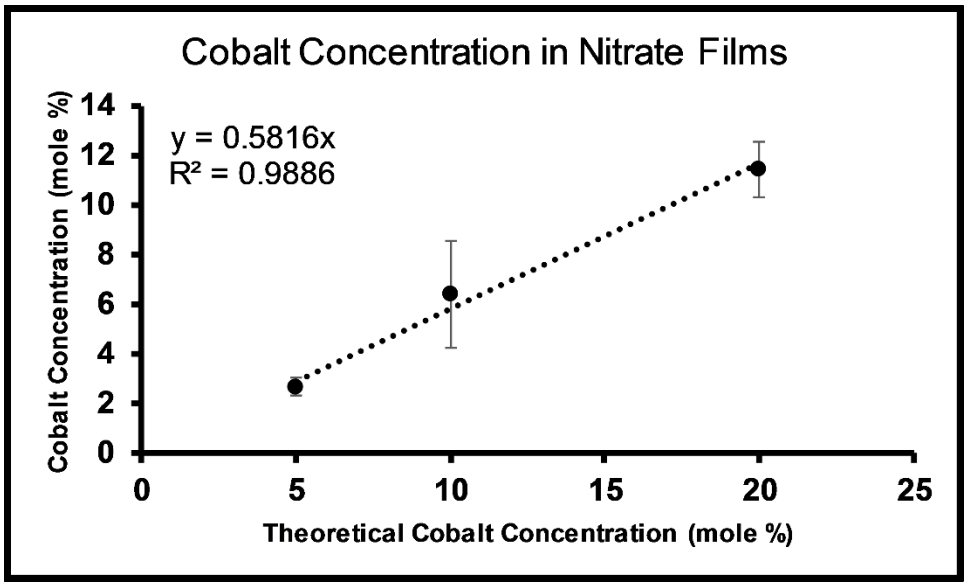

Figure 31: Cobalt mole percent trend within the nitrate films.

There is a linear dependence between the cobalt mole percent in the films and the amount used in the original bath. The doping concentrations for cobalt within the films that were made using the chloride salts were elevated from the initial metal ratio used (Table 6). The hydroxyl chloride film's slope is close to 2.3 meaning that the final χ_{Co} in the film is 2.3 times that of the original solution suggesting a bias in the system (Figure 30). On the other hand, the films derived from nitrate solutions are depleted in cobalt as

shown in Table 7 and Figure 31. The slope of the actual vs. theoretical cobalt concentration graph for the nitrate films is 0.58 and the intercept is zero. In this case, the solution after filtration is still enriched in cobalt (much less so than the chloride). However, the deposited film is much diminished in cobalt compared to the concentration in the deposition solution (Table 9). Considering that the opposite was true for the chloride salts, it must be concluded that the differences arise from the solubility of the cobalt in the zinc hydroxide host. As indicated by color, cobalt adopts the tetrahedral sites and these are $(OH)_4$ sites in the nitrate salts and $Cl(OH)_3$ in the chloride salt. Thus, the difference in cobalt incorporation likely arises from favored incorporation into tetrahedral $Cl(OH)_3$ sites. Presumably the fit in the tetrahedral $(OH)_4$ sites is poor for the Co^{2+} in comparison to the Zn^{2+} leading to the low incorporation of Co^{2+} in the hydroxy nitrate film.

The origin of the stark difference between the original solution and the final film was determined to be a difference in the solubility of the $MCl_2 \cdot HMTA$ complexes. The synthetic procedure uses excess reagents so that the chemical bath is saturated in the HMTA complexes. The excess complex is filtered off before the deposition step. Analysis of the starting solution and the filtered solution for the 5 mole percent cobalt deposition. After filtration, the solution was enriched in cobalt by a factor of 2.43, reflecting the lower solubility of the zinc HMTA complex versus the cobalt complex (Table 8). The deposition also produces films enriched slightly further with cobalt. This may be due to the higher solubility of cobalt hydroxide in an ammonia solution or a slight selectivity of the zinc hydroxide structure for cobalt over zinc.

Table 8: Following the reaction of 5% cobalt doping using the metal chlorides.

Compound	Mole % Starting Solution	Mole % Filtered Solution	Mole % Film
5% Cobalt	4.9	11.9	12.7

Table 9: Following the reaction of 5% cobalt doping using the metal nitrates.

Compound	Mole % Starting Solution	Mole % Filtered Solution	Mole % Film
5% Cobalt	4.9	6.0	2.4

The layered structure being synthesized by the chloride salts can be easily converted to ZnO by simple calcination at 200 °C for 2 hours (Figure 32). The film produced by the nitrate salts requires a calcination temperature of 250 °C for 2 hours to convert it to ZnO (Figure 34). In these decomposition pathways, there is loss of water and evolution of either HCl or NO_2 as the layered hydroxide convert to ZnO (Schemes 3 & 4).

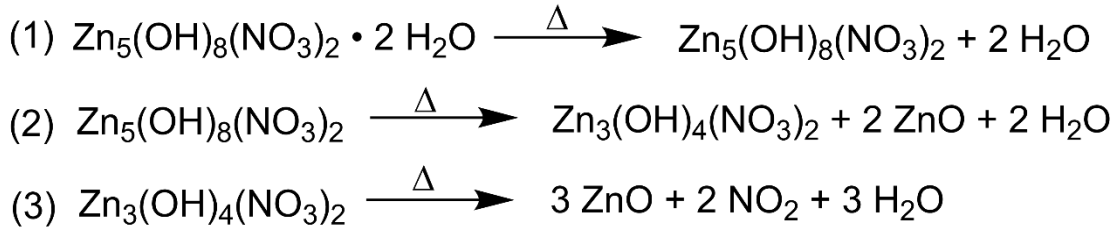

Scheme 3: Thermal decomposition of $Zn_5(OH)_8(NO_3)_2 \cdot 2H_2O$.[30,31]

(1) $Zn_5(OH)_8(Cl)_2 \cdot H_2O \xrightarrow{\Delta} Zn_5(OH)_8(Cl)_2 + H_2O$

(2) $Zn_5(OH)_8(Cl)_2 \xrightarrow{\Delta} 3\ Zn(OH)_2 + 2\ Zn(OH)Cl$

(3) $Zn(OH)_2 \xrightarrow{\Delta} ZnO + H_2O$

(4) $Zn(OH)Cl \xrightarrow{\Delta} ZnO + HCl$

Scheme 4: Thermal decomposition of $Zn_5(OH)_8(Cl)_2 \cdot H_2O$.[32]

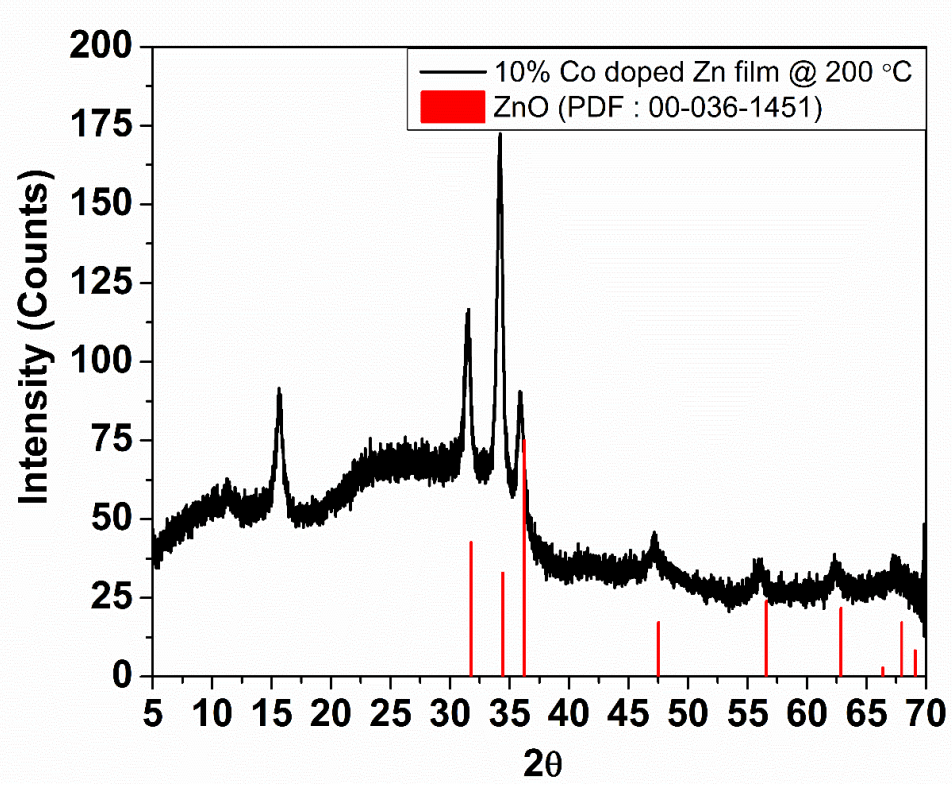

Figure 32: X-ray diffraction pattern for the 10% Co doped Zn film from chloride salts after calcination at 200 °C for 2 hours.

Figure 33: 10% Co doped Zn film from chloride salts after calcination at 200 °C.

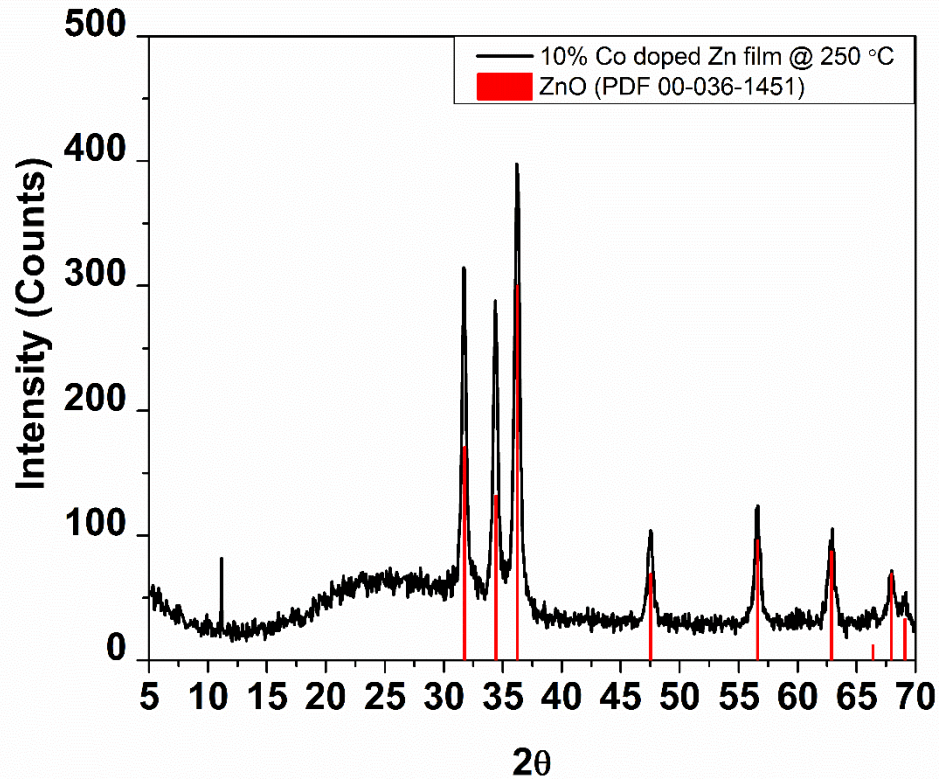

Figure 34: X-ray diffraction pattern for the 10% Co doped Zn film from nitrate salts after calcination at 250 °C for 2 hours.

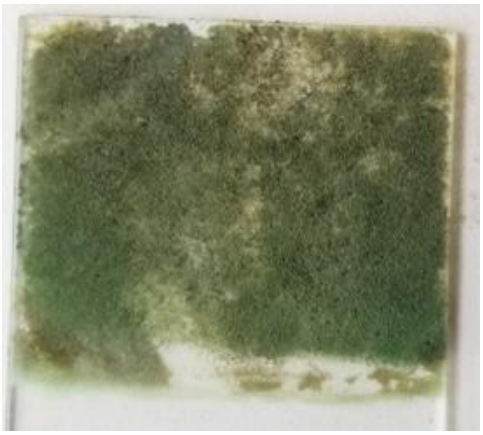

Figure 35: 10% Co doped Zn film from nitrate salts after calcination at 250 °C.

Analysis of films produced by collaborators at the University of Tulsa lead to an interesting observation of the film's composition. Instead of using a nylon, string to suspend the glass slides into the chemical bath, copper wire was used. Throughout the deposition process, copper was solubilizing and found to be incorporating copper ions into the zinc lattice. In researching the process of the copper being incorporated into the zinc oxide lattice, an ion exchange process was discovered whereby solid ZnO can be used for uptake of both copper and cobalt from aqueous solutions. Exploring this process, 200 mg samples of nanocrystalline ZnO, made through the decomposition of the pyruvic acid oxime precursors, was used to treat 20 mL solutions of 1,000 ppm copper and cobalt solutions. These samples were mixed for 24 hours and then were filtered using 0.45 μm nylon syringe filters. The treated solutions were then diluted into a standard calibration range for the microwave plasma atomic emission spectrometer. Standards for the calibration curves were made from 1,000 ppm standard solutions purchased from Alfa Aesar. The data from the microwave plasma shows a significant decrease in the cobalt and copper solutions along with a concomitant increase of zinc ions in the solutions

(Figures 34 & 35). In both cases, there is about a 1:1 molar exchange of cobalt or copper for zinc. ZnO blank samples were analyzed to determine Zn^{2+} concentration in just the presence of deionized water. It was determined that after the 24 hour period, the concentration of Zn^{2+} in solution was 103 ppm. There is also an obvious color change to both of these treated solids. ZnO starts as a white solid and after the reaction with copper the resulting powder is bright blue (Figure 36). A color change is also evident when reacting the ZnO with the cobalt solutions resulting in the formation of a pink solid (Figure 37). It may be concluded that nanocrystalline zinc oxide has the ability to undergo ion exchange with divalent metal ions. Notably, bulk zinc oxide does not show such reactivity as expected for a material without channels for ion exchange. Further investigation into this process is needed and may allow for post synthesis doping of ZnO powders and films by simple immersion into corresponding divalent metal solutions.

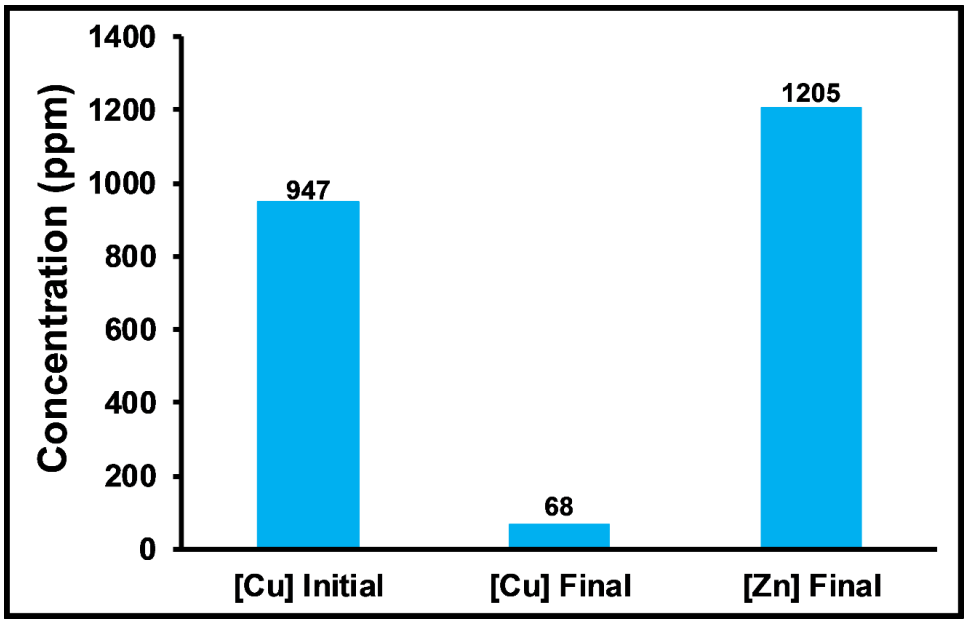

Figure 36: Concentration change for copper treated with ZnO powder.

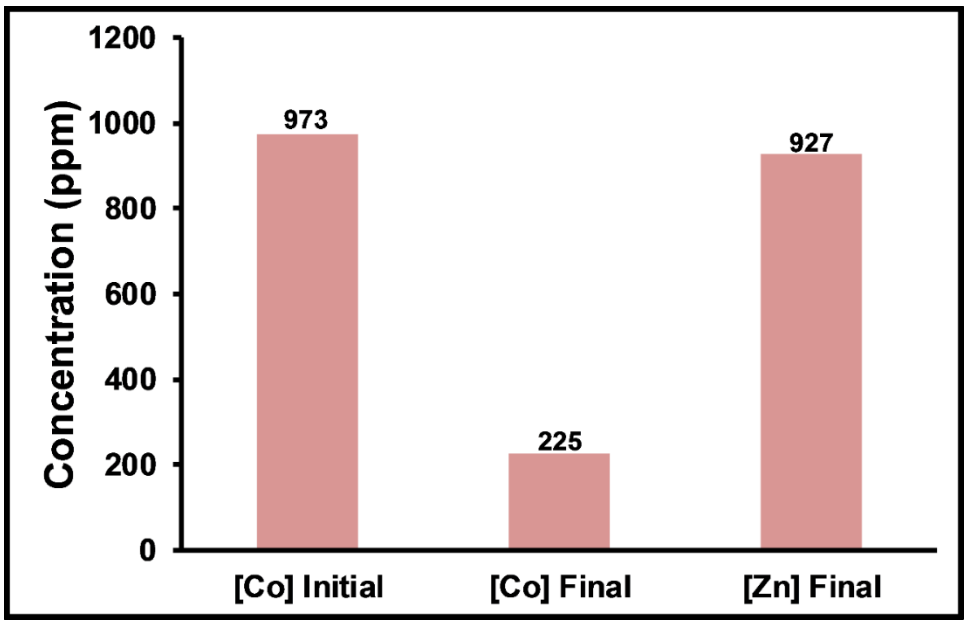

Figure 37: Concentration change for cobalt treated with ZnO powder.

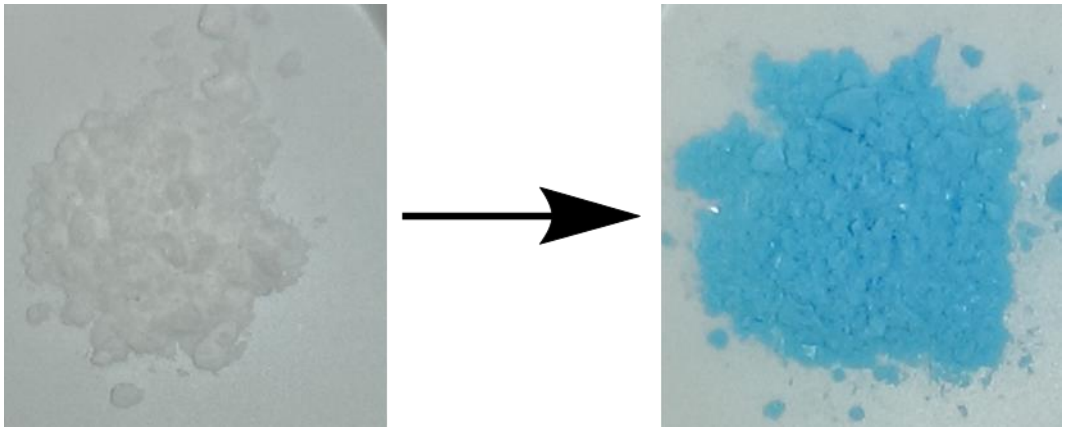

Figure 38: Visual change that occurs after treatment with 1,000 ppm Cu^{2+} solution.

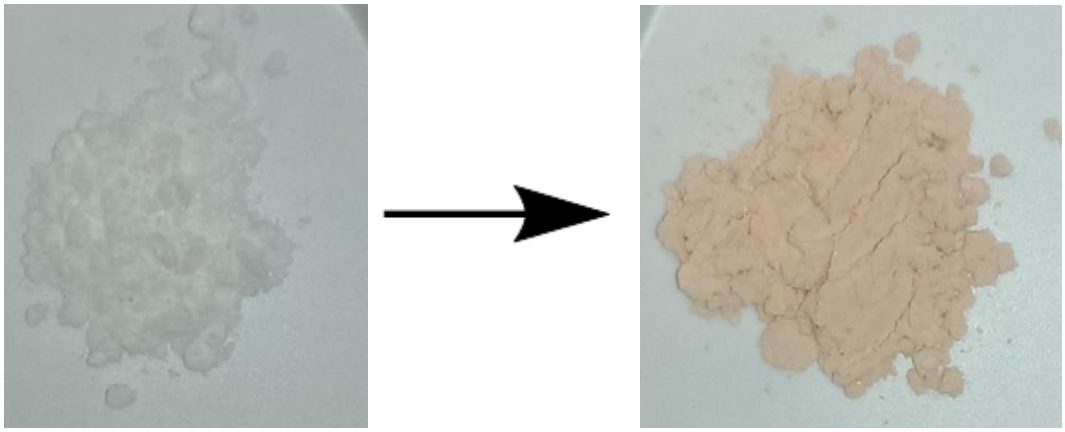

Figure 39: Visual change that occurs after treatment with 1,000 ppm Co^{2+} solution.

Conclusion

Two different synthetic routes were successfully used to synthesize cobalt-doped zinc oxide with a range of cobalt doping percentages. Using the single source precursor method, 5% and 10% cobalt doped ZnO was synthesized through decomposition of a pyruvic acid oxime precursor. This approach provided an easy synthetic method to produce precursors that decompose at low temperatures producing the doped metal oxide, H_2O, CO_2, and CH_3CN. The stoichiometry of the material was retained from the starting solutions through the final material allowing for easy tailoring of the concentration of cobalt doped into the ZnO crystal structure. The produced powder was pressed into sputtering targets for possible use for preparation of photovoltaic devices. The difficulty in the application of a copper backing onto the targets led to the desire to investigate a chemical bath deposition method. In this method, hexamethylenetetramine and either metal chlorides or metal nitrates were mixed and then filtered. This filtrate was then used to make a chemical bath that was used to grow films on suspended glass slides. In the chloride chemical baths, the cobalt concentration had an increased final concentration of

roughly 2.3x the expected theoretical concentration. The films made using the metal nitrate salts had a decreased level of cobalt doping. These final concentrations were about half the expected cobalt mole percent. Deposition of these films onto glass slides will allow for easy future device development for photovoltaics. An interesting discovery made during the development of these films was ZnO ability to undergo ion exchange with Co^{2+} or Cu^{2+} solutions. This could lead to a fast and simple method to introduce dopants into ZnO films.

References

1. Hoffmann, R., How chemistry and physics meet in the solid state. *Angewandte Chemie International Edition* 1987, *26* (9), 846-878.

2. Miessler, G. L.; Tarr, D. A., *Inorganic Chemistry*. Pearson Education: 2004.

3. Anderson, J.; Chris, G. V. d. W., Fundamentals of zinc oxide as a semiconductor. *Reports on Progress in Physics* 2009, *72* (12), 126501.

4. Green, M. A., Recent developments in photovoltaics. *Solar Energy* 2004, *76* (1), 3-8.

5. Matt Boreland., D. B. *Current and Future Photovoltaics*; Office of Science and Innovation: United Kingdom, 2006.

6. Bush, K. A.; Palmstrom, A. F.; Yu, Z. J.; Boccard, M.; Cheacharoen, R.; Mailoa, J. P.; McMeekin, D. P.; Hoye, R. L. Z.; Bailie, C. D.; Leijtens, T.; Peters, I. M.; Minichetti, M. C.; Rolston, N.; Prasanna, R.; Sofia, S.; Harwood, D.; Ma, W.; Moghadam, F.; Snaith, H. J.; Buonassisi, T.; Holman, Z. C.; Bent, S. F.; McGehee, M. D., 23.6%-efficient monolithic perovskite/silicon tandem solar cells with improved stability. 2017, *2*, 17009.

7. Yoder, M. N., Wide bandgap semiconductor materials and devices. *IEEE Transactions on Electron Devices* 1996, *43* (10), 1633-1636.

8. Özgür, Ü.; Alivov, Y. I.; Liu, C.; Teke, A.; Reshchikov, M. A.; Doğan, S.; Avrutin, V.; Cho, S.-J.; Morkoç, H., A comprehensive review of ZnO materials and devices. *Journal of Applied Physics* 2005, *98* (4), 041301.

9. Harrison, S. E., Conductivity and Hall Effect of ZnO at Low Temperatures. *Physical Review* 1954, *93* (1), 52-62.

10. Van de Walle, C. G., Hydrogen as a Cause of Doping in Zinc Oxide. *Physical Review Letters* 2000, *85* (5), 1012-1015.

11. Chai, G.; Lupan, O.; Chow, L.; Heinrich, H., Crossed zinc oxide nanorods for ultraviolet radiation detection. *Sensors and Actuators A: Physical* 2009, *150* (2), 184-187.

12. Smith, A. M.; Nie, S., Semiconductor Nanocrystals: Structure, Properties, and Band Gap Engineering. *Accounts of Chemical Research* 2010, *43* (2), 190-200.

13. Hari, P.; Baumer, M.; Tennyson, W. D.; Bumm, L. A., ZnO nanorod growth by chemical bath method. *Journal of Non-Crystalline Solids* 2008, *354* (19), 2843-2848.

14. Baranov, A. N.; Chang, C. H.; Shlyakhtin, O. A.; Panin, G. N.; Kang, T. W.; Young-Jei, O., In situ study of the ZnO–NaCl system during the growth of ZnO nanorods. *Nanotechnology* 2004, *15* (11), 1613.

15. Allan, J. R.; Brown, D. H.; Lappin, M., Transition metal halide complexes of hexamethylenetetramine. *Journal of Inorganic and Nuclear Chemistry* 1970, *32* (7), 2287-2292.

16. Paboudam, A. G.; Mohamadou, A.; Agwara, M. O.; Conde, M. A.; Ndifon, P. T., Solution Studies on Co(II), Ni(II), Cu(II), and Zn(II) Complexes of Hexamethylenetetramine in Aqueous and Non-Aqueous Solvents. *International Journal of Inorganic Chemistry* 2014, *2014*, 9.

17. Gaudon, M.; Toulemonde, O.; Demourgues, A., Green Coloration of Co-Doped ZnO Explained from Structural Refinement and Bond Considerations. *Inorganic Chemistry* 2007, *46* (26), 10996-11002.

18. Ungár, T., Microstructural parameters from X-ray diffraction peak broadening. *Scripta Materialia* 2004, *51* (8), 777-781.

19. Liu, K. C., Heifen, Experiment verification for the dependence of the X-ray diffraction line profile with the absorption of sample. *Advances in X-ray Analysis* 2012, *55*, 182-185.

20. Evans, D. F., A new type of magnetic balance. *Journal of Physics E: Scientific Instruments* 1974, *7* (4), 247.

21. Barefield, E. K.; Busch, D. H.; Nelson, S. M., Iron, cobalt, and nickel complexes having anomalous magnetic moments. *Quarterly Reviews, Chemical Society* 1968, *22* (4), 457-498.

22. Li, P.; Ping Xu, Z.; Hampton, M.; T Vu, D.; Huang, L.; Rudolph, V.; Nguyen, A., *Control Preparation of Zinc Hydroxide Nitrate Nanocrystals and Examination of the Chemical and Structural Stability*. 2012; Vol. 116, p 10325-10332.

23. Stahlin, W.; Oswald, H. R., The crystal structure of zinc hydroxide nitrate, $Zn_5(OH)_8(NO_3)_2.2H_2O$. *Acta Crystallographica Section B* 1970, *26* (6), 860-863.

24. Eriksson, L.; Louër, D.; Werner, P. E., Crystal structure determination and rietveld refinement of $Zn(OH)(NO_3) \cdot H_2O$. *Journal of Solid State Chemistry* 1989, *81* (1), 9-20.

25. Ramesh, T. N.; Madhu, T. L., Thermal Decomposition Studies of Layered Metal Hydroxynitrates (Metal: Cu, Zn, Cu/Co, and Zn/Co). *International Journal of Inorganic Chemistry* 2015, *2015*, 11.

26. Tavares, S. R.; Vaiss, V. S.; Wypych, F.; Leitão, A. A., Similarities between Zinc Hydroxide Chloride Monohydrate and Its Dehydrated Form: A Theoretical Study of Their Structures and Anionic Exchange Properties. *The Journal of Physical Chemistry C* 2014, *118* (33), 19106-19113.

27. Hawthorne, F. C.; Sokolova, E., SIMONKOLLEITE, $Zn_5(OH)_8 Cl_2 (H_2O)$, A DECORATED INTERRUPTED-SHEET STRUCTURE OF THE FORM $[M\varphi_2]_4$. *The Canadian Mineralogist* 2002, *40* (3), 939-946.

28. Neilson, J. R.; Schwenzer, B.; Seshadri, R.; Morse, D. E., Kinetic Control of Intralayer Cobalt Coordination in Layered Hydroxides: $Co1{-}0.5xoctCoxtet(OH)_2(Cl)_x(H2O)_n$. *Inorganic Chemistry* 2009, *48* (23), 11017-11023.

29. Neilson, J. R.; Kurzman, J. A.; Seshadri, R.; Morse, D. E., Cobalt Coordination and Clustering in α-$Co(OH)_2$ Revealed by Synchrotron X-ray Total Scattering. *Chemistry – A European Journal* 2010, *16* (33), 9998-10006.

30. Biswick, T.; Jones, W.; Pacuła, A.; Serwicka, E.; Podobinski, J., The role of anhydrous zinc nitrate in the thermal decomposition of the zinc hydroxy nitrates $Zn_5(OH)_8(NO_3)_2 \cdot 2H_2O$ and $ZnOHNO_3 \cdot H_2O$. *Journal of Solid State Chemistry* 2007, *180* (4), 1171-1179.

31. Auffredic, J.-P.; Louër, D., Etude thermodynamique de la décomposition thermique des hydroxynitrates de zinc. *Journal of Solid State Chemistry* 1983, *46* (2), 245-252.

32. Tanaka, H.; Fujioka, A., Influence of thermal treatment on the structure and adsorption properties of layered zinc hydroxychloride. *Materials Research Bulletin* 2010, *45* (1), 46-51.

CHAPTER V

Conclusion and Future Work

In the first chapter of this dissertation, neutralization of reactive aggregate for the use in cement was investigated to reduce or prevent the expansion caused by alkali-silica reaction. Neutralization was carried out by treatments of the aggregate with $Ca(OH)_2$ and LiOH solutions. $Ca(OH)_2$ treatments reduced the expansion of the ASR 14% over the initial 14 days, as well as, over the whole 80 day experiment. This treatment needed to be carried out multiple times due to the low solubility of $Ca(OH)_2$. Possible improvement of the reduction of expansion by this treatment could be increased through additional treatments of the aggregate. LiOH was used to treat the aggregate at room temperature and an elevated temperature. Single and double treatments of the aggregates were also done to try to reach complete neutralization. Overall, the double treatments outperformed their single treatment counterparts. Significant reduction of ASR is seen over the first 14 days with continuation of the significant reduction over the whole 80 day experiment. All the treatments, except for the room temperature single treatment, passed the ASTM C 1206 standardized test for ASR expansion over the first 14 days. Further studies should focus on improving the LiOH neutralization of the aggregate and then investigate mortar bar studies using the ASTM C 1293 test.

The ASTM C 1293 is a long-term mortar bar test that measures expansion over a year. This test would give better insight into how these treatments would work in real life applications.

The second chapter of this dissertation covered the synthetic approach to develop mixed metal oxides via the decomposition of the corresponding mixed metal pyruvic acid oxime precursors. This synthetic approach allows for good control of the molar ratios of the desired metals that allows for controlled stoichiometry in the final mixed metal oxide. Low decomposition temperatures and the nanocrystallinity of final products provide added incentive in the production of these mixed metal oxides. These mixed iron and zinc metal oxides were then used as sorbents for arsenic remediation from aqueous samples. Interest in mixed iron and zinc metal oxides were probed for the increased arsenic uptake capacity for the bimetallic oxides compared to that of iron oxide. These targeted samples included stock solutions, industrial wastewaters, naturally occurring well water, and commercially available apple juice. When comparing the bimetallic iron/zinc oxide's uptake capacity to that of the pure iron oxide produced the same way, significant increase is showed in arsenate uptake capacity in acidic environments for the bimetallic materials. Maximum uptake capacity is decreased when targeting the dibasic arsenate, which is found in basic solutions. These materials were also able to show good uptake capacity for the neutral arsenite species. Using these materials to then treat industrial and naturally occurring samples showed excellent arsenic removal ability in the presence of competing ions in a range of pHs. Finally, commercial apple juice found with an elevated arsenic concentration (9 ppb) was treated and in 1 d treatments, the arsenic concentration was below detection limits of the instrumentation. Future studies should focus on identifying

an ideal pH range for maximum uptake capacity. In addition, uptake kinetics and competing ion studies should be completed to further compare these materials to commercially available products.

Finally, it was shown that cobalt doped zinc oxide was synthesized through two separate routes leading to a fine powders or films grown on glass substrates. Synthesis of the cobalt-zinc pyruvic acid oxime precursor complex was achieved through a simple precipitation reaction. These precursors can be decomposed at low temperature resulting in the corresponding doped zinc oxide. The second approach used the chemical bath deposition technique to produce films of cobalt doped zinc oxide at various cobalt percentages onto glass slides. This approach was used to address the difficulty seen in transitioning the previously synthesized powder material to a photovoltaic device. The film would lead to an easier transition to the final device construction. Materials made by both approaches produced colored solids, which is expected as the bandgap of zinc oxide is shifted into the visible spectrum. Doping of cobalt was successfully controlled in target ranges of 2.5% to 20%. Future research should be done investigating the electrical properties of the films and development of the final photovoltaic device.

VITA

Travis Reed

Candidate for the Degree of

Doctor of Philosophy

Thesis: NOVEL MATERIALS CHEMISTRY FOR STRUCTURAL, PHOTOVOLTAIC, AND ENVIRONMENTAL APPLICATIONS

Major Field: Chemistry

Biographical:

Education:

Completed the requirements for the Doctor of Philosophy in Chemistry at Oklahoma State University, Stillwater, Oklahoma in May, 2018.

Completed the requirements for the Bachelor of Science in Chemistry at Wayne State College, Wayne, Nebraska in 2010.

Experience:

Teaching Assistant – January 2011 to May 2013 – Oklahoma State University
Research Assistant – June 2013 to May 2018 – Oklahoma State University

Publications:

Perkins, C. K.; Reed, T. M.; Apblett, A. W., Sorption of lead from aqueous solutions by a commercially available tungsten trioxide nanopowder. *RSC Advances* 2015, *5* (84), 68991-68997.

Perkins, C. K.; Reed, T. M.; Brown, Z. A.; Apblett, A. W., Exceptional sorption behaviour of porous tungsten oxide for aqueous lead. Environmental Science: Water Research & Technology 2017, 3 (3), 429-432.

Professional Memberships:

American Chemical Society